

HYBRID PMN-PT / TERFENOL-D BROADBAND
TRANSDUCERS IN MECHANICAL SERIES
CONFIGURATION

A Thesis

Presented in Partial Fulfillment of the Requirements for
the Degree Master of Science in the
Graduate School of The Ohio State University

By

Patrick R. Downey, B.E.

* * * * *

The Ohio State University

2003

Master's Examination Committee:

Dr. Marcelo J. Dapino, Adviser

Dr. Gregory N. Washington

Approved by

Adviser

Department of Mechanical
Engineering

ABSTRACT

This thesis presents recent advances in the design and characterization of hybrid transducers incorporating both piezoelectric and magnetostrictive elements. The complementary properties of the two smart materials can be actively employed in the transducer to exhibit unique attributes and advantages over conventional smart structures. In order to analyze and validate the properties inherent to these hybrid concepts, a transducer is designed and constructed through a mechanical series arrangement of a PMN-PT stack and a Terfenol-D rod. This configuration provides a double resonant frequency response that can be tuned for a variety of applications. Of particular interest in this study is the use of the device as a Tonpilz sonar transducer achieving maximum bandwidth on the 1-6 kHz range. The primary focus of this investigation is the development of linear and nonlinear system models that completely describe the electrical and mechanical regimes of the transducer as well as the interaction among regimes. The linear model accurately simulates the transducer output at low drive levels, while the nonlinear model is applicable for all operating regimes. In addition, by addressing the constitutive nonlinearities and hysteresis in the piezoelectric and magnetostrictive processes, the nonlinear model facilitates design optimization and model-based control with a degree of efficacy which the linear model does not. Experimental data is collected from the test transducer and used to validate and improve the overall system models at the material level.

HYBRID PMN-PT / TERFENOL-D BROADBAND TRANSDUCERS IN MECHANICAL SERIES CONFIGURATION

By

Patrick R. Downey, M.S.

The Ohio State University, 2003

Dr. Marcelo J. Dapino, Adviser

This thesis presents recent advances in the design and characterization of hybrid transducers incorporating both piezoelectric and magnetostrictive elements. The complementary properties of the two smart materials can be actively employed in the transducer to exhibit unique attributes and advantages over conventional smart structures. In order to analyze and validate the properties inherent to these hybrid concepts, a transducer is designed and constructed through a mechanical series arrangement of a PMN-PT stack and a Terfenol-D rod. This configuration provides a double resonant frequency response that can be tuned for a variety of applications. Of particular interest in this study is the use of the device as a Tonpilz sonar transducer achieving maximum bandwidth on the 1-6 kHz range. The primary focus of this investigation is the development of linear and nonlinear system models that completely describe the electrical and mechanical regimes of the transducer as well as

the interaction among regimes. The linear model accurately simulates the transducer output at low drive levels, while the nonlinear model is applicable for all operating regimes. In addition, by addressing the constitutive nonlinearities and hysteresis in the piezoelectric and magnetostrictive processes, the nonlinear model facilitates design optimization and model-based control with a degree of efficacy which the linear model does not. Experimental data is collected from the test transducer and used to validate and improve the overall system models at the material level.

HYBRID PMN-PT / TERFENOL-D BROADBAND TRANSDUCERS IN MECHANICAL SERIES CONFIGURATION

By

Patrick R. Downey, M.S.

The Ohio State University, 2003

Dr. Marcelo J. Dapino, Adviser

This thesis presents recent advances in the design and characterization of hybrid transducers incorporating both piezoelectric and magnetostrictive elements. The complementary properties of the two smart materials can be actively employed in the transducer to exhibit unique attributes and advantages over conventional smart structures. In order to analyze and validate the properties inherent to these hybrid concepts, a transducer is designed and constructed through a mechanical series arrangement of a PMN-PT stack and a Terfenol-D rod. This configuration provides a double resonant frequency response that can be tuned for a variety of applications. Of particular interest in this study is the use of the device as a Tonpilz sonar transducer achieving maximum bandwidth on the 1-6 kHz range. The primary focus of this investigation is the development of linear and nonlinear system models that completely describe the electrical and mechanical regimes of the transducer as well as

the interaction among regimes. The linear model accurately simulates the transducer output at low drive levels, while the nonlinear model is applicable for all operating regimes. In addition, by addressing the constitutive nonlinearities and hysteresis in the piezoelectric and magnetostrictive processes, the nonlinear model facilitates design optimization and model-based control with a degree of efficacy which the linear model does not. Experimental data is collected from the test transducer and used to validate and improve the overall system models at the material level.

To my late grandmother, Julia Liederman

ACKNOWLEDGMENTS

I wish to thank my advisor, Dr. Marcelo J. Dapino, for his guidance, support, and understanding during the time of this research. Without his encouragement, advice, and patient editing this thesis would not have been possible. Under his study I have learned more than I had ever hoped. I also would like to thank Dr. Greg Washington for his position on my Master's Examination Committee. Dr. Ralph C. Smith of North Carolina State University provided assistance on the development of the hysteresis model.

I would like to acknowledge the various people in the Mechanical Engineering Department who helped make this work possible. The Ohio State University startup funds provided financial support for this research. Keith Rogers was a great help in the machine shop, Jerry Kingzett and Joe West provided various equipment, and Prem Rose Kumar and Mary Richards were very helpful as academic advisors.

This investigation was made possible by the donation of a Terfenol-D rod on an in-kind basis by Julie Slaughter of ETREMA Products, Inc., and by the helpful suggestions of Stephen Butler.

I am grateful to all of my friends and colleagues in the lab: Aayush Malla, LeAnn Faidley, David Moody, Brett Burton, John Herbert, and Juan Gamez. In particular, Aayush, LeAnn, Ian Package, and Brian Bray provided much needed intellectual

advice as well as extracurricular distractions. David Moody's creativity and assistance during the early stages of this project are much appreciated.

I am indebted to my friends and family back home for their continuous support. This thesis is the direct result of years of encouragement and patience from my brother, friends, aunts, and father, as well as the entire Downey and Skelly families. The determination, effort, and responsibility that were required for me to achieve this degree were instilled by my mother. I cannot fully express my appreciation and respect for all that she has done. Finally, I am grateful to Jen for shouldering all of our responsibilities during these past several weeks, and more importantly for her unwavering faith and dedication.

VITA

November 29, 1979 Born - Philadelphia, PA

2001 B.E. Mechanical Engineering,
University of Delaware

2001-present Graduate Research Assistant,
The Ohio State University.

PUBLICATIONS

Research Publications

P.R. Downey, M.J. Dapino, R.C. Smith “Analysis of Hybrid PMN/Terfenol Broad-band Transducers in Mechanical Series Configuration”. *Proceedings SPIE*, Paper 5049-24, 2003.

FIELDS OF STUDY

Major Field: Mechanical Engineering

Studies in Smart Materials and Structures: Dr. Marcelo J. Dapino

TABLE OF CONTENTS

	Page
Abstract	ii
Dedication	iii
Acknowledgments	iv
Vita	vi
List of Tables	x
List of Figures	xi
Chapters:	
1. Introduction	1
1.1 Motivation for Research	1
1.2 Smart Materials	3
1.3 Fundamental Concepts of Electricity and Magnetism	5
1.3.1 The Electric Charge and Field	6
1.3.2 Electric Flux and Gauss' Law	7
1.3.3 Polarization	9
1.3.4 The Magnetic Field	12
1.3.5 Magnetic Induction and Flux	15
1.3.6 Magnetization	17
1.3.7 Maxwell's Equations	18
1.4 Fundamental Concepts of Electric Circuits	20
1.4.1 Resistance, Capacitance, and Inductance	20
1.4.2 Impedance	22
1.5 Fundamental Concepts of Dynamic Systems	24

1.5.1	Mechanical Systems	24
1.5.2	Frequency Response	26
2.	Linear Transducer Model	31
2.1	Material Background and Constitutive Relations	31
2.1.1	Piezoelectric and Ferroelectric Materials	31
2.1.2	Linear Piezoelectric Modeling	35
2.1.3	PMN-PT Transducers	36
2.1.4	Magnetostrictive Materials	38
2.1.5	Magnetostrictive Process	39
2.1.6	Linear Magnetostrictive Modeling	42
2.1.7	Terfenol-D Transducers	45
2.2	Linear System Dynamics Model	48
2.2.1	Mechanical Model	50
2.2.2	Electroacoustics Model	55
2.2.3	Electrical Impedance Analysis	57
2.2.4	Electroacoustics Model for the Terfenol-D Section	62
2.2.5	Electroacoustics Model for the PMN-PT Section	65
2.2.6	Combined Linear Transducer Model	68
2.2.7	Determination of Model Parameters	68
2.2.8	Linear Model Simulations	70
3.	Nonlinear Transducer Model	75
3.1	Unified Hysteresis Model	76
3.1.1	Polarization	76
3.1.2	Magnetization	79
3.2	Active Strain Model	80
3.3	Structural Model	82
3.4	Implementation	86
4.	Transducer Design and Testing	93
4.1	Mechanical Design	93
4.2	Magnetic Circuit Design	98
4.3	Amplifier Configuration	100
4.4	Data Collection	102
4.5	Test Parameters	104

5.	Results and Analysis	106
5.1	Low Frequency Model and Test Results	106
5.2	Broadband Model and Test Results	111
5.2.1	Terfenol-D Section	111
5.2.2	PMN-PT Section	118
5.2.3	Complete Transducer	122
6.	Concluding Remarks	128
6.1	Conclusions	129
6.2	Future Work	130
Appendices:		
A.	Units in Electromagnetism	132
B.	Mechanical Part Drawings	133
C.	Amplifier Characterization	137
	Bibliography	143

LIST OF TABLES

Table	Page
A.1 Principal variables and units in electricity and magnetism.	132
C.1 Amplifier voltage gains at discrete frequencies for each electrical load.	141

LIST OF FIGURES

Figure	Page
1.1 Electric field lines for (a) two like charges and (b) two opposite charges.	7
1.2 Electric field for oppositely charged plates [13].	8
1.3 Electric field through a Gaussian surface [13].	8
1.4 Electric dipole moment [13].	10
1.5 Atomic electric dipole induced by applied field [13].	11
1.6 Polarization versus electric field for a typical piezoceramic.	11
1.7 Magnetic field lines from: (a) straight line current, (b) single wire loop, (c) solenoid, and (d) permanent bar magnet [8, 19].	13
1.8 Biot-Savart law applied to a single circular coil [8].	14
1.9 Magnetization versus magnetic field for a typical ferromagnetic material.	18
1.10 One degree of freedom mechanical system as (a) schematic and (b) free body diagram.	25
1.11 Frequency response of $G(j\omega)$ as (a) magnitude and (b) phase.	29
2.1 Ternary phase diagram of PZT and Relaxor-PT piezoceramics showing morphotropic phase boundaries [26].	34
2.2 Phase diagram showing the morphotropic phase boundary region for the (1-x)PMN-(x)PT solid solution system [30].	35

2.3	Crystallographic structure of Terfenol-D [8, 19].	41
2.4	Magnetostriction process arising from the application of field H [8, 19].	42
2.5	Simulation of initial (a) magnetization and (b) magnetostriction with applied field [8, 19].	43
2.6	Simulated strain versus magnetic field for Terfenol-D.	43
2.7	Magnetic field lines from a cylindrical permanent magnet like that encasing the Terfenol-D rod [23].	47
2.8	Overview of a typical Terfenol-D transducer [6].	47
2.9	Schematic of a Tonpilz broadband hybrid transducer.	48
2.10	Corresponding electrical circuit with the two active sections wired in parallel.	49
2.11	Transducer modeled as a 3 degree-of-freedom mechanical vibratory system.	50
2.12	Mechanical representation of the simplified (a) high frequency (PMN-PT) and (b) low frequency (Terfenol-D) vibration modes.	52
2.13	Head mass velocity response of the complete system and individual sections calculated from the ideal mode linear mechanical model (2.8)-(2.11).	54
2.14	General representation of an electromechanical transducer.	56
2.15	Experimental total and blocked electrical impedance magnitude of the PMN-PT section employed in this investigation.	58
2.16	Experimental impedance mobility loop associated with the data in Figure 2.15, showing resonance (f_r) and half power point (f_1, f_2) frequencies.	59
2.17	Experimental admittance mobility loop associated with the data in Figure 2.15, showing antiresonance (f_{ar}) and half power point (f_{a1}, f_{a2}) frequencies.	60

2.18	Simulated idealized and practical system responses with only Terfenol-D excitation as (a) total electrical impedance magnitudes and (b) head mass velocity responses.	72
2.19	Simulated idealized and practical system responses with only PMN-PT excitation as (a) total electrical impedance magnitudes and (b) head mass velocity responses.	73
2.20	Simulated idealized and practical system responses with excitation from both sections as (a) total electrical impedance magnitudes and (b) head mass velocity responses.	73
3.1	Helmholtz energy ψ and Gibbs energy G for increasing field E [32, 33].	77
3.2	Local polarization \bar{P} kernel from Equation (3.1) [33].	78
3.3	Sign convention for the prestress forces, inplane resultant, and rod deflection at boundary condition [10]. The variable \bar{u} represents the total deflection as opposed to the perturbation u employed in the modeling equations.	83
3.4	Structural model representation of the complete transducer.	86
3.5	Linear test functions $\phi_0(x)$, $\phi(x)$, and $\phi_N(x)$	89
4.1	Construction diagram of the total hybrid transducer.	95
4.2	Experimental force versus deflection curve for the Belleville washers used in the prestress mechanism.	97
4.3	Complete (a) PMN-PT / Terfenol-D transducer and (b) external housing structure.	98
4.4	Cross-section of the closed magnetic circuit components.	99
4.5	Finite element computation of the performance of the magnetic circuit.	101
4.6	Predicted variation of induction along the axis of the Terfenol-D rod calculated with FEMM v3.2.	101

5.1	Biased strain versus magnetic field data collected from the Terfenol-D section at 500 mHz. The minor loop depicts the drive range for subsequent broadband tests.	107
5.2	Magnetic induction versus magnetic field data collected from the Terfenol-D section at 500 mHz, showing biased major and minor loops.	108
5.3	Strain versus field data collected from the PMN-PT stack at 500 mHz.	108
5.4	Strain versus magnetic field for the Terfenol-D section simulated with the nonlinear model presented in Section 3.2.	110
5.5	Magnetization versus magnetic field for the Terfenol-D section simulated with the nonlinear model presented in Section 3.1.2.	110
5.6	Head mass velocity response with only Terfenol-D excitation.	112
5.7	Electrical impedance magnitude with only Terfenol-D excitation.	113
5.8	Impedance mobility loop with only Terfenol-D excitation.	113
5.9	Head mass velocity response with only Terfenol-D excitation with external load Z_L	114
5.10	Head mass velocity response with only Terfenol-D excitation with external load and increased damping in the modeled load impedance.	115
5.11	Head mass velocity response with only Terfenol-D excitation from all models.	116
5.12	Electrical impedance magnitude with only Terfenol-D excitation with external load.	117
5.13	Impedance mobility loop with only Terfenol-D excitation with external load.	117
5.14	Head mass velocity response with only PMN-PT excitation.	119
5.15	Electrical impedance magnitude with only PMN-PT excitation.	119
5.16	Impedance mobility loop with only PMN-PT excitation.	120

5.17	Head mass velocity response with only PMN-PT excitation from all models.	120
5.18	Electrical impedance magnitude with only PMN-PT excitation with external load.	121
5.19	Impedance mobility loop with only PMN-PT excitation with external load.	121
5.20	Head mass velocity response with both sections driven.	123
5.21	Head mass velocity response with both sections driven with external load.	123
5.22	Electrical impedance magnitude with both sections driven in parallel with external load.	125
5.23	Impedance mobility loop with both sections driven in parallel.	125
5.24	Electrical impedance magnitude with both sections driven with external load and added capacitor.	126
5.25	Impedance mobility loop with both sections driven and added capacitor.	126
5.26	Head mass velocity response with both sections driven with external load and added capacitor.	127
5.27	Head mass velocity response with both sections driven with external load.	127
B.1	Mechanical drawing of head mass.	133
B.2	Mechanical drawing of center mass.	134
B.3	Mechanical drawing of tail mass.	134
B.4	Mechanical drawing of a magnetic circuit steel piece.	135
B.5	Mechanical drawing of a magnetic circuit steel piece.	135

B.6	Mechanical drawing of a magnetic circuit steel piece.	136
C.1	Magnitude of amplifier frequency response with $R=10\Omega$ load.	138
C.2	Phase of amplifier frequency response with $R=10\Omega$ load.	138
C.3	Magnitude of amplifier frequency response with $L=225$ mH load. . . .	139
C.4	Phase of amplifier frequency response with $L=225$ mH load.	139
C.5	Magnitude of amplifier frequency response with $C=390$ nF load. . . .	140
C.6	Phase of amplifier frequency response with $C=390$ nF load.	140
C.7	Magnitude of amplifier frequency response to 5 kHz sine wave.	141
C.8	Magnitude of amplifier frequency response to all loads, showing agree- ment between random and sinusoidal inputs.	142
C.9	Phase of amplifier frequency response to all loads.	142

CHAPTER 1

INTRODUCTION

1.1 Motivation for Research

Conventional smart structures employ a single active material for actuation, sensing, or control. Recent advances have shown that hybrid systems containing multiple smart materials can exhibit unique attributes and advantages over those containing a single material. Each material element can have different electrical, mechanical, and thermal regimes, as well as unique coupling interactions among regimes. The complementary properties of certain classes of active materials can be employed effectively to design hybrid systems which augment the performance characteristics of or add functionality to any one individual material. Previous research on hybrid designs has targeted two specific metrics for improvement, energy efficiency [17] and frequency bandwidth [3]. Energy efficiency gains stem from the fact that more mechanical output can be achieved with less electrical input if a system's available energy is shared between different active elements with complementary electrical properties. In practice, these gains have not been fully realized in hybrid designs. The work on frequency bandwidth has led to novel designs for broadband transducers that can be tuned for a variety of applications.

One particular device that benefits greatly from enhancing the bandwidth is that of a Tonpilz sonar transducer such as those installed on naval ships. This transducer typically utilizes a single piezoelectric element, but recent U.S. Navy research has been aimed at enhancing the bandwidth of high power Tonpilz transducers through hybrid piezoelectric / magnetostrictive architectures [3]. It has been demonstrated that such architectures can produce increased velocity output in the low frequency range when compared with conventional devices. Because of the constitutive nonlinearities of the active materials and the coupling among the electric, magnetic, elastic, and thermal regimes, the efficient design and control of these hybrid transducers necessitates detailed material and system models.

The focus of this investigation is the development of linear and nonlinear models for broadband transducers employing the complementary electrical and mechanical properties of Terfenol-D ($\text{Tb}_{0.73} \text{ Dy}_{0.27} \text{ Fe}_{1.95}$) and lead magnesium niobate - lead titanate ($\text{PMN}_{0.65}\text{-PT}_{0.35}$). These models allow for the transducer bandwidth, and the variables that affect it, to be characterized to a further degree than previously attained by the Navy. The linear model is developed first to describe the transducer output at particular operating conditions. The nonlinear model is then needed for the more general case where all of the transducer properties are variable. By addressing hysteresis effects and the multi-regime coupling, these nonlinear models facilitate design optimization and model-based control with a degree of efficacy which linear models do not. In addition, such models could provide new design criteria for the implementation of the high energy efficiencies thought to be achievable with hybrid structures. In order to analyze and validate the properties of the model, a test

transducer is designed and constructed to provide the necessary data to optimize the overall system model at the material level.

1.2 Smart Materials

A smart material by definition is one that exhibits a characterizable change in some physical property under the influence of external stimuli. These variable material properties cover the microscopic as well as macroscopic mechanical, electrical, and thermal regimes. The different stimuli that can induce these changes include combinations of electric and magnetic field, stress, and heat. A wide range of smart materials are found in engineering practice today, and so a brief overview of the more common ones follows.

Piezoelectrics are ceramic or polymer materials that convert electrical to mechanical energy, and vice versa. These materials will strain under the application of an electric field (converse effect), and produce electric charge under the application of mechanical stress (direct effect) [4, 16, 20]. These two effects make piezoelectrics suitable as either actuators or sensors. For actuation, if the material is poled in a certain direction, applying field in this same direction will induce a quasi-linear length increase on the order of 0.1%. In general piezoceramics can operate over a large frequency range and are used in a wide variety of applications. Commonly these materials are produced as cylindrical stacks that extend axially for use in force or position applications. Thin sheets can be attached to or embedded in beams for bending actuation, vibration damping, and shape optimization. Piezoelectric materials have inherent hysteresis losses that typically must be accounted for through advanced modeling.

Electrostrictives are another class of electric materials that are similar in function to piezoelectrics but produce more strain and have a nonlinear strain to field dependence [4, 14, 27]. These materials also exhibit less hysteresis, implying a more efficient actuation. One concern with electrostrictives, however, is that their behavior is very dependent on operating temperature and applied stress. A popular electrostrictive, lead magnesium niobate (PMN), is often doped with a piezoceramic such as lead titanate (PT) to create a composite ceramic such as that used in this project. Under certain compositions and operating conditions this material can exhibit qualities of either class of smart material.

Magnetostrictives follow a similar behavior to electrostrictives but obviously respond to magnetic fields rather than electric. Both the converse and direct effects are present, i.e. the material will strain under a magnetic field and produce magnetic flux under stress [7, 18, 22]. The effect of the applied field on strain is highly nonlinear and hysteretic but they can generate more strain (0.2%) and force than piezoelectrics. Typically driven by a magnetic coil, these materials can exhibit a response over a large frequency range, but can have issues with heating in the drive coil. Terfenol-D is the most popular of this class of material, and as such is used in this research.

Electrorheological and magnetorheological fluids contain micro particles suspended in an inert carrier fluid that align with an applied electric or magnetic field, respectively. These particles join to form semi-rigid chains that can significantly alter the fluid properties like viscosity, yield stress, and plasticity. These effects are complex but reversible, making these materials useful in a range of devices such as clutches, dampers, valves, and suspensions.

Shape memory alloys are metals that can display large recovery strains (up to 10%) and forces through a martensitic-austenitic phase change. The transformation from one phase to the other is typically brought about via a combination of heat and stress, but some shape memory materials are activated magnetically. Shape memory materials suffer from large hysteresis effects and slow response times, but are quite popular because of the memory effect for which they are named. If an alloy is deformed at relatively low temperature while martensitic, the material can recover its original shape when raised above a certain transformation temperature. This process can be repeated through further temperature changes. This behavior is quite interesting and has led to numerous new technologies being developed.

All of these materials, and others not mentioned, show promise in future technological applications. Their high power capabilities, “clean” transduction, compact and efficient design, and ability to actuate and sense through a unified manner are heavily desired in all engineering systems. The fact that each smart material has an intrinsic multi-regime coupling creates possibilities for new designs to maximize the potential of these materials.

1.3 Fundamental Concepts of Electricity and Magnetism

In order to properly characterize smart materials, the underlying physics of the system must be understood. This section, borrowed heavily from Halliday [13], will review some general ideas from electromagnetism that are useful in modeling both Terfenol-D and PMN-PT.

1.3.1 The Electric Charge and Field

Electric charge is a fundamental property of all materials. Charge can be either positive or negative, with a balance or equality of the two being called electrically neutral. The atomic particles that are associated with charge are the positive proton and negative electron, which form orbital pairs. Protons are generally fixed but the electrons can often move, inducing a positive charge on the atom it left and a negative charge wherever it ends up. The general rule for electric charge is that alike charges repel each other while opposites attract. The strength of this force is quantified by Coulomb's Law

$$F = \frac{1}{4\pi\epsilon_0} \frac{|q_1||q_2|}{r^2}, \quad (1.1)$$

where ϵ_0 is the free space permittivity, q_1 and q_2 are charge magnitudes, and r is the distance between charges. The presence of this force is due to the existence of an electric field in the space surrounding each charge.

The electric field is a vector field quantity which exists around all electric charges consisting of both magnitude and direction at each point in space. When another charge is placed in this field, a force acts on it according to equation (1.1). It is often helpful to visualize electric field lines emanating from a charged particle (Figure 1.1). These lines extend away from positive charge and toward negative charge, and clearly show the repulsive and attractive nature of the like and opposite particles.

The concepts of charge and field are not constrained to particles but are applicable to any geometry. Of particular interest is a charged plate where field lines extend perpendicularly outward from the face. Near the boundaries of the plate the field will fringe, but for points near the surface and in the center the field appears uniform.

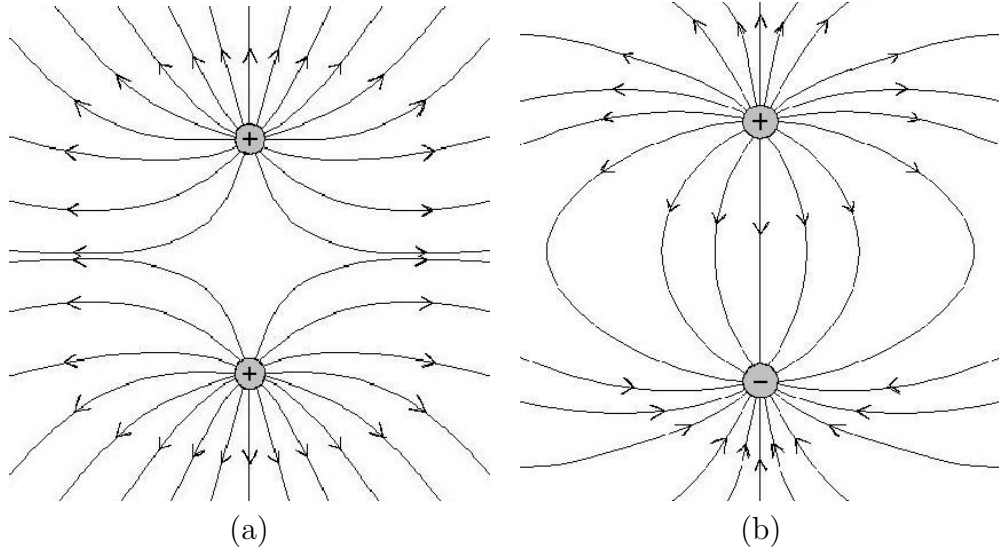


Figure 1.1: Electric field lines for (a) two like charges and (b) two opposite charges.

If two oppositely charged plates are brought close to each other, the space between them will be filled almost perfectly with an electric field orthogonal to both surfaces, as shown in Figure 1.2. This geometry is important because the PMN-PT stack used in the test transducer is activated by two charged electrodes like those shown, with the material itself lying in the space between the two plates.

1.3.2 Electric Flux and Gauss' Law

Suppose that an arbitrarily shaped object is placed in an electric field. Depending upon the location of this object relative to the field, lines will be passing through the surface of the object as shown in Figure 1.3. The rate of this “flow” through the surface, known as the flux, is determined from

$$\Phi = \sum \vec{E} \cdot \Delta \vec{A} \quad (1.2)$$

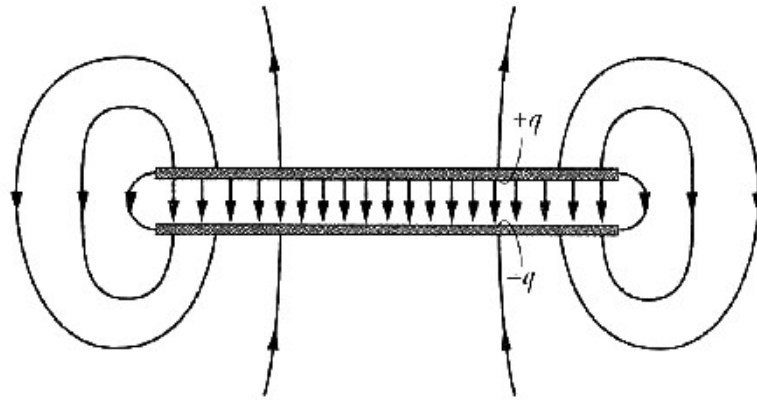


Figure 1.2: Electric field for oppositely charged plates [13].

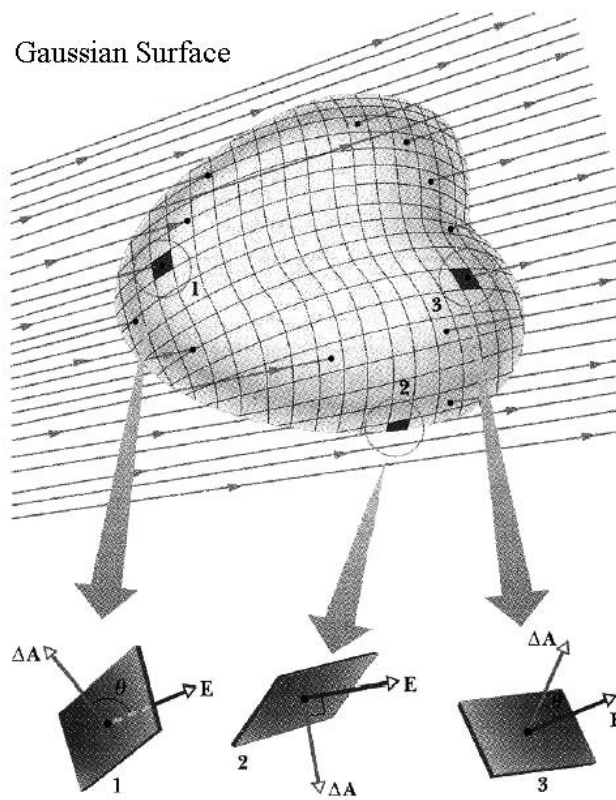


Figure 1.3: Electric field through a Gaussian surface [13].

where Φ is the net flux, \vec{E} is the electric field vector, and $\Delta\vec{A}$ is the normal vector to each finite piece of surface area. Gauss' law relates the net flux of an electric field through a closed surface to the net charge q_{enc} that is enclosed by that surface. Assuming that the flux approaches a differential limit and becomes an integral, then (1.2) becomes

$$\kappa\epsilon_0 \oint \vec{E} \cdot d\vec{A} = q_{enc}, \quad (1.3)$$

where κ is known as the dielectric constant and is a scaling factor for the permittivity based on the type of surrounding medium.

Gauss' law states that any closed surface surrounding a net positive charge will have some net flux flowing outward, while one surrounding a net negative charge will have an inward flux. An object enclosing no charge or zero net charge will have zero net flux, which means as many field lines enter the object as leave it.

1.3.3 Polarization

The electric dipole consisting of two oppositely charged particles has a corresponding moment vector \vec{p} , which points in the direction from negative to positive. When this dipole is placed in an electric field, a torque will be generated acting to align the moment with the field vector \vec{E} . An example of this effect is shown in Figure 1.4. The magnitude and direction of the torque vector can be found from

$$\vec{\tau} = \vec{p} \times \vec{E},$$

with the right hand rule applying as usual. When the dipole is completely aligned with the applied field it has no torque and is in equilibrium.

Ideal dipoles made from discrete particles are convenient but unrealistic. In real materials dipoles exist at the atomic level due to the inherent charges and positions of

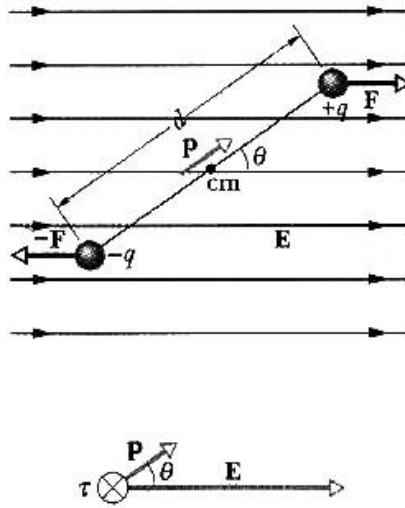


Figure 1.4: Electric dipole moment [13].

the protons and electrons. Normally the centers of the positive nucleus and negative electron shell spatially coincide and thus no dipole moment is set up. In the presence of an external electric field, the electrons can alter their relative position and spin to separate the centers of the positive and negative charges, as in Figure 1.5. This shift induces a dipole moment that points in the direction of the field, and the atom is said to be polarized. If the applied field is removed the induced moment and corresponding polarization disappear as well.

The polarization \vec{P} of a material is defined as the volume density of the electric dipole moments,

$$\vec{P} = \frac{\vec{p}}{V}, \quad (1.4)$$

with V representing the volume of material [4]. In any realistic system there will be a limit to how many dipole moments can be induced by an applied field, and this

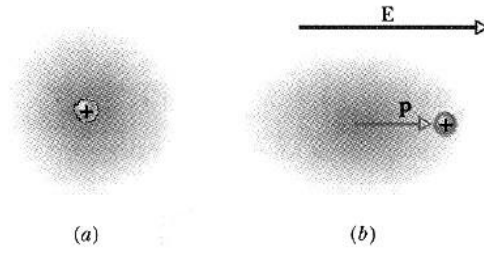


Figure 1.5: Atomic electric dipole induced by applied field [13].

behavior is characterized by the saturation polarization P_s . The polarization will increase in proportion with higher field levels until all available parts are polarized, at which point it will reach the saturation value P_s . This process is illustrated in Figure 1.6, which also depicts the inherent hysteresis.

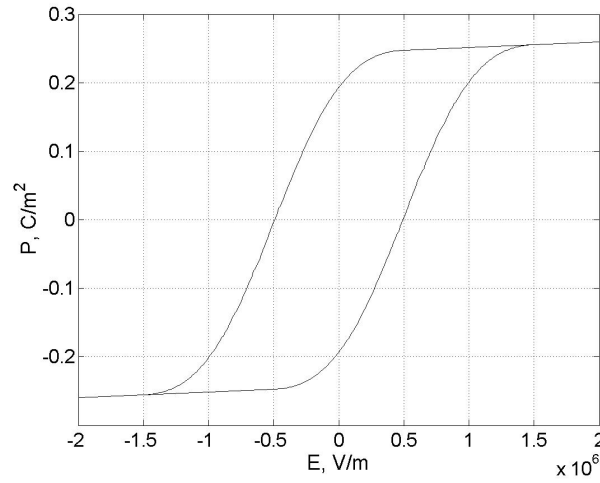


Figure 1.6: Polarization versus electric field for a typical piezoceramic.

1.3.4 The Magnetic Field

For all of the previously discussed electric phenomena, there are analogous magnetic phenomena that must be reviewed. The fundamental connection between electricity and magnetism is that an electric charge in motion, known as a current, generates a magnetic field in a surrounding medium. Like the electric field, the magnetic field is a vector quantity with a defined magnitude and direction at each point in space. The direction of the field is defined by the right hand rule, with the thumb pointing in the direction of the current and the curl of the fingers showing the magnetic field path. Consequently, a field loop is formed around a straight conductor as shown in Figure 1.7(a). However, more useful fields are generated when the current travels in a circular loop. Stacking these loops into a long coil creates a solenoid that is very commonly used in magnetically activated systems. In addition to currents, permanent bar magnets create magnetic fields due to their inherent magnetization. Figure 1.7 shows the magnetic fields generated by various wire shapes and a permanent magnet.

The intensity of the magnetic field due to an electric current can be determined from the Biot-Savart law,

$$d\vec{H} = \frac{1}{4\pi r^2} i d\vec{l} \times \vec{u}, \quad (1.5)$$

where \vec{H} is the magnetic field, i is the current, $d\vec{l}$ is a length of conductor, and r is the distance to the point in space where the field is being calculated in the direction of unit vector \vec{u} . This equation can be used to calculate the fields produced by coils operating in real transducers as part of a dynamic magnetic circuit [8]. Figure 1.8 shows the application of the Biot-Savart law to a single current carrying coil.

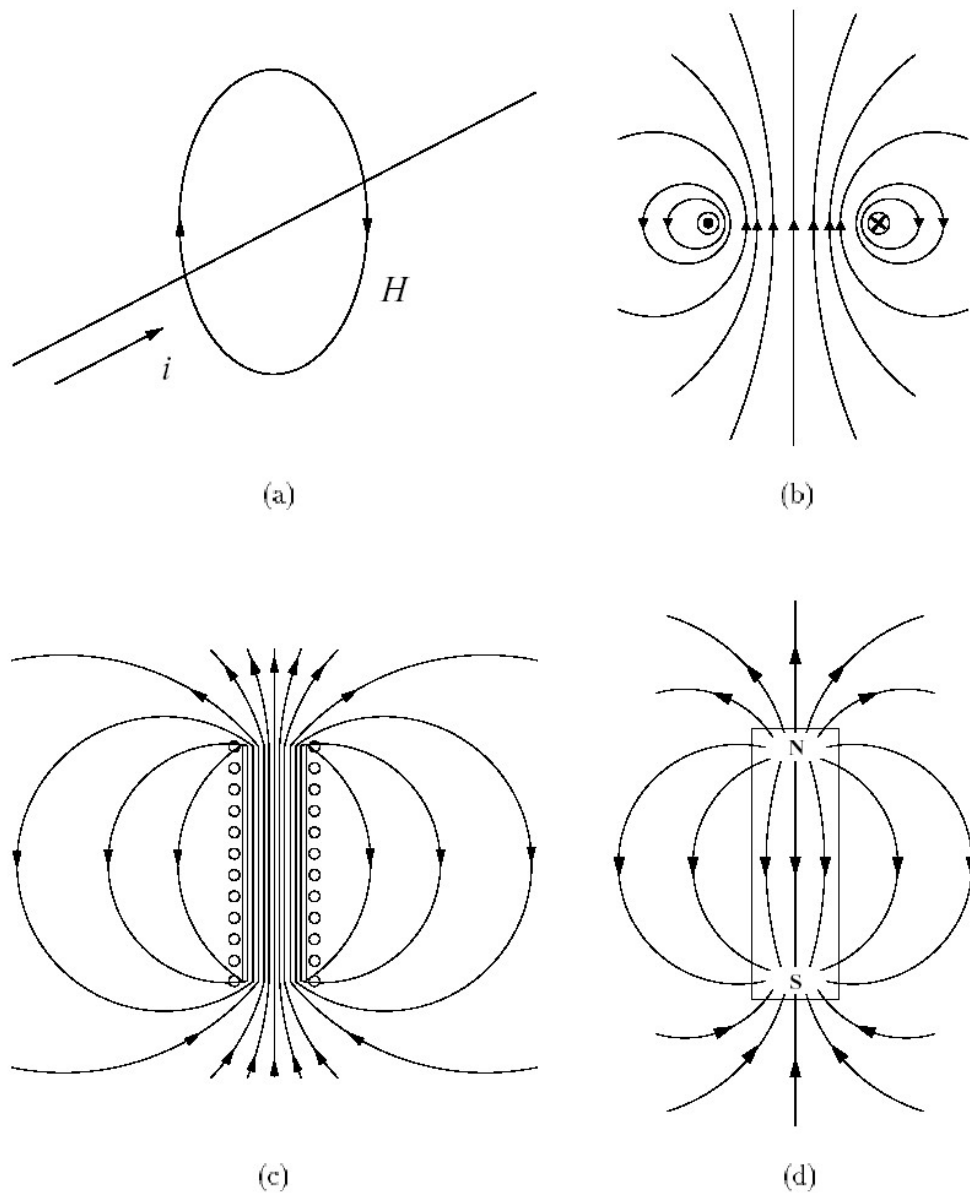


Figure 1.7: Magnetic field lines from: (a) straight line current, (b) single wire loop, (c) solenoid, and (d) permanent bar magnet [8, 19].

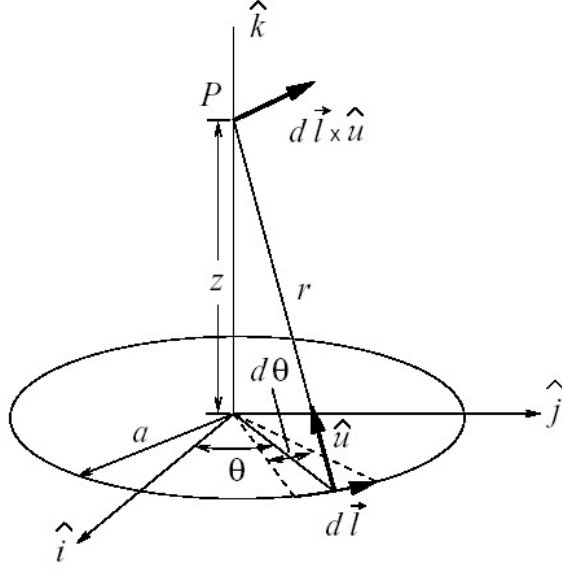


Figure 1.8: Biot-Savart law applied to a single circular coil [8].

The magnetic circuit in this investigation is generated from a solenoid like that depicted in Figure 1.7(c). While the Biot-Savart law can be used to calculate the magnetic field intensity along the axis of a solenoid, off-axis calculations generally lead to equations without closed form solutions. For this reason, thin solenoid approximations are often employed. Assuming a thin solenoid of length L and N turns of wire, the magnetic field is found to be

$$H = \frac{Ni}{L} = ni. \quad (1.6)$$

The field is considered uniform along the length of the solenoid which is an approximation since physical solenoids exhibit leakage and end effect losses. A thick solenoid refers to one with more than one layer of coils, which is useful for generating larger magnetic fields. Magnetic field models for the thick solenoid are usually constructed

from Maxwell's equations in combination with finite element solution approximations. A simpler treatment of thick solenoid has been given by Jiles [18]; for a solenoid of length L , inner radius a_1 , and outer radius a_2 , two parameters are defined that characterize the geometry of the system, $\alpha = a_2/a_1$ and $\beta = L/2a_1$. The field along the axis of the coil is given by

$$\vec{H} = \frac{Ni}{L} \left[\frac{F(\alpha, \beta)}{\alpha - 1} \right],$$

where $F(\alpha, \beta)$ has the form

$$F(\alpha, \beta) = \beta \left[\operatorname{arcsinh} \left(\frac{\alpha}{\beta} \right) - \operatorname{arcsinh} \left(\frac{1}{\beta} \right) \right].$$

The above expression is the most general case for a solenoid, and can be simplified to other familiar cases, e.g. equation (1.6), when certain limits are applied.

1.3.5 Magnetic Induction and Flux

While a magnetic field \vec{H} is generated whenever an electric charge is in motion, the magnetic induction \vec{B} quantifies the response of a medium to the applied field [8]. All media respond to a magnetic field with some induction, the strength of which is related by the permeability μ . The constitutive law that relates magnetic field and magnetic induction is

$$\vec{B} = \mu \vec{H}. \tag{1.7}$$

It is noted that the permeability is actually a variable property dependent on several factors such as the intensity of the field, applied stress, and temperature. For calculation purposes involving experimental data the differential permeability is often used,

$$\mu = \frac{dB}{dH}.$$

It is useful in some cases to express the permeability as a relative strength compared with the nominal value of $\mu_0 = 4\pi \times 10^{-7}$ H/m for free space. Thus the relative permeability is defined as

$$\mu_r = \frac{\mu}{\mu_0}.$$

The physical implication of μ_r is how much magnetic flux will be induced in a material compared with free space or air ($\mu_{r,air} \approx 1$). For example, iron has a maximum relative permeability of 5200 and thus a solenoid wrapped around it would generate 5200 times more magnetic flux than the same solenoid operating in air.

The connection between magnetic induction and magnetic flux ϕ is that the induction is the flux density in the material. Physically the flux lines always close, as in Figure 1.7, but in some areas they will be more densely packed than in others. Therefore, another expression for B can be written as

$$B = \frac{\phi}{A}, \tag{1.8}$$

where A is the cross-sectional area through which the flux lines traverse.

One relation between magnetism and electricity lies in that an electromotive force is induced in a coil when the magnetic flux through it changes. The Faraday-Lenz law states that the voltage induced in a coil is proportional to the rate of change of flux through the coil and that the direction of the induced voltage opposes the flux change producing it. This is written as

$$V = -N \frac{d\phi}{dt}, \tag{1.9}$$

where N is the number of turns in the coil. From equations (1.8)-(1.9), the magnetic induction can be expressed as

$$B = -\frac{1}{NA} \int V dt, \tag{1.10}$$

which can be used for measuring the induction in a medium. Typical transducer design incorporates a thin pickup coil wrapped around a magnetic core from which the voltage induced by changing magnetic flux can be read. This voltage signal can then be integrated to obtain B .

1.3.6 Magnetization

Magnetization in a material is due to the development of magnetic moments on the atoms, with the net magnetic moment \vec{m} being a combination of both orbital and spin magnetic moments. These moments are analogous to those induced by electric dipoles, as they will align with an externally applied induction. The equation quantifying the torque $\vec{\tau}$ on a moment induced by a magnetic field with induction B is given by

$$\vec{\tau} = \vec{m} \times \vec{B}.$$

The magnetization \vec{M} of a magnetic material is defined as the volume density of magnetic moments,

$$\vec{M} = \frac{\vec{m}}{V}, \quad (1.11)$$

where V is the volume of material [8]. In the absence of an external magnetic field, such as in a permanent bar magnet with an internal magnetization, induction will still be generated in the material due solely to \vec{M} . Assuming a medium of air, this is found to be

$$\vec{B} = \mu_0 \vec{M}, \quad (1.12)$$

which is analogous to (1.7). The total magnetic induction then consists of two contributions, one from the applied field and one from the magnetization. The vector

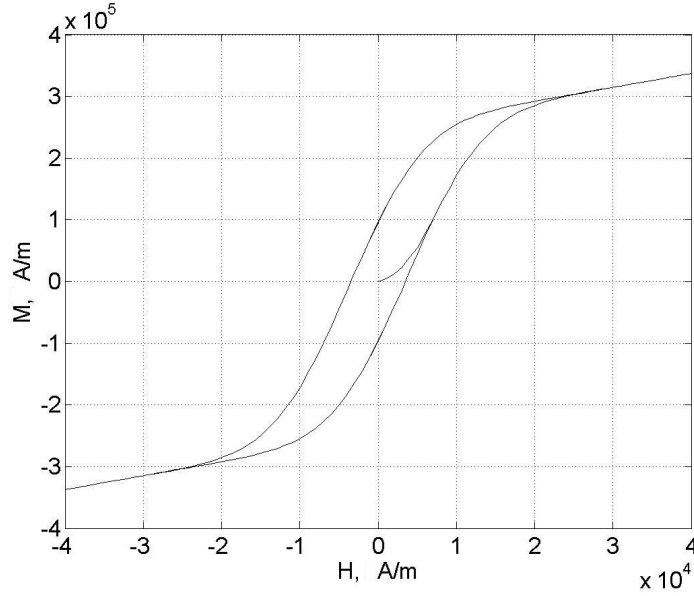


Figure 1.9: Magnetization versus magnetic field for a typical ferromagnetic material.

sum of these quantities yields the expression

$$\vec{B} = \mu_0 (\vec{H} + \vec{M}).$$

As the magnetization increases in a material, the magnetic moments will further align with the applied field until all the magnetic moments are aligned parallel. This state is termed the saturation magnetization M_s and is achieved when the entire material has converted to a single magnetic domain. An example of the relation between the magnetization and magnetic field, along with the effects of hysteresis and saturation, is shown in Figure 1.9.

1.3.7 Maxwell's Equations

A set of equations developed by James Maxwell provide a complete unified description of all electromagnetic phenomena. The description is based on the work of

Gauss, Ampère, Faraday, and Lenz. Maxwell’s own contribution is the concept of “displacement currents,” which generalizes Ampère’s law to include high frequency wave propagation.

The formulation of Maxwell’s equations concisely relate the fundamental electromagnetic fields: the electric field \vec{E} , electric flux density \vec{D} , magnetic field \vec{H} , and magnetic induction \vec{B} . The four differential equations are

$$\begin{aligned}\nabla \cdot \vec{D} &= q && \text{(Gauss' law for electric flux)} \\ \nabla \cdot \vec{B} &= 0 && \text{(Gauss' law for magnetic flux)} \\ \nabla \times \vec{E} &= -\frac{\partial \vec{B}}{\partial t} && \text{(Faraday-Lenz law of induction)} \\ \nabla \times \vec{H} &= \vec{J} + \frac{\partial \vec{D}}{\partial t} && \text{(Maxwell's form of Ampère's law)}\end{aligned}$$

where \vec{J} is the surface current density that generates the magnetic field, and ∇ is the vector derivative operator.

The first equation is a different expression for Gauss’ law, equation (1.3), but is mathematically and physically equivalent. The second equation is Gauss’ law applied to magnetic flux, which states that lines of magnetic flux always close and thus that flux is conserved. This is readily verified by looking at the lines in Figure 1.7. This is particularly important for magnetic circuits because it implies that applying a field to one component in the system will magnetize all other components as the flux moves through.

Maxwell’s third equation is a reinterpretation of the Faraday-Lenz law from (1.9). It states that the curl of the electric field is determined by the rate of change of the magnetic induction and that it points in the opposite direction. The last equation contains the “displacement current” term $\frac{\partial \vec{D}}{\partial t}$ which is negligibly small at low to moderate frequencies. In this case, the equation simplifies to Ampère’s circuital law

which in integral form is expressed as

$$\oint_{\partial\Omega} \vec{H} d\vec{l} = Ni, \quad (1.13)$$

where there are N conductors, each carrying current i , within the boundary $\partial\Omega$. This law is equivalent to the Biot-Savart relation (1.5), and this is easily seen in the case of a long thin solenoid where equation (1.13) reduces to $H = Ni/L$, identical to the form derived in (1.6).

1.4 Fundamental Concepts of Electric Circuits

The previous section detailed concepts from electric and magnetic fields but ignored the overall scheme in which they are generated. For this an overview is presented (based on Rizzoni [29]) of electric circuits and how each component fits into the overall smart material system.

1.4.1 Resistance, Capacitance, and Inductance

An electric circuit is a closed path consisting of an energy source (typically voltage) connected to a combination of loads, the three types of which are the resistor, capacitor, and inductor. Each is governed by a distinct expression quantifying the relation between voltage across and current through that element. The resistor relationship is defined by Ohm's law,

$$V = iR, \quad (1.14)$$

where R is the resistance, V is the voltage potential across the load, and i is the current flowing through it. Resistance is present in all practical circuit components, including the wire path and any practical sources, and represents the energy dissipation in the circuit.

The ideal capacitor is a device that stores energy in the form of an electric charge potential, with the value of the capacitance C being the proportionality between voltage and charge, $q = CV$. The fact that the current is the rate of change of charge converts this into the more useful circuit form

$$i(t) = C \frac{dV}{dt}. \quad (1.15)$$

The capacitance value itself depends only upon the geometry of the device, with the form of primary interest being two parallel plates like those of Figure 1.2. Using Gauss' law the charge on either plate can be written as $q = \kappa\epsilon_0 EA$ with area A , and by definition the voltage and electric field are related by $V = Ed$ where d is the distance between the plates. Combining these expressions with the definition of capacitance yields

$$C = \frac{\kappa\epsilon_0 A}{d}, \quad (1.16)$$

where κ is once again the dielectric constant of the material located between the two plates.

The ideal inductor is a wound wire device that can store energy in a magnetic field, with the value of inductance L being the measure of flux linkage produced per unit current. This takes the form $L = N\phi/i$, where N is the number of turns, and ϕ and i are magnetic flux and current as previously defined. Combining this definition of inductance with the Faraday-Lenz law (1.9) yields the useful circuit expression

$$V(t) = L \frac{di}{dt}. \quad (1.17)$$

The duality between capacitance and inductance is recognizable by comparing equations (1.15) and (1.17).

Like the capacitance, the inductance value is dependent only on the geometry of the component. The most common form for an inductor is a solenoid wrapped around a metal core, for which the inductance can be derived using earlier concepts. To this end, equation (1.8) can be used for the flux ϕ and N is simply the turns ratio n times the length L_e . The magnitude B is defined by (1.7), with H of a solenoid taken from (1.6). Substituting these expressions into the definition of inductance yields L of a solenoid,

$$L = \mu n^2 A L_e. \quad (1.18)$$

1.4.2 Impedance

When a combination of resistors, capacitors, and inductors are in a circuit, all of the voltages and currents of interest can be found by implementing the relations (1.14), (1.15), and (1.17). An alternate approach with widespread applicability to this research is to utilize the complex impedance. Rewriting Ohm's law in the form

$$V = iZ, \quad (1.19)$$

Z is now a generalized impedance and all three variables can be complex. This defines Z of any electric circuit component to be the ratio of its voltage and current. Looking first at the resistor, the identical form of equations (1.14) and (1.19) allows the impedance of the ideal resistor to be easily written as

$$Z = R. \quad (1.20)$$

For the two energy storage elements the differential relations in (1.15) and (1.17) need to be converted into a more useful form. Applying the Laplace transform to the

capacitance equation allows for conversion into the frequency domain,

$$\mathcal{L} \left\{ i(t) = C \frac{dV}{dt} \right\} \Rightarrow I(s) = CsV(s),$$

where $I(s)$ is the transform of $i(t)$, $V(s)$ is the transform of $V(t)$, and s is the Laplace derivative operator $j\omega$. With this expression the impedance of a capacitor is by definition

$$Z = \frac{1}{Cs}. \quad (1.21)$$

Repeating the above procedure for an inductor yields

$$\mathcal{L} \left\{ V(t) = L \frac{di}{dt} \right\} \Rightarrow V(s) = LsI(s),$$

from which the impedance is written as

$$Z = Ls. \quad (1.22)$$

Because each device's impedance has a different frequency proportionality, most electrical devices can be characterized as either resistive, capacitive, or inductive based on its measured impedance.

The usefulness of this impedance notation comes from the fact that various loads of all types can be easily combined using two basic rules. Impedances in series, which share a common current, sum normally to a single equivalent,

$$Z_{eq} = \sum_{n=1}^N Z_n.$$

The other possible configuration is when the impedances are arranged in parallel and subjected to the same voltage. These combine using the relation

$$\frac{1}{Z_{eq}} = \sum_{n=1}^N \frac{1}{Z_n}.$$

Any circuit with various series and parallel loads can be easily analyzed by combining impedances wherever necessary.

1.5 Fundamental Concepts of Dynamic Systems

Dynamic systems in general contain energy storage elements from one or more regime, and react to applied inputs with some output response [25]. Electrical, mechanical, thermal, and hydraulic systems can all behave in a similar manner. This thesis is focused on the mechanical regime which will be used to describe the transducer vibrations.

1.5.1 Mechanical Systems

Mechanical systems, just like the electric circuit, can be analyzed through three types of elements: inertias (masses or rotational moments), dampers (energy dissipators), and compliances (stiffnesses). The basic mechanical system shown in Figure 1.10(a) contains all three of these components. The one end of the spring and damper are considered fixed, while the mass m is constrained to move only in the x direction. The free body diagram in Figure 1.10(b) shows the components broken down into their applied forces. To analyze this system, Newton's second law is applied,

$$\sum \vec{F} = m\vec{a}, \quad (1.23)$$

with \vec{F} the individual vector force contributions, m the mass (inertia) of the object, and \vec{a} the acceleration. Applying (1.23) to the system in Figure 1.10, the following equations are generated,

$$\sum F = F_{\text{applied}} + F_{\text{spring}} + F_{\text{damper}} = F_{\text{applied}} - kx - bv = ma, \quad (1.24)$$

where the force directions are determined from sign convention.

Rewriting equation (1.24) in terms of $x(t)$ and its derivatives gives

$$m\ddot{x} + b\dot{x} + kx = F_{\text{applied}}, \quad (1.25)$$

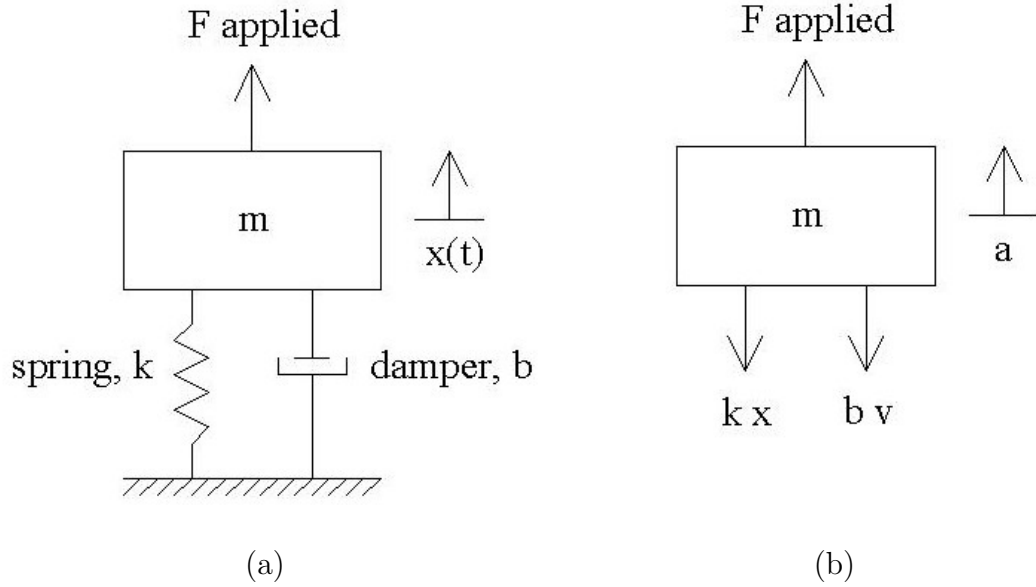


Figure 1.10: One degree of freedom mechanical system as (a) schematic and (b) free body diagram.

which is known as the differential equation of motion for the system [21]. Using standard mathematical techniques, this differential equation can be solved for the displacement $x(t)$ for any input forcing function.

It is possible to relate the equation of motion (1.25) with an electric circuit if some parallels are drawn. The current flow in a circuit is analogous to the mechanical velocity while the driving voltage potential is analogous with the externally applied force. In this context, the mechanical impedance can be defined as F/v , just as the electrical impedance is defined as V/i . Taking the Laplace transform yields

$$ms^2X(s) + bsX(s) + kX(s) = F(s),$$

from which the impedance can be written as

$$Z_{mech} = \frac{F}{v}(s) = \frac{F}{sX}(s) = ms + b + \frac{k}{s}.$$

The last step in completing the electrical-mechanical analogy is recognizing that Z_{mech} is equivalent to an electrical impedance consisting of a series combination of an inductor, resistor, and capacitor. Thus it is concluded that m is analogous to L , b to R , and k to $\frac{1}{C}$. The benefit of this comparison is that in multi-regime devices both electrical and mechanical components can be described by complex impedances and combined in the same manner.

The presence of the s^2 term in the transformed equation of motion means that this is known as a second-order system. Typically this will result from the inclusion of two different energy storage elements, in this case the mass and the spring. Regardless of the energy regime, any second-order system like equation (1.25) can be rewritten in the standard form

$$\left(\frac{1}{\omega_n^2} s^2 + \frac{2\zeta}{\omega_n} s + 1 \right) X = \frac{F}{k}, \quad (1.26)$$

where $\omega_n = \sqrt{k/m}$ is the resonance frequency and $\zeta = b/2\omega_n$ is the dimensionless damping factor. The resonant frequency is the frequency at which the system would naturally oscillate if allowed to do so freely, whereas the damping coefficient controls how these oscillations die out. The physical connotations of these terms are discussed in the next section.

1.5.2 Frequency Response

Complete dynamic systems as well as individual components are characterizable by an input-output relationship called a transfer function. This description relates

the system output to the input driving function by a ratio of frequency domain equations. For example, if in (1.26) the force F is considered the input and the displacement X the output, then the transfer function is $\frac{X}{F}(s)$, which can easily be solved for algebraically. A transfer function is a mathematical model of the dynamic characteristics of a physical system, and is a property of that system independent of the nature of the input and output [25]. If the transfer function of a system is known then the response to any distinct input signal can be calculated.

Recognizing that $s = j\omega$, the transfer function is a complex function of frequency containing both a real and imaginary part, or alternatively a magnitude and phase. The basic form examined thus far is

$$G(s) = \frac{X}{F}(s) = \frac{1}{\frac{1}{\omega_n^2}s^2 + \frac{2\zeta}{\omega_n}s + 1},$$

which in terms of frequency is

$$G(j\omega) = \frac{1}{1 - \left(\frac{\omega}{\omega_n}\right)^2 + j2\zeta\frac{\omega}{\omega_n}}. \quad (1.27)$$

This expression is a measure of the system response to an excitation of frequency ω which is why $G(j\omega)$ is called the frequency response function. Utilizing the concept of the complex conjugate $\bar{G}(j\omega)$ and complex algebra, the frequency response can be expressed in terms of magnitude,

$$|G(j\omega)| = \frac{1}{\sqrt{\left[1 - \left(\frac{\omega}{\omega_n}\right)^2\right]^2 + \left(\frac{2\zeta\omega}{\omega_n}\right)^2}}, \quad (1.28)$$

and phase,

$$\phi(\omega) = \arctan\left(\frac{\frac{2\zeta\omega}{\omega_n}}{1 - \left(\frac{\omega}{\omega_n}\right)^2}\right). \quad (1.29)$$

Insight into system behavior can be obtained by examining both the magnitude and phase functions with respect to frequency [21]. From the denominator of equation (1.28), as ω approaches ω_n , the real term goes to zero and the denominator is a minimum, implying that the total magnitude $|G(j\omega)|$ is a maximum. Thus at resonance the system responds with a maximum output, seen as the peak in Figure 1.11(a). This figure also shows how the relative magnitude achieved at this point is determined by ζ , as more damping will result in a wider and flatter peak output. Finally, the points ω_1 and ω_2 are the half power point frequencies, where the magnitude is $\sqrt{2}/2$ times that at resonance which correlates to half the power output. In real systems where the damping ratio is difficult to calculate, the half power points provide an approximate measure of ζ and the related quality factor Q through the expression

$$\zeta \simeq \frac{1}{2Q} \simeq \frac{\omega_2 - \omega_1}{2\omega_n}. \quad (1.30)$$

As for the phase, resonance is the point where the system response shifts from being in phase ($\phi \sim 0$) to out of phase ($\phi \sim 180^\circ$) with the excitation, as shown in Figure 1.11(b). Note that at the resonant frequency ω_n , the phase is exactly 90° . Once again, an increase of damping in the system results in a more dispersed phase transition.

For a multi-degree of freedom system, natural vibration implies not only a resonance frequency but also a natural configuration of the masses. Such system will possess several different equations of motion, each typically being a second-order system itself. Therefore the overall multi-degree of freedom structure will have as many natural modes as degrees of freedom, where each mode consists of a resonance frequency and mass configuration [21].

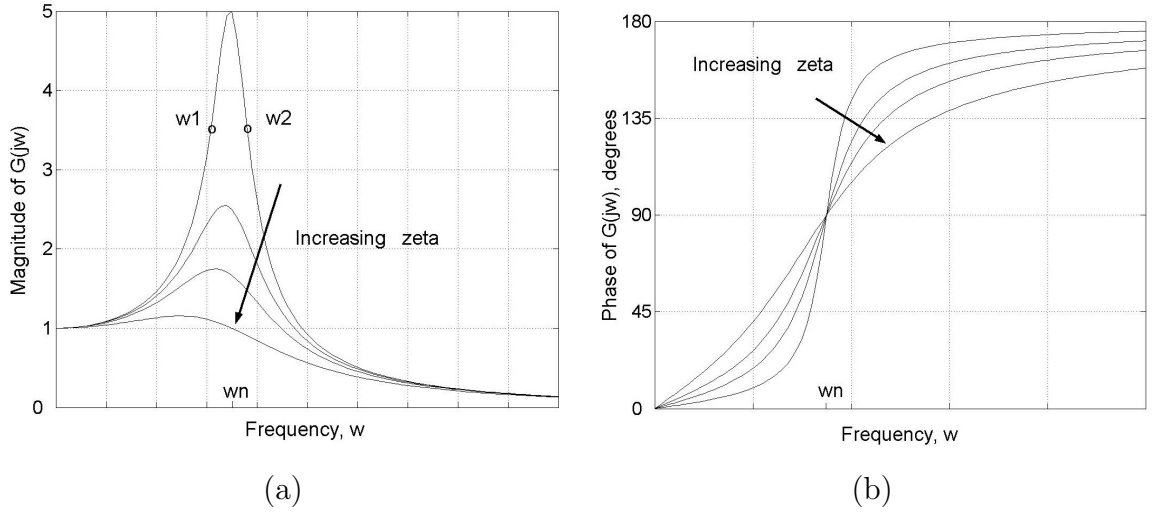


Figure 1.11: Frequency response of $G(j\omega)$ as (a) magnitude and (b) phase.

Modal analysis is the technique of identifying the natural modes through the eigenvalues and eigenvectors. When the multitude of equations of motion are written in matrix form, there will be distinct mass M and stiffness K matrices that contain all of the physical constants of the system. The total system is then described by

$$[M]\ddot{x} + [K]x = 0$$

without damping and external forces. Applying the Laplace transform and rearranging terms gives

$$\lambda x = [M]^{-1}[K]x,$$

where this expression is called the characteristic equation and the conversion $\lambda = \omega^2$ is used. The solutions of this are known as the eigenvalues λ_i from which the various natural frequencies are found by $\omega_{n,i} = \sqrt{\lambda_i}$. Substituting these frequencies back into the system equations allows the corresponding mode shapes, or eigenvectors \vec{u} , to

be found by solving for x . The benefit of this is that the values in each eigenvector represent the relative directions of each mass in that natural mode, meaning that the eigenvector defines the mode shape.

Overall the concepts of resonance, vibration modes, and frequency response are vital to the design and modeling of a broadband transducer. The universality of the impedance method for characterizing both electrical and mechanical devices is also necessary in allowing for an elegantly concise description of the multi-regime coupling. These ideas will be fully developed in Chapters 2 and 3.

CHAPTER 2

LINEAR TRANSDUCER MODEL

2.1 Material Background and Constitutive Relations

The electric field-actuated smart material used in the hybrid transducer is lead magnesium niobate - lead titanate, $(\text{Pb Mg}_{\frac{1}{3}} \text{Nb}_{\frac{2}{3}} \text{O}_3)_{0.65} - (\text{Pb Ti O}_3)_{0.35}$, known as PMN-PT. The complementary magnetic field-actuated smart material is the magnetostrictive compound terbium-iron-dysprosium $(\text{Tb}_{0.73} \text{Dy}_{0.27} \text{Fe}_{1.95})$. In order to design and model a system using these materials, it is necessary to understand the basic concepts of piezoelectricity and magnetostriction.

2.1.1 Piezoelectric and Ferroelectric Materials

Piezoelectricity is defined as the electric polarization produced in a material by an applied mechanical stress. Closely related to this is the converse effect where a piezoelectric crystal is deformed when electrically polarized. Both are manifestations of the same fundamental property. The direct effect was discovered by the Curie brothers in 1880 [4, 15, 16, 20] while investigating temperature related effects (pyroelectricity) in combination with mechanical pressure on various crystals. In the year following their discovery, Lippmann predicted the existence of the converse effect,

and the Curie brothers soon verified this phenomenon as well [4]. For several years after these discoveries, piezoelectricity was largely ignored by the scientific community until the first world war, when it was demonstrated that quartz crystals could be used in oscillatory applications ranging from sonar to radio transmitters [20]. In all of these cases, a single crystal was typically used since more advanced manufacturing techniques were not available. By the late 1940's the process of poling was introduced which allowed for polycrystalline compounds such as ceramics to be used in piezoelectric applications [16]. The most popular piezoceramic still in wide use today is lead zirconate titanate (PZT), of which several grades and compositions exist.

The nature of the piezoelectric phenomenon is dependent on the ability of the crystal to respond in the direction of the applied stress or field and to be reversible upon their removal. For the piezoelectric interaction to exist it is necessary that the medium intrinsically possess a directionality in its crystallographic structure, referred to as anisotropy [16]. Such crystallographic ordering allows for the reversal of strain with alternating fields and distinguishes piezoelectricity from electrostriction. Electrostriction is similar to the converse piezoelectric effect, but the deformation is proportional to the square of the applied field rather than linearly dependent, and thus it is independent of the field direction.

More recent studies have revealed the benefit of combining relaxor ferroelectrics with piezoceramics to create a new class of material [30]. Ferroelectricity is defined as the presence of a spontaneous electric dipole moment in a crystal that can change its orientation between distinct directions by an externally applied field [16]. A material can be made to exhibit this behavior through the process of poling, which is the concept that bridges classical single crystal piezoelectrics to the modern piezoceramics.

A polycrystalline material such as a ceramic is an agglomeration of small crystals that are grown in random orientations during manufacturing. The method of poling a material consists of applying a very strong electric field such that the random polar axes are reoriented along easy polarization axes closest to the field direction. The resultant crystallographic structure resembles a single piezoelectric crystal with a net dipole moment and responds as such to stress and field inputs. There exists a depolarizing threshold in both stress and field, but so long as the material is never subjected to these thresholds it will remain poled practically forever. Ferroelectric properties are quite sensitive to thermal effects and often must be operated in a narrow band about room temperature.

In many applications, polycrystalline ferroelectric piezoceramics have replaced single crystal compounds. Lead zirconate, the basis for PZT, is an example of a “normal” ferroelectric ceramic produced with the poling technique. Relaxor ferroelectrics are a class of materials that exhibit a broad and dispersive phase transition [30]. The largest family of such materials is the complex lead based perovskites, of which PMN is a member. When these materials are combined with lead titanate (PT), the resultant crystal structure will vary based on the volume fraction of each compound present. Ferroelectric ceramics have been shown to exhibit anomalously large piezoelectric and dielectric properties at compositions near a morphotropic phase boundary (MPB), which is the transition where the crystallographic structure changes from rhombohedral to tetragonal [26]. Each of these crystal structures has a different easy axis, $[0\ 0\ 1]$ for the tetragonal and $[1\ 1\ 1]$ for the pseudo-cubic rhombohedral phase [16]. An example of the morphotropic phase boundary is shown in Figure 2.1, where the crystallographic phases are detailed for both PZT and PMN-PT compounds.

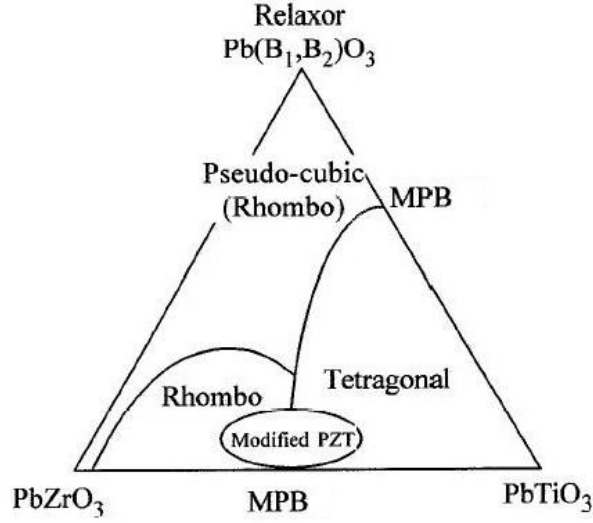


Figure 2.1: Ternary phase diagram of PZT and Relaxor-PT piezoceramics showing morphotropic phase boundaries [26].

The axes separating the three ferroelectric ceramics represent fractional amounts in blends between them (not to scale). Most PZT compounds come from the region near the MPB, as do relaxor based materials such as PMN-PT. The compositions near the MPB have good properties as a result of enhanced polarizability arising from the coupling between the tetragonal and rhombohedral states, allowing efficient reorientation during the poling process [26].

Now the focus is placed solely on the PMN-PT. Figure 2.2 is a detailed plot showing the dependence of the morphotropic phase boundary with PT content and temperature. The transducer employed in this study is operated exclusively at room temperature so thermal effects are ignored. Figure 2.2 shows that pure PMN is electrostrictive in nature but becomes increasingly piezoelectric as it nears the MPB

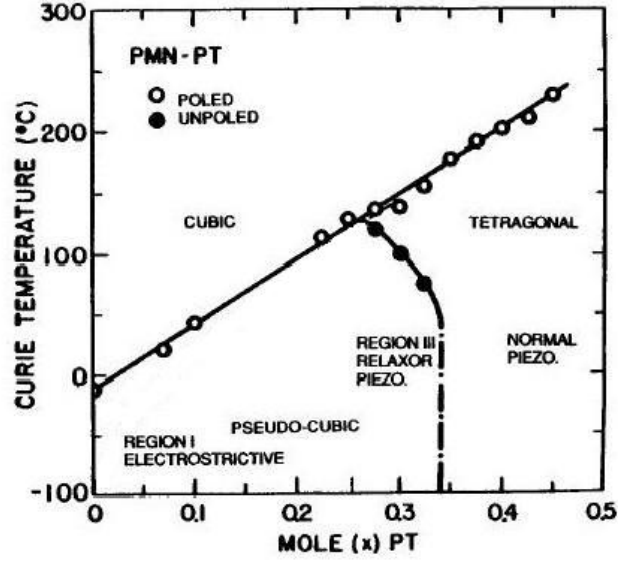


Figure 2.2: Phase diagram showing the morphotropic phase boundary region for the $(1-x)\text{PMN}-(x)\text{PT}$ solid solution system [30].

at 33% PT. The 35% PT compound used in this investigation is purely piezoelectric with strong properties due to its proximity to the morphotropic phase boundary.

2.1.2 Linear Piezoelectric Modeling

The direct and converse piezoelectric effects are often modeled as a pair of linear equations which account for the superposition of elastic, electric, and thermal effects on the strain and electric flux density. The assumed linear relationship between the variables is accurate for low to moderate levels of stress and electric field but does break down at higher regimes. In addition, piezoceramic materials exhibit hysteresis effects, which in linear models can be partially addressed only through laborious

experimental look-up tables. The differential first order form of the model is

$$\begin{aligned} d\varepsilon &= \left(\frac{\partial \varepsilon}{\partial \sigma} \right)_{E,T} d\sigma + \left(\frac{\partial \varepsilon}{\partial E} \right)_{\sigma,T} dE + \left(\frac{\partial \varepsilon}{\partial T} \right)_{E,\sigma} dT \\ dD &= \left(\frac{\partial D}{\partial \sigma} \right)_{E,T} d\sigma + \left(\frac{\partial D}{\partial E} \right)_{\sigma,T} dE + \left(\frac{\partial D}{\partial T} \right)_{E,\sigma} dT, \end{aligned}$$

where ε is the strain, D is the electric flux density, E is the applied field, T is the absolute temperature, and σ is the axial stress [20]. Neglecting the effects of temperature and expressing the partial derivatives as real coefficients leads to

$$\varepsilon = \frac{\sigma}{E_y^E} + d_{33}E \quad (2.1)$$

$$D = d_{33}^*\sigma + \epsilon_0^\sigma E, \quad (2.2)$$

where E_y^E is the Young's modulus at constant field, ϵ_0^σ is the permittivity at constant stress, and d_{33} and d_{33}^* are the electroelastic coupling coefficients. The strain equation contains both Hooke's law for elastic materials $\sigma = \varepsilon E_y$ and the converse piezoelectric effect $d_{33}E$. The second equation characterizes the electric flux density as the sum of the direct piezoelectric effect $d_{33}\sigma$ and the inherent electrical component $\epsilon_0 E$. It is typically assumed that $d_{33} = d_{33}^*$. Equations (2.1)-(2.2) are used as a foundation for the full transducer model presented in Section 2.2.5 and in Chapter 3.

2.1.3 PMN-PT Transducers

In this investigation, the system consists a broadband sonar transducer incorporating a prebuilt PMN-PT stack actuator connected in mechanical series with a magnetostrictive rod. One major benefit of the conventional cylindrical stack configuration for piezoceramics is that the material has already been configured for activation and can be installed without any additional accessories. This stack is made by layering thin circular discs of ceramic between opposite electrodes wired such that the voltage

is equal across all layers. When a voltage is applied, the electrodes generate an electric field that completely and uniformly penetrates the ceramic and induces strain in the thickness direction (d_{33} actuation). Stack actuators generally are compact, come in a variety of sizes, and exhibit high energy densities.

Since each individual ceramic layer is sandwiched between two thin electrodes, the geometry is identical to that of a parallel plate capacitor (see Chapter 1). The ceramic inside of the electrodes acts as a dielectric material, modifying the nominal permittivity ϵ_0 by the constant κ , and the resulting capacitance value is as given in equation (1.16). The entire stack can be modeled as a single capacitance in the overall electrical circuit, with the piezoelectric effect providing a means for coupling the electrical and mechanical regimes.

The mechanical system is also dependent on the PMN-PT stack as it is traditionally used as the stiffness element in vibratory devices. The actual value of this stiffness is approximated as

$$k = \frac{E_y^E A}{t} \quad (2.3)$$

for linear elastic behavior, where k is the stiffness, A is the cross-sectional area, and t is the thickness. This expression is true only for a single ceramic layer but is often extrapolated out to the entire stack when the stiffness contributions of the electrodes are negligible. In addition to acting as a stiffness, the stack provides mechanical damping to the structure through the strain hysteresis. Another mechanical contribution of the piezoceramic stack is that it is responsible for the force generation in the transducer (along with the Terfenol-D rod) in response to electric fields.

Finally, with some poled materials the inherent directionality requires that fields be applied only from zero to peak to avoid negative values that could potentially

depolarize the material. In these cases, if sinusoidal motion is desired, then the “zero” basis for displacement is often shifted to a positive value by the consistent application of a DC electric field or DC bias. This is usually done at the external electric circuit level. In addition, PMN-PT transducers are typically operated under a compressive prestress. This is done to help keep the material in compression at all times where its yield strength is much greater than in tension, and to prealign the dipoles along directions perpendicular to the stack’s 33 direction, leading to more complete rotations, and thus strains, when a field is applied. The means of applying this compressive prestress can vary with the setup, but here Belleville spring washers are used. These springs offer a significant force in a small size, and can be tailored to have a nonlinear stiffness response that minimizes their extraneous dynamic effects.

2.1.4 Magnetostrictive Materials

The term magnetostriction refers to the fractional change in length (strain) that occurs in a ferromagnetic material when subjected to magnetic fields. Magnetostrictive strain is denoted by λ , and is a component of the total elastic strain ε . The phenomenon of magnetostriction was first discovered by Joule in 1842 in samples of iron [8, 13, 19]. Joule noted that when subjected to magnetic fields, these materials underwent a dimensional change as their magnetization was modified. The Villari effect is a reciprocal phenomenon where a stress induced dimensional change will alter a magnetostrictive material’s magnetization. Throughout the early to mid 1900’s, magnetostrictive materials such as iron, nickel, and cobalt were employed in various electromechanical systems such as telephones and sonar devices. Giant magnetostriction, so named because of the substantial increase in possible strains ($\lambda > 1000\mu\varepsilon$),

was discovered in the rare earth elements terbium (Tb) and dysprosium (Dy) but only at extremely low temperatures [19]. In 1971, the U.S. Navy developed an alloy of these two rare metals with iron to create Terfenol-D (the name comes from a combination of TER for terbium, FE for iron, NOL for Naval Ordnance Laboratory, and D for dysprosium), which is a giant magnetostrictive material useable in practical operating conditions. Terfenol-D has been commercially available since the late 1980's and has since grown into an international industry.

Magnetostriction results from the alignment of atomic magnetic moments to form magnetic domains in ferromagnetic materials. The inducing magnetization, and thus the magnetostriction, can change reversibly or irreversibly with the applied field. The reversible magnetization changes are energy conserving while the irreversible effects are dissipative. It is known that the reversible changes exist only at low field levels, and that as the field is increased a transition is made towards irreversibility. Thus a full field cycle will have some magnetization hysteresis, as shown in Figure 1.9.

2.1.5 Magnetostrictive Process

The magnetostrictive process discussed here is actually one of two separate types of magnetostriction. The field induced alignment of magnetic moments occurs only at temperatures below the Curie point, and is the pertinent effect for this investigation. The second class is the spontaneous magnetostriction arising from the alignment of domains when cooling through the Curie temperature [8, 19].

The Terfenol-D rod used in this investigation was manufactured using the free-stand-zone-melt process, resulting in a cubic crystal structure. This structure features a large magnetic anisotropy that dictates the material's preferred magnetic domain

orientation as a result of energy minimization (Figure 2.3). The group of $\langle 1\ 1\ 1 \rangle$ axes are the easy axes that the magnetostrictive anisotropy favors [8, 19]. Isolating the analysis to the $(1\ \bar{1}\ 0)$ plane, one easy axis $[1\ 1\ \bar{1}]$ is closely in line with the overall rod axis. The magnetic domain rotation into this direction is then what causes most of the observable length increase. The other easy axis, $[1\ 1\ 1]$, is nearly orthogonal to the rod axis and 90° from the first easy axis. If a compressive prestress is applied along the primary axis of the rod, it will cause the domains to favor the $[1\ 1\ 1]$ direction, from where a 90° rotation into the $[1\ 1\ \bar{1}]$ by an applied field will generate maximum strain. Thus the prestress allows for enhanced performance with respect to structures in which the initial domains are randomly oriented. An additional use of the prestress is to ensure that the material does not undergo tensile stresses, as its yield strength in tension is only 4% of its strength in compression. A final consequence of the 90° domain rotation is that a field in either direction along the length of the rod will generate a positive magnetostriction.

A more detailed look at the magnetostrictive process in Figure 2.4 shows the material as it progresses from a demagnetized state to a fully saturated one. Panel (a) shows the initial condition where the Terfenol-D domains collectively sum to zero net magnetization. With the application of magnetic field H in Panel (b), the domains more closely aligned with the field grow at the expense of those less favorably oriented, termed domain wall motion. As the field increases in strength in Panel (c), the material becomes a single magnetic domain and rotates into the easy $[1\ 1\ \bar{1}]$ axis nearly aligned with H . Once the field is increased further the domain rotates fully into alignment with the field in the $[1\ 1\ \bar{2}]$ direction, and saturation has been reached in Panel (d). At this point if the field is removed but not reversed, then the domains

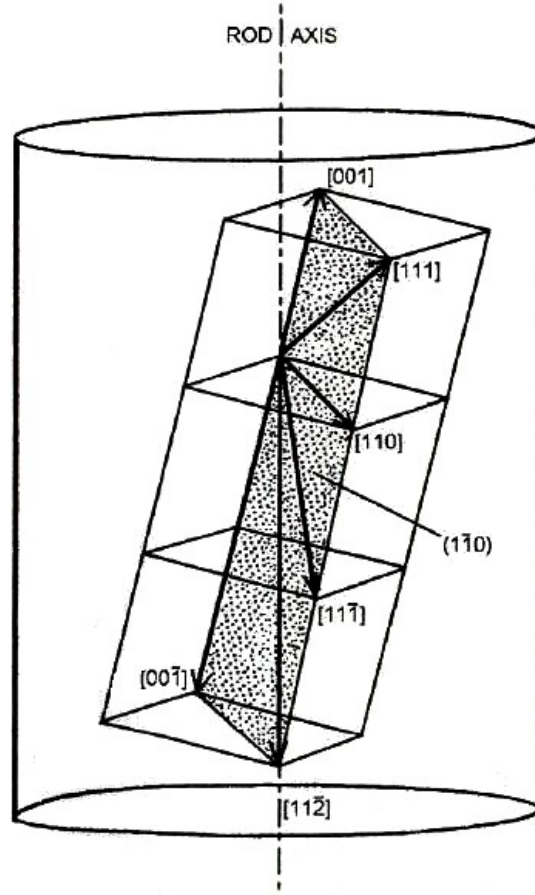


Figure 2.3: Crystallographic structure of Terfenol-D [8, 19].

will return to the nearest easy axis of $[1\ 1\ \bar{1}]$ as in Panel (c). A fully reversed field is required to rotate the domain out of this configuration and generate cyclic strains.

Another graphical representation of this phenomenon is depicted in Figure 2.5. Both magnetization and magnetostriction slowly increase from zero due to the early domain wall motion. Once the large magnetic domain rotates into easy axes, a large increase in both M and λ is seen. The final stage yields little increase from saturation. One consideration when employing practical magnetostrictive materials in

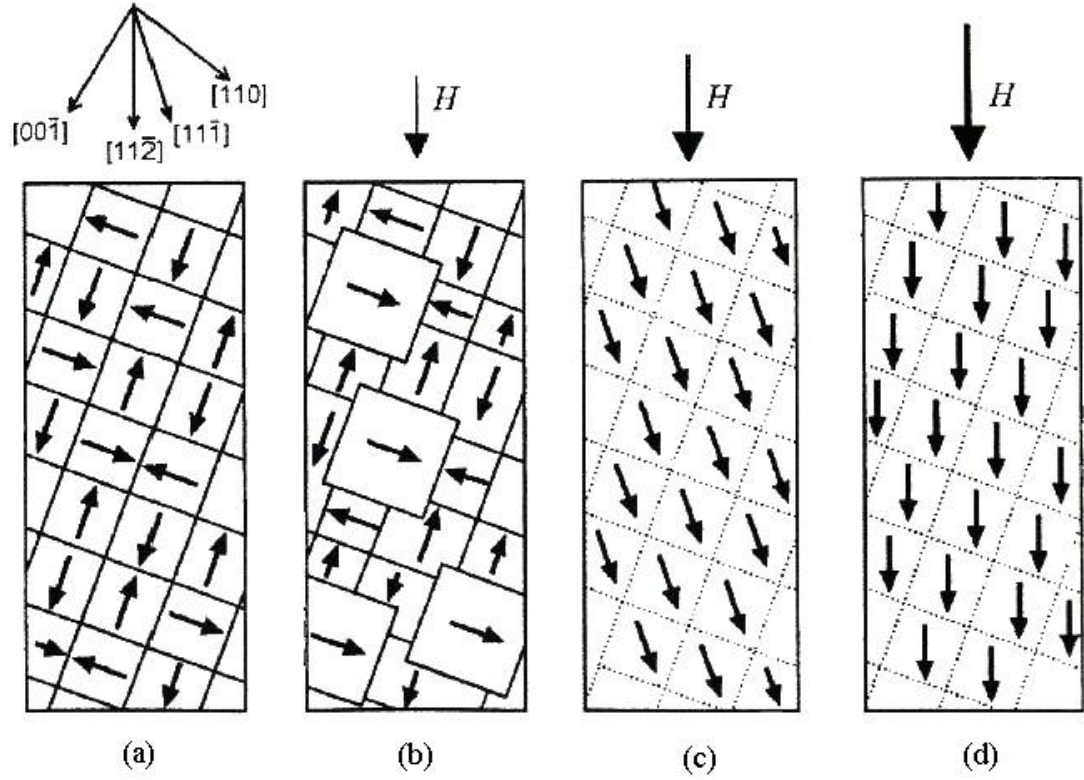


Figure 2.4: Magnetostriction process arising from the application of field H [8, 19].

transducers is that they exhibit magnetostriction hysteresis, as illustrated in Figure 2.6 for Terfenol-D. Another important issue is that the material properties, and thus the entire magnetostriction process, are significantly affected by external stress and temperature.

2.1.6 Linear Magnetostrictive Modeling

Although the magnetostrictive process has been shown to be nonlinear and hysteretic, a set of coupled linearized equations are sufficiently accurate to describe the

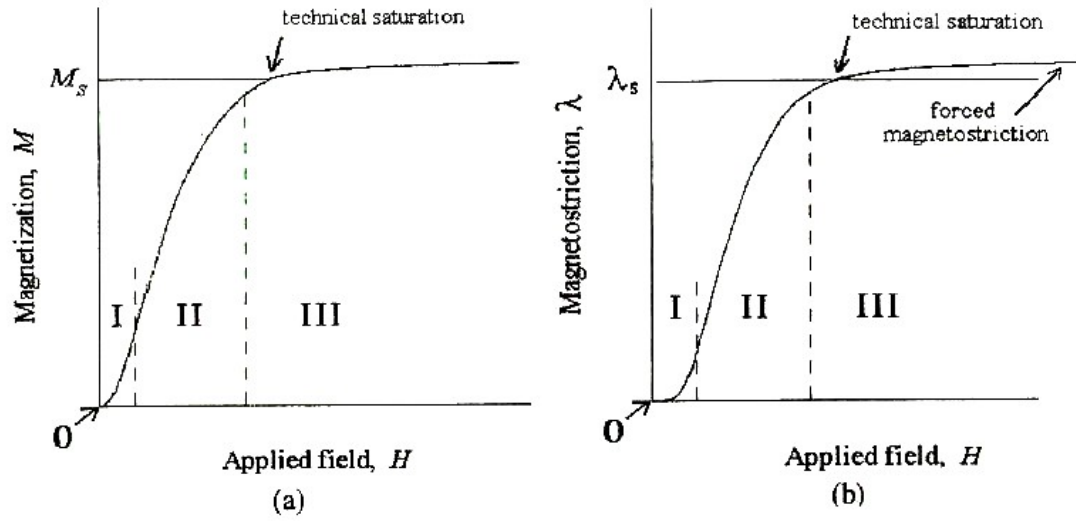


Figure 2.5: Simulation of initial (a) magnetization and (b) magnetostriction with applied field [8, 19].

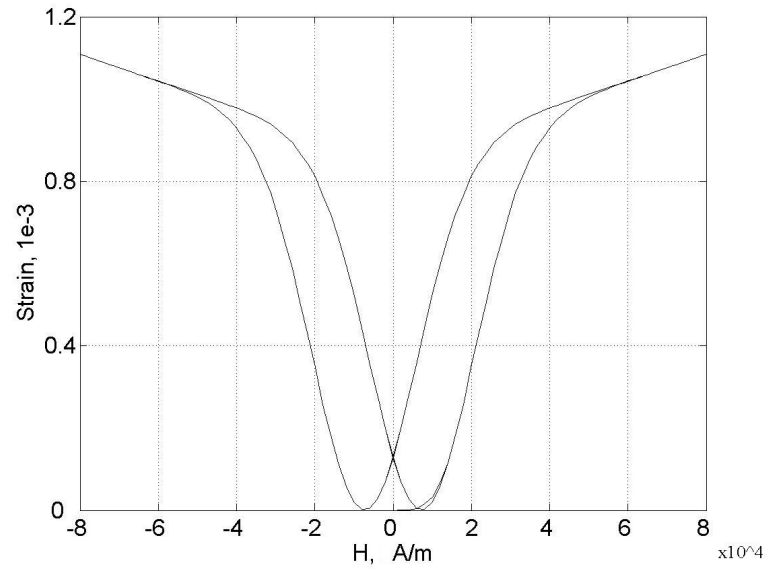


Figure 2.6: Simulated strain versus magnetic field for Terfenol-D.

response for low to moderate applied field levels. These relations build on the superposition of elastic, magnetic, and thermal effects on the strain and magnetic induction.

In differential form they are

$$\begin{aligned} d\varepsilon &= \left(\frac{\partial \varepsilon}{\partial \sigma} \right)_{H,T} d\sigma + \left(\frac{\partial \varepsilon}{\partial H} \right)_{\sigma,T} dH + \left(\frac{\partial \varepsilon}{\partial T} \right)_{H,\sigma} dT \\ dB &= \left(\frac{\partial B}{\partial \sigma} \right)_{H,T} d\sigma + \left(\frac{\partial B}{\partial H} \right)_{\sigma,T} dH + \left(\frac{\partial B}{\partial T} \right)_{H,\sigma} dT, \end{aligned}$$

where ε is the strain, B is the induction, H is the applied field, T is the absolute temperature, and σ is the axial stress [8, 19]. Neglecting the effects of temperature, and expressing the partial derivatives as real coefficients gives

$$\varepsilon = \frac{\sigma}{E_y^H} + q_{33}H \quad (2.4)$$

$$B = q_{33}^*\sigma + \mu^\sigma H, \quad (2.5)$$

where E_y^H is the Young's modulus at constant field, μ^σ is the permeability at constant stress, and q_{33} and q_{33}^* are the magnetoelastic coupling coefficients. The analogy between these equations and the piezoelectric constitutive relations (2.1)-(2.2) is emphasized. This model is compatible with some fundamental principles, such as the strain being the superposition of Hooke's law $\sigma = \varepsilon E_y$ and a representation of the magnetostriction λ by the term $q_{33}H$. In addition, the induction B is seen to be a combination of the constitutive magnetic law $B = \mu H$ and a mechanically coupled term $q_{33}^*\sigma$, where it is often assumed that $q_{33} = q_{33}^*$. This model will be used later in this chapter to generate a full linear description of the transducer, while Chapter 3 will expand on this by more accurately accounting for the various physical effects that are either linearized or ignored in (2.4)-(2.5).

2.1.7 Terfenol-D Transducers

To take full advantage of the unique properties and energy transduction characteristics of Terfenol-D, this material must be placed in a transducer. Numerous applications exist where a magnetomechanical system could be of use, but for purposes of this investigation the primary interest is in a broadband sonar transducer. In this device the Terfenol-D element represents a key component of both the mechanical and electrical regimes.

Mechanically, the Terfenol-D rod has three fundamental functions in the transducer: representing the compliance, adding damping, and generating force excitation internal to the transducer. The rod is placed between two masses and acts as a spring with a stiffness parameter k defined by

$$k = \frac{E_y^H A}{L_e}, \quad (2.6)$$

where A is the cross-sectional area and L_e is the length. The masses in this structure are designed around the Terfenol-D stiffness to result in a specific angular natural frequency of oscillation ω_n (rad/s). The damping coefficient is not as easily defined but it should be apparent that the hysteresis and irreversibility in the magnetostriction process will result in a loss of energy that appears as mechanical dissipation. The final role that the material plays in the mechanical system is that of an excitation source to generate the desired oscillations of the structure. The magnetostrictive strain will generate a drive force applied from the rod onto each of the attached masses and the PMN-PT stack. By controlling the applied magnetic field, and thus the magnetostriction, a variety of forcing inputs can be applied to the transducer.

In order to drive the Terfenol-D with a magnetic field, a solenoid is used. By having a solenoid wrapped around the cylindrical rod, the magnetic field through the rod will be uniaxial and relatively uniform, as first shown in Figure 1.7. Coupling this setup to the overall electromechanical system is the fact that the solenoid wrapped around the metal rod is electrically an ideal inductor in series with a small resistor. The inductance for this geometry has been already derived in equation (1.18), with μ being the permeability of the Terfenol-D core.

Another major component in the Terfenol-D transducer is often a permanent magnet that serves two functions. First, it partially completes the necessary magnetic circuit through which the magnetic flux passes. Second, it provides a permanent field that can magnetically bias the material to a nominal operating point. Like in PMN-PT, this is often necessary when sinusoidal motions are needed from the device. Looking at Figure 2.5, the linear constitutive model (2.4)-(2.5) provides sufficient accuracy if the applied field from the solenoid can be kept on the steepest region of the curve. Shifting the effective field to this region is accomplished in part by a permanent magnet and partly from a DC current in the solenoid. The field lines for a cylindrical permanent magnet are shown in Figure 2.7. As a final consideration, Terfenol-D requires a compressive prestress for the reasons discussed above, which is applied through the use of Belleville spring washers and adjustable compression bolts. Figure 2.8 details the general geometry and key components in a typical Terfenol-D transducer.

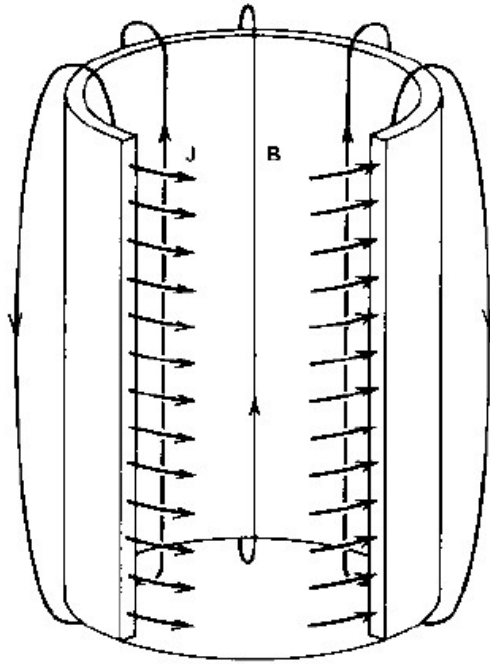


Figure 2.7: Magnetic field lines from a cylindrical permanent magnet like that encasing the Terfenol-D rod [23].

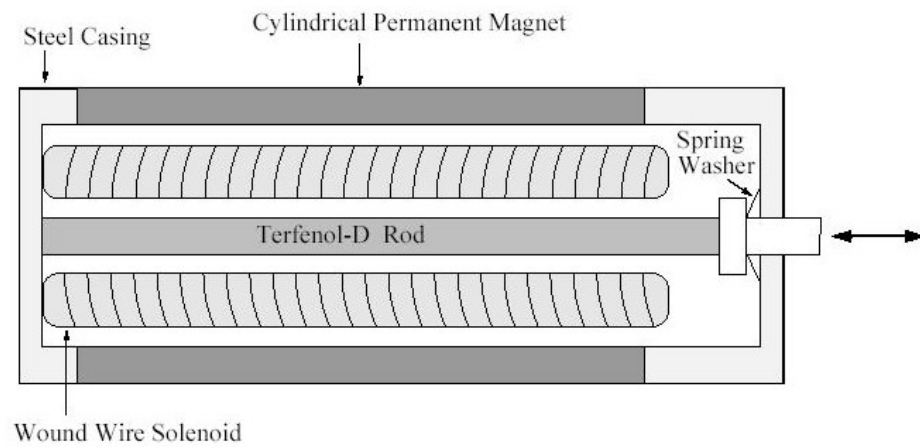


Figure 2.8: Overview of a typical Terfenol-D transducer [6].

2.2 Linear System Dynamics Model

The broadband transducer under investigation has the Tonpilz sonar configuration shown in Figure 2.9 with the piezoelectric and magnetostrictive elements each located between two oscillating masses [1, 2]. Rigidly combining these two sections in mechanical series forms a double resonant system in which the lower resonance is controlled by the Terfenol-D element and the higher resonance by the PMN-PT stack. The inductive drive solenoid for the Terfenol-D rod is wired in parallel with the capacitive PMN-PT stack to create an electrical resonant system as shown in Figure 2.10. The hybrid properties that facilitate broadband operation include an inherent 90° phase shift in the velocities of the two sections and a natural difference in the speed of sound in the active materials [3].

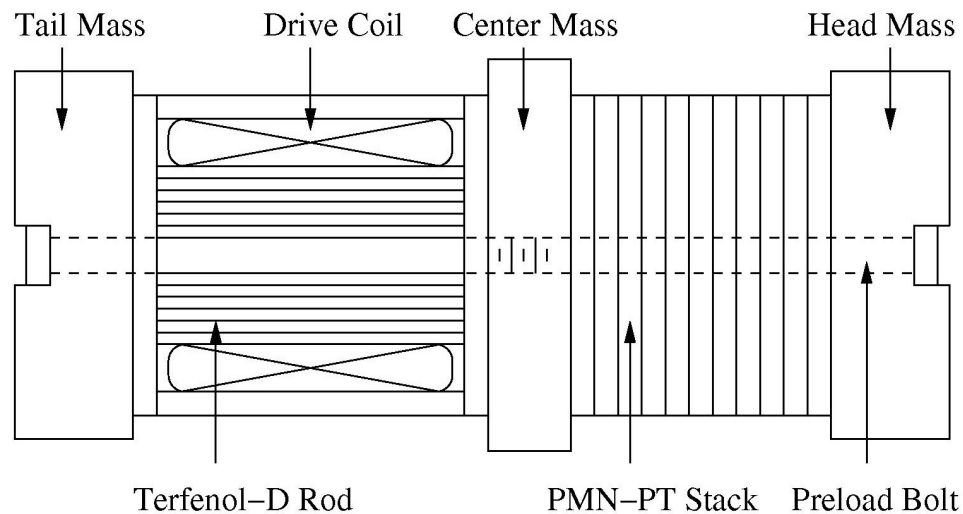


Figure 2.9: Schematic of a Tonpilz broadband hybrid transducer.

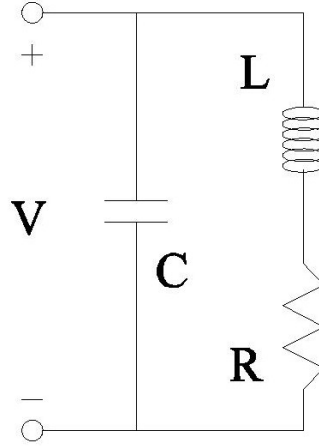


Figure 2.10: Corresponding electrical circuit with the two active sections wired in parallel.

A linear system model describing the dynamic behavior of the transducer is developed in three steps. This model incorporates concepts from vibrations, electronics, acoustics, and smart materials to characterize the complete system response as well as the interactions between the electrical and mechanical domains. In the first modeling stage, a linear vibrations framework is used to represent the mechanical regime of the transducer. The second model component utilizes electroacoustics theory to describe the coupling between the mechanical and electrical regimes and to identify pertinent physical system parameters. The third step involves the development of relations between stress, strain, and applied field, as well as the characterization of material properties. The resulting set of linearized equations is used to quantify the dependence of material properties with drive and acoustic load conditions, as well as develop the transducer frequency response functions velocity per voltage and voltage per current.

2.2.1 Mechanical Model

The transducer architecture employed here consists of a mechanical series arrangement of piezoelectric and magnetostrictive sections joined through a rigid center mass, with oscillating head and tail masses at opposite ends. This configuration provides a double resonant frequency response which is used to facilitate broad frequency bandwidth operation. For modeling purposes, each smart material is assumed to behave mechanically as a tunable compliance arranged in parallel with a damper as described by the three degree of freedom linear vibratory system shown in Figure 2.11.

This mechanical model is analyzed to determine the ideal mass and stiffness ratios to achieve the largest bandwidth possible over the 1-6 kHz frequency range, which has been determined by the U.S. Navy to be of primary interest in hybrid architectures [3]. To start, the equation of motion for each mass is written and the three equations

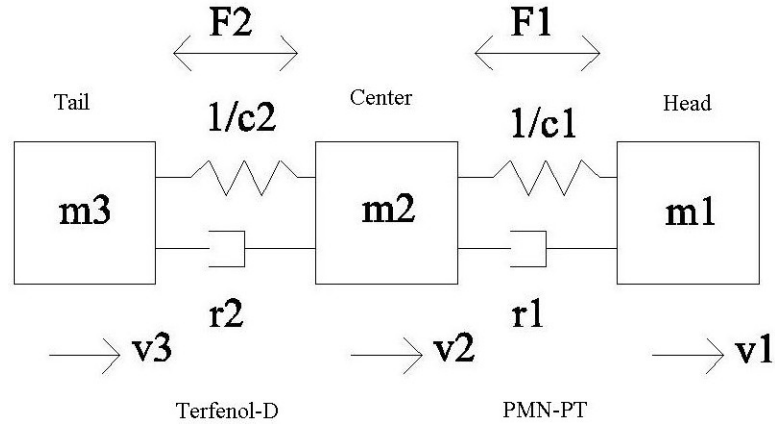


Figure 2.11: Transducer modeled as a 3 degree-of-freedom mechanical vibratory system.

are then related in matrix form as

$$[M]\ddot{\vec{x}} + [C]\dot{\vec{x}} + [K]\vec{x} = \vec{F}, \quad (2.7)$$

in which the structural matrices and vectors are

$$\begin{aligned} [M] &= \begin{bmatrix} m_1 & 0 & 0 \\ 0 & m_2 & 0 \\ 0 & 0 & m_3 \end{bmatrix} \\ [C] &= \begin{bmatrix} r_1 & -r_1 & 0 \\ -r_1 & r_1 + r_2 & -r_2 \\ 0 & -r_2 & r_2 \end{bmatrix} \\ [K] &= \begin{bmatrix} \frac{1}{c_1} & -\frac{1}{c_1} & 0 \\ -\frac{1}{c_1} & \frac{1}{c_1} + \frac{1}{c_2} & -\frac{1}{c_2} \\ 0 & -\frac{1}{c_2} & \frac{1}{c_2} \end{bmatrix} \\ \vec{x} &= \begin{bmatrix} x_1 \\ x_2 \\ x_3 \end{bmatrix} \\ \vec{F} &= \begin{bmatrix} F_1 \\ F_2 - F_1 \\ -F_2 \end{bmatrix}, \end{aligned}$$

where m represents the mass, r the damping, c the mechanical compliance, x the displacement, F the force, and subscripts 1, 2, and 3, respectively denote the head, center, and tail masses, as in Figure 2.11. Consistent with prior work [3], it is determined that optimum bandwidth is achieved using a head : center : tail mass ratio of approximately 1 : 2 : 2.5, and having the piezoceramic stack ($1/c_1$) be much stiffer than the Terfenol-D rod ($1/c_2$). Using these values in eigenvector modal analysis, the mode shapes and natural frequencies are found to be approximately

$$\vec{u}_1 = \begin{bmatrix} .58 \\ .58 \\ .58 \end{bmatrix} = \begin{bmatrix} 1 \\ 1 \\ 1 \end{bmatrix} \quad \vec{u}_2 = \begin{bmatrix} -.58 \\ -.50 \\ .64 \end{bmatrix} \approx \begin{bmatrix} -1 \\ -1 \\ 1 \end{bmatrix} \quad \vec{u}_3 = \begin{bmatrix} .90 \\ -.44 \\ -.03 \end{bmatrix} \approx \begin{bmatrix} 2 \\ -1 \\ 0 \end{bmatrix}$$

$$\omega_{n1} = 0 \text{ Hz}$$

$$\omega_{n2} = 1250 \text{ Hz}$$

$$\omega_{n3} = 4000 \text{ Hz}$$

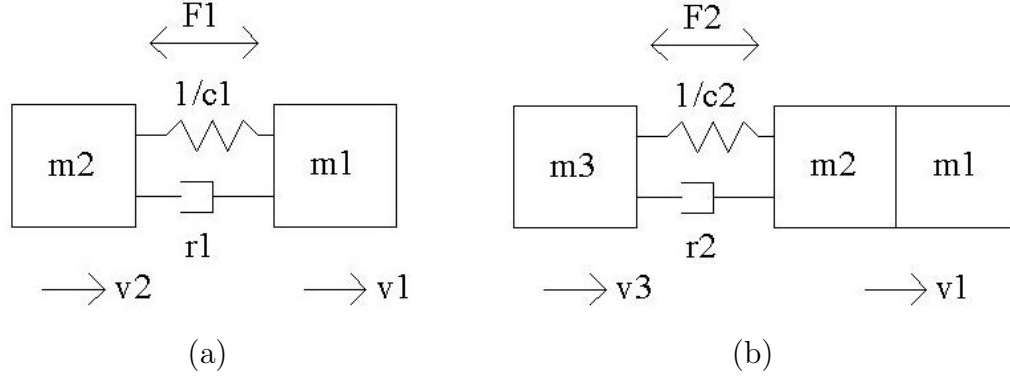


Figure 2.12: Mechanical representation of the simplified (a) high frequency (PMN-PT) and (b) low frequency (Terfenol-D) vibration modes.

where the zero frequency rigid body translational mode is ignored. The two other modes dominate the motion of the system, where the lower resonance is controlled by the Terfenol-D section and is characterized by the head and center masses lumped together vibrating out of phase with the tail mass. The PMN-PT stack controls the upper resonance where the tail mass essentially decouples from the system and the head and center masses are out of phase with each other. Both of these situations are depicted in Figure 2.12 and are described by the equations

$$\begin{aligned} m_1 \ddot{x}_1 + r_1 \dot{x}_1 + \frac{1}{c_1} x_1 &= F_1 + r_1 \dot{x}_2 + \frac{1}{c_1} x_2 \\ m_2 \ddot{x}_2 + r_1 \dot{x}_2 + \frac{1}{c_1} x_2 &= -F_1 + r_1 \dot{x}_1 + \frac{1}{c_1} x_1 \end{aligned}$$

for the high frequency mode and

$$\begin{aligned} (m_1 + m_2) \ddot{x}_1 + r_2 \dot{x}_1 + \frac{1}{c_2} x_1 &= F_2 + r_2 \dot{x}_3 + \frac{1}{c_2} x_3 \\ m_3 \ddot{x}_3 + r_2 \dot{x}_3 + \frac{1}{c_2} x_3 &= -F_2 + r_2 \dot{x}_1 + \frac{1}{c_2} x_1 \end{aligned}$$

for the low frequency mode, all of which are simplifications of equation (2.7) using the known mode shapes. Converting to the frequency domain and rewriting in terms of the velocities yields

$$m_1 s v_1 + r_1 v_1 + \frac{1}{s c_1} v_1 = F_1 + r_1 v_2 + \frac{1}{s c_1} v_2 \quad (2.8)$$

$$m_2 s v_2 + r_1 v_2 + \frac{1}{s c_1} v_2 = -F_1 + r_1 v_1 + \frac{1}{s c_1} v_1 \quad (2.9)$$

for the high frequency mode and

$$(m_1 + m_2) s v_1 + r_2 v_1 + \frac{1}{s c_2} v_1 = F_2 + r_2 v_3 + \frac{1}{s c_2} v_3 \quad (2.10)$$

$$m_3 s v_3 + r_2 v_3 + \frac{1}{s c_2} v_3 = -F_2 + r_2 v_1 + \frac{1}{s c_2} v_1 \quad (2.11)$$

for the low frequency mode. When the transducer is excited in a broadband fashion the two modes' resonant peaks will overlap in the frequency domain to create a wide, relatively flat region in the head mass velocity response v_1 , a key criterion for propagating acoustic energy into a medium. Equations (2.8)-(2.11) are used to simulate the bandwidth of the two individual modes and the combined system as shown in Figure 2.13.

The idealization of the vibration modes results in each section inaccurately ignoring the dynamic effects of the other section. In reality, broadband excitation of one section will cause some response in the other which will alter the separate head mass responses of Figure 2.13. To account for such dynamics, the simplified modes are ignored and the full system (2.7) is transformed into the frequency domain and expressed in terms of velocities as follows,

$$m_1 s v_1 + r_1 v_1 + \frac{1}{s c_1} v_1 = F_1 + r_1 v_2 + \frac{1}{s c_1} v_2 \quad (2.12)$$

$$m_2 s v_2 + (r_1 + r_2) v_2 + \left(\frac{1}{s c_1} + \frac{1}{s c_2} \right) v_2 = F_2 - F_1 + r_1 v_1 + r_2 v_3 + \frac{1}{s c_1} v_1 + \frac{1}{s c_2} v_3 \quad (2.13)$$

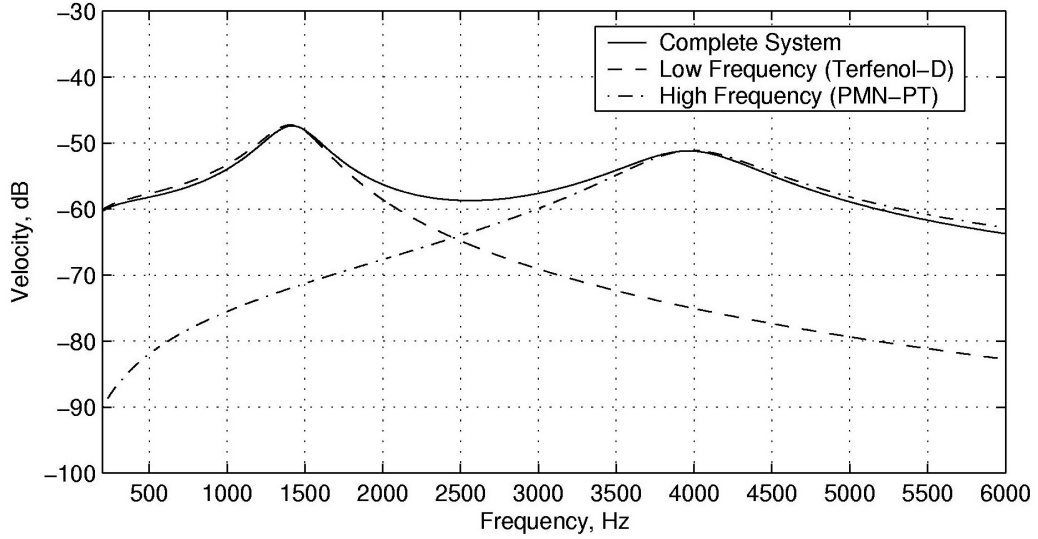


Figure 2.13: Head mass velocity response of the complete system and individual sections calculated from the ideal mode linear mechanical model (2.8)-(2.11).

$$m_3 s v_3 + r_2 v_3 + \frac{1}{s c_2} v_3 = -F_2 + r_2 v_2 + \frac{1}{s c_2} v_2. \quad (2.14)$$

Since v_1 is the primary term of interest, the algebraic system of equations (2.12)-(2.14) is solved for v_1 as a function of the forcing functions F_1 and F_2 . As a means to fully describe the mechanical regime of the transducer, the transfer function force per velocity, i.e. the mechanical impedance, can be found for each smart material section. For the PMN-PT element, the force F_2 from the Terfenol-D rod is set to zero and then F_1/v_1 is shown to be

$$Z_{mech,E} = \frac{A s^4 + B s^2 + C}{s c_1 (m_2 m_3 c_2 s^2 + (m_2 + m_3)(r_2 c_2 s + 1))}, \quad (2.15)$$

while for the Terfenol-D rod, F_1 is set to zero and F_2/v_1 gives

$$Z_{mech,M} = \frac{A s^4 + B s^2 + C}{s c_2 m_3 (r_1 c_1 s + 1)}. \quad (2.16)$$

The subscripts E and M denote electric and magnetic for the PMN-PT and Terfenol-D elements, respectively. In equations (2.15)-(2.16), the terms A , B , and C are of the form

$$\begin{aligned} A &= (m_1 m_2 m_3 c_1 c_2) \\ B &= m_3(m_1 + m_2)c_2(r_1 c_1 s + 1) + m_1(m_2 + m_3)c_1(r_2 c_2 s + 1) \\ C &= (r_1 c_1 s + 1)(r_2 c_2 s + 1)(m_1 + m_2 + m_3). \end{aligned}$$

Relations (2.15)-(2.16) characterize the output response of the transducer due to activation of either smart material. For later comparison, the mechanical impedances for the two idealized modes are found in an identical manner from (2.8)-(2.11) to be

$$Z_{m,E} = \frac{m_1 m_2 c_1 s^2 + (r_1 c_1 s + 1)(m_1 + m_2)}{m_2 c_1 s} \quad (2.17)$$

for the PMN-PT stack and

$$Z_{m,M} = \frac{(m_1 + m_2)m_3 c_2 s^2 + (r_2 c_2 s + 1)(m_1 + m_2 + m_3)}{m_3 c_2 s}. \quad (2.18)$$

for the Terfenol-D rod.

2.2.2 Electroacoustics Model

For the second modeling step, classical eletroacoustic transduction theory [15] is considered for purposes of coupling the vibratory model with the electrical regime. The field of electroacoustics is based on the validated observations that a functional relationship exists between the variables describing two different energy regimes. Considering a typical “black box” transducer that couples arbitrary electrical and mechanical systems, such as that depicted in Figure 2.14, two coupled equations can be written that describe the system, one for the electrical side and one for the mechanical side. For operating regimes in which linear models are accurate, the frequency

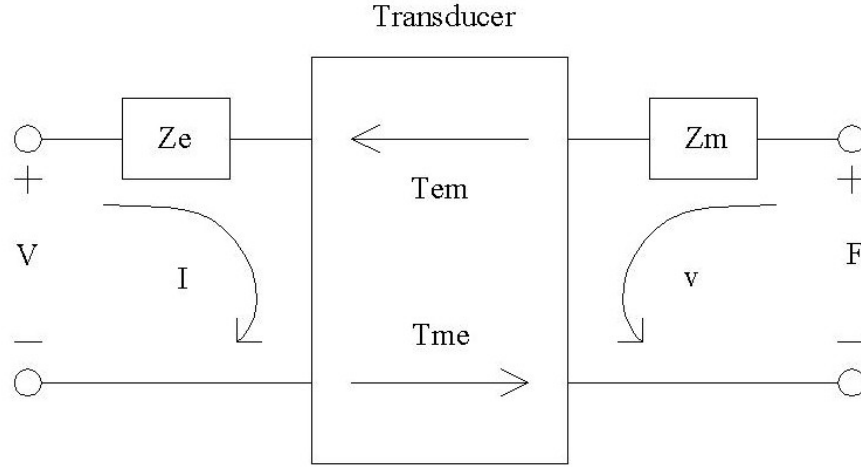


Figure 2.14: General representation of an electromechanical transducer.

domain relations that quantify this coupling between the electrical and mechanical regimes are

$$V = Z_e I + T_{em} v \quad (2.19)$$

$$F = T_{me} I + Z_m v, \quad (2.20)$$

where V is the voltage across the transducer terminals, I is the current flow through the transducer, v is the velocity, F is the force, Z_e and Z_m are the blocked electrical and mechanical impedances, respectively, and T_{em} and T_{me} are transduction coefficients that describe the electromechanical coupling of the system. The subscript em reads as “electrical due to mechanical”, and vice versa. Simplifying the model to have no electromechanical coupling ($T_{em} = T_{me} = 0$), equations (2.19)-(2.20) reduce to the basic definition of blocked impedance for each energy regime.

Fundamental properties of the electromechanical interaction can be studied by considering the driving-point impedance at either the electrical or mechanical terminals as fully detailed by Hunt [15]. Due to the easily measurable nature of electric variables, the electrical impedance is preferred for use in this investigation. The driving-point impedance is defined as the complex ratio of voltage to current, but with the added restriction that all other energy sources are suppressed. For a general system described by the electroacoustic equations (2.19)-(2.20), it is assumed that the force F acts on a load of impedance Z_L , which allows (2.20) to be rewritten in the form

$$v = \frac{-T_{me}I}{Z_m + Z_L}, \quad (2.21)$$

which upon substitution in (2.19) gives the total electrical impedance,

$$Z_{ee} = \frac{V}{I} = Z_e + \frac{-T_{em}T_{me}}{Z_m + Z_L} = Z_e + Z_{mot}. \quad (2.22)$$

This impedance is the superposition of the blocked electrical impedance Z_e and the coupled effects of the mechanical motion Z_{mot} , known as the motional impedance. Figure 2.15 illustrates how the mechanical contributions affect the electrical impedance of a capacitive PMN-PT stack. The solid line shows the blocked impedance Z_e and the deviation from this line represents the coupled motional effects Z_{mot} .

2.2.3 Electrical Impedance Analysis

The key to using the total electrical impedance Z_{ee} in analyzing the transducer is to plot it on the complex plane as imaginary part versus real part (Nyquist format). The impedance is frequency dependent due to the presence of s , and thus as the frequency is changed the tip of the impedance vector will trace out the curve known

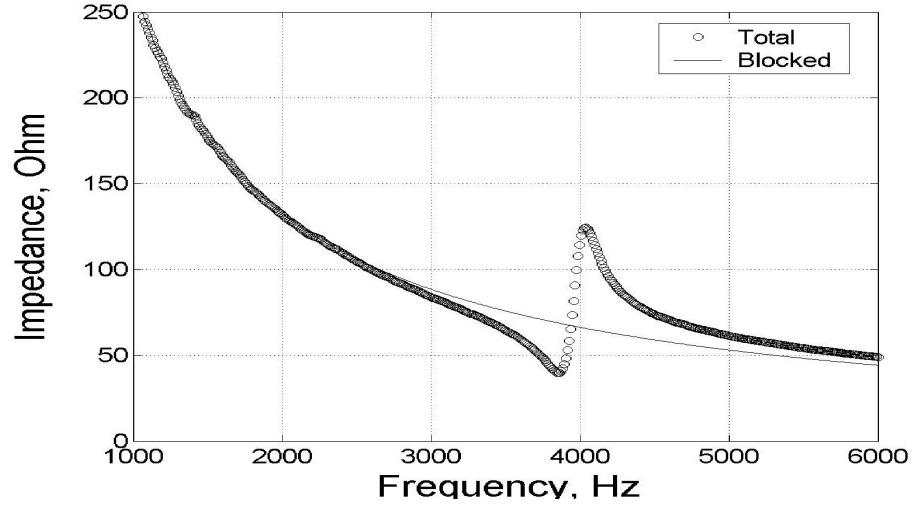


Figure 2.15: Experimental total and blocked electrical impedance magnitude of the PMN-PT section employed in this investigation.

as a locus. For a typical transducer mechanism this locus will have the form of Figure 2.16, also collected from the PMN-PT stack employed in this investigation. The circular shape is called the mobility loop caused by the mechanical coupling, since as frequency increases the locus will divert from the blocked path and circle clockwise.

The value of this approach lies in that the frequency directly opposite the crossover point on the mobility loop is the transducer's resonance frequency $f_r = \omega_n/2\pi$. Note that this frequency does not correspond to the relative maximum seen on Figure 2.15 because that graph does not contain phase information. The two points on the circle at 90° from the main diameter are the half power points f_1 and f_2 .

An identical form of analysis is performed on the electrical admittance function, defined as the inverse of the impedance, $Y_{ee} = 1/Z_{ee}$. This relation will likewise have a corresponding locus such as that shown in Figure 2.17. The inverse relationship

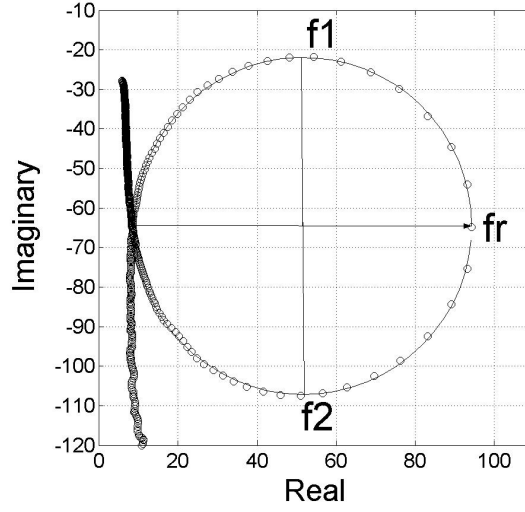


Figure 2.16: Experimental impedance mobility loop associated with the data in Figure 2.15, showing resonance (f_r) and half power point (f_1, f_2) frequencies.

between impedance and admittance means that this curve is simply a geometric inversion of the impedance locus with respect to unity. This does not mean, however, that identical information is present in both. Although the total impedance and admittance are inverses of one another, the coupled motional effects are not, i.e. $Y_{mot} \neq 1/Z_{mot}$. In fact, one important difference is that in the admittance loop the frequency opposite the crossover point is a measure of the antiresonance frequency f_{ar} . Similarly, the points at 90° from this are the half power points associated with antiresonance, f_{a1} and f_{a2} .

The resonant and antiresonant frequencies are combined in a relation for the effective coupling between the mechanical and electrical regimes,

$$k_{eff}^2 = 1 - \left(\frac{f_{ar}}{f_r} \right)^2, \quad \text{if } f_{ar} < f_r \quad (2.23)$$

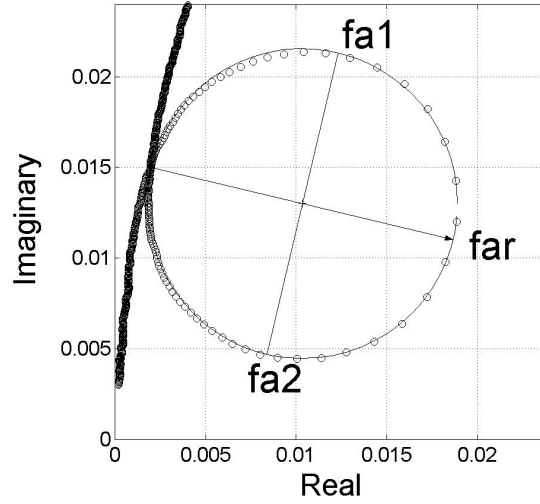


Figure 2.17: Experimental admittance mobility loop associated with the data in Figure 2.15, showing antiresonance (f_{ar}) and half power point (f_{a1}, f_{a2}) frequencies.

$$k_{eff}^2 = 1 - \left(\frac{f_r}{f_{ar}} \right)^2, \quad \text{if } f_{ar} > f_r \quad (2.24)$$

depending upon whether f_{ar} or f_r is smaller, respectively. This is required to keep the coupling less than or equal to one, and will be shown to be dependent upon the type of smart material and the variables in the electric circuit.

The resonant frequencies are also important in the determination of a variety of material properties. In conjunction with the known masses, they offer a means of calculating the stiffness of each smart material element. From the simplified expressions of mechanical impedance, equations (2.17)-(2.18), the stiffness is determined by setting the imaginary component equal to zero and rearranging, that is

$$k_m^E = \frac{1}{c_1} = \frac{(2\pi f_r)^2 m_1 m_2}{m_1 + m_2} \quad (2.25)$$

$$k_m^H = \frac{1}{c_2} = \frac{(2\pi f_r)^2(m_1 + m_2)m_3}{m_1 + m_2 + m_3} \quad (2.26)$$

respectively for the PMN-PT stack and Terfenol-D rod. The values obtained from the full impedances (2.15)-(2.16) are mathematically more complex but numerically equal. Assuming that the material follows linear elastic behavior the Young's moduli take the form of (2.3) and (2.6),

$$E_y^E = \frac{k_m^E L_{e,1}}{A_1} \quad (2.27)$$

$$E_y^H = \frac{k_m^H L_{e,2}}{A_2}, \quad (2.28)$$

and from them each material's intrinsic sound speed is

$$c_E = \sqrt{\frac{E_y^E}{\rho_E}}$$

$$c_M = \sqrt{\frac{E_y^H}{\rho_M}}$$

where ρ is the material density.

Another property that can be found from this analysis is the mechanical quality factor Q of each section, which from equation (1.30) is an approximate measure of the amount of damping present in the system,

$$Q_r = \frac{f_r}{f_2 - f_1}$$

$$Q_{ar} = \frac{f_{ar}}{f_{a2} - f_{a1}}.$$

Both active sections will have two Q values, one from each set of frequencies, with f_1 and f_2 being the half power points associated with f_r , and f_{a1} and f_{a2} those corresponding to f_{ar} . In this study, the average value of these two Q 's is used. Analysis of the mechanical equations of motion shows that the internal damping can

be respectively estimated as

$$r_1 = \frac{2\pi f_r m_1 m_2}{Q(m_1 + m_2)} \quad (2.29)$$

$$r_2 = \frac{2\pi f_r (m_1 + m_2) m_3}{Q(m_1 + m_2 + m_3)} \quad (2.30)$$

for the PMN-PT and Terfenol-D sections. This procedure of calculating material parameters is applied to actual test data collected from the physical transducer and the results obtained are used as nominal values in the model simulations.

2.2.4 Electroacoustics Model for the Terfenol-D Section

The linear electroacoustic relations and corresponding impedance analysis provide a framework which is sufficiently general to analyze a variety of electromechanical systems. However, for purposes of modeling hybrid smart structures, additional physical details must be considered, especially concerning the active coupling effects inherent to the two smart materials. To this end, the linearized constitutive relations for the active materials will be converted into a form comparable with equations (2.19)-(2.20), thus allowing for the blocked impedances and transduction coefficients to be expressed in terms of properties such as coupling, Young's moduli, magnetic or electric parameters, and physical dimensions. While the material behaviors are in actuality nonlinear and hysteretic, linearized models are sufficiently accurate for biased, low signal operation in which saturation and frequency-doubling effects are reduced.

For a system featuring magnetostrictive transduction, various electroacoustic coefficients can be determined by comparing the constitutive relations (2.4)-(2.5), rewritten here for convenience

$$\begin{aligned}\varepsilon &= \frac{\sigma}{E_y^H} + q_{33}H \\ B &= q_{33}\sigma + \mu^\sigma H,\end{aligned}$$

with the transduction equations (2.19)-(2.20) [12]. Assuming that the Terfenol-D rod is placed inside and completely fills an ideal wire solenoid, then the magnetic field H and current I are related through $H = nI$. The solenoid flux linkage is $N\phi$, where ϕ is given by equation (1.8) as BA . The voltage potential across the solenoid is that of a DC resistance times the current plus the time rate of change of the total flux linkage. Assuming spatial independence of stress and strain, the strain is related to the displacement x by definition $\varepsilon = x/L_e$, which can then be expressed as a velocity via a time derivative. Finally, the axial stress in the rod can be compared with the internal force by ratio of cross-sectional area. These electromechanical relations are summarized as

$$\begin{aligned}H &= nI \\ \varepsilon &= \frac{v}{j\omega L_{e,2}} \\ \sigma &= \frac{F}{A_2} \\ V &= RI + j\omega NA_2B,\end{aligned}$$

with all of the variables previously defined. Substitution of these expressions into (2.19)-(2.20) yields

$$V = (R + j\omega\mu^\sigma(1 - k^2)n^2A_2L_{e,2}) I + Nqk_m^H v \quad (2.31)$$

$$F = -Nqk_m^H I + \frac{k_m^H}{j\omega} v, \quad (2.32)$$

where $q = q_{33}$ and k^2 is the magnetomechanical coupling factor defined as

$$k^2 = \frac{q^2 E_y^H}{\mu^\sigma}. \quad (2.33)$$

By comparison with the electroacoustic equations it is evident that the blocked electrical impedance $Z_{e,M}$ for the Terfenol-D section is an ideal resistor in series with an inductor with the inductance L expressed in terms of material properties,

$$Z_{e,M} = R + j\omega\mu^\sigma(1 - k^2)n^2 A_2 L_{e,2} = R + j\omega L_{block}. \quad (2.34)$$

The inductance value for this solenoid geometry was independently derived in equation (1.18) and is found to be equivalent when the fixed (constant strain) permeability is redefined as the permeability at constant stress times the coupling factor, $\mu^\varepsilon = \mu^\sigma(1 - k^2)$ [12].

Equations (2.31)-(2.32) also present the form of the transduction coefficients T_{em} and T_{me} . These terms describe the coupling between the electrical and mechanical regimes and have the form

$$T_{em,M} = Nqk_m^H \quad (2.35)$$

$$T_{me,M} = -Nqk_m^H = -T_{em,M}. \quad (2.36)$$

It is noted that they are equal in magnitude while opposite in sign. This antisymmetric relationship, according to Hunt [15], is expected of all magnetostrictive transducers because of the spatial orthogonality of current and magnetic field.

The final electroacoustic coefficient is the blocked mechanical impedance $Z_{m,M}$. By the manipulations done above the resultant term appears as $Z_{m,M} = k_m^H/j\omega$, which

contains only a stiffness term. Other dynamic effects such as inertia and damping are tacitly ignored in the constitutive material relations [12], hence these relations predict a very inaccurate mechanical impedance. Note, however, that the mechanical part of the model has already led to a complete formulation of $Z_{m,M}$ in equation (2.16), hence the stiffness calculated from the constitutive material relations is completely disregarded and replaced by the detailed term derived previously.

With all of the frequency domain coefficients in the electroacoustics framework written in terms of measurable or calculable properties it is necessary to combine these expressions into a complete description of the Terfenol-D section. The total electrical impedance function (2.22) offers a single expression that includes all relevant electrical, magnetic, and mechanical effects. Thus the magnetostrictive section can be described by

$$Z_{ee,M} = Z_{e,M} + \frac{-T_{em,M}T_{me,M}}{Z_{m,M}}, \quad (2.37)$$

where the blocked electrical impedance is given by (2.34), the transduction coefficients are given by (2.35)-(2.36), and the mechanical impedance is expressed by (2.16).

2.2.5 Electroacoustics Model for the PMN-PT Section

In this section, relations analogous to those developed in Section 2.2.4 are developed for the PMN-PT stack. Beginning with the constitutive piezoelectric relations (2.1)-(2.2), which are rewritten here for convenience with $d = d_{33}$,

$$\begin{aligned} \varepsilon &= \frac{\sigma}{E_y} + dE \\ D &= d\sigma + \epsilon_0 E \end{aligned}$$

several electromechanical conversions are performed to relate these to the electroacoustics framework. For each individual layer in the stack, the voltage is applied

across the thickness t of the material, implying that the electric field E is simply equal to V/t . The electric displacement (flux density) D is defined as charge per area and is then converted into current through $q = I/j\omega$. As before, assuming uniform stress and strain allows for fundamental relationships between stress and force, and strain and velocity. These expressions combined explicitly are

$$\begin{aligned} E &= \frac{V}{t} \\ \varepsilon &= \frac{v}{j\omega t} \\ \sigma &= \frac{F}{A_1} \\ D &= \frac{I}{j\omega A_1}. \end{aligned}$$

Substituting the above into (2.19)-(2.20) gives, for N layers,

$$V = \frac{t}{A_1 j\omega N(\epsilon_0 - E_y^E d^2)} I + \frac{-dE_y^E}{j\omega N(\epsilon_0 - E_y^E d^2)} v \quad (2.38)$$

$$F = \frac{-dE_y^E}{j\omega N(\epsilon_0 - E_y^E d^2)} I + \frac{\epsilon_0 E_y^E A_1}{j\omega N(\epsilon_0 - E_y^E d^2)} v, \quad (2.39)$$

which are in standard electroacoustic form.

From these equations, it is inferred that the blocked electrical impedance of the PMN-PT stack is purely capacitive,

$$Z_{e,E} = \frac{t}{j\omega A_1 N(\epsilon_0 - E_y^E d^2)} = \frac{1}{j\omega C_{block}}. \quad (2.40)$$

The specific formulation of C_{block} is not unexpectedly analogous to the previously derived capacitance of two parallel plates in (1.16), with the permittivity constant now incorporating some additional terms.

Additionally, the two transduction coefficients which characterize the electromechanical interaction can be written from equations (2.38)-(2.39) as

$$T_{em,E} = \frac{-dE_y^E}{j\omega N(\epsilon_0 - E_y^E d^2)} \quad (2.41)$$

$$T_{me,E} = \frac{-dE_y^E}{j\omega N(\epsilon_0 - E_y^E d^2)} = T_{em,E}. \quad (2.42)$$

In contrast with the Terfenol-D section, these coefficients are symmetric, that is they are identical in both magnitude and sign. This symmetry is consistent with the electrical nature of the transduction. It was mentioned previously that the velocities of the two sections are inherently 90° out of phase and that this property is useful in extending bandwidth. This phase shift can be proven by comparing the T_{em} electrical to mechanical transduction coefficient of each section,

$$\angle \left(\frac{T_{em}^E}{T_{em}^M} \right) = \angle \left(\frac{-T_1}{j\omega T_2} \right) = 90^\circ.$$

This transduction coefficient relates voltage to velocity in the electroacoustics framework. When the two sections are wired in parallel and receive the same applied voltage, the phase of the velocities will be determined by the T_{em} 's and thus will always be 90° apart even when moving through resonance.

Just as for the Terfenol-D, the resultant mechanical impedance of this comparison is solely a compliance term, proven by the $1/j\omega$ dependence in the velocity term of equation (2.39). Due to the lack of the constitutive piezoelectric equations to properly account for dynamic effects, the expression for the mechanical impedance derived above is replaced with the more complete $Z_{m,E}$ given by equation (2.15).

Analogous to the Terfenol-D section is the choice of the total electrical impedance Z_{ee} to characterize the multi-regime effects of the PMN-PT stack. This expression

once again is

$$Z_{ee,E} = Z_{e,E} + \frac{-T_{em,E}T_{me,E}}{Z_{m,E}}, \quad (2.43)$$

with the electroacoustic coefficients defined in (2.40)-(2.42) and (2.15).

2.2.6 Combined Linear Transducer Model

With relations for the mechanical, electroacoustic, and material regimes of each smart material section, it is necessary to combine all aspects of the model into an overall description of the transducer. When the two active sections are physically combined, they are joined mechanically in series and electrically in parallel in agreement with previous work. Since the smart materials are wired in electrical parallel, their total electrical impedances including motional contributions sum as normal. Thus the complete hybrid system's overall impedance, incorporating both elements' different electrical and mechanical effects, is

$$Z_{ee,total} = \frac{Z_{ee,E} Z_{ee,M}}{Z_{ee,E} + Z_{ee,M}}. \quad (2.44)$$

2.2.7 Determination of Model Parameters

The next step consists of determining the material parameters used in expressions (2.37) and (2.43). The impedance and admittance analysis outlined in Section 2.2.3 is used to produce the resonance, antiresonance, and half power frequencies for each section. From these it is shown how the material stiffnesses and elastic moduli are found for substitution into the mechanical impedances. The quality factor and damping of each element are also calculated and used in $Z_{m,E}$ and $Z_{m,M}$. The only remaining unknowns in the mechanical impedances are the masses which are easily measurable quantities.

For the remaining parameters, other measurements must be made. Firstly, all of the physical dimensions of the material elements need to be known. To determine the linear electroelastic and magnetoelastic coupling coefficients d_{33} and q_{33} , low frequency tests are conducted independently on the two materials. In each, the resultant strain is plotted versus the applied field where the slope gives the desired constant. Note that these tests are run at the same operating conditions as the final broadband tests (to be discussed in Chapters 4 and 5) as each material parameter is dependent on the prestress, temperature, DC bias, and AC field [5, 9, 11].

The effective coupling given in equations (2.23)-(2.24) is a measure of the coupling of a particular transducer section, not of the material itself. The realities of the system force the effective coupling to contain contributions from sources other than the smart material. Specifically, recognizing that each active element is connected to a corresponding prestress stiffness and that flux leakage exists in the electrical components, then the actual material coupling has been shown by Hall [12] to be

$$k^2 = \frac{k_{eff}^2(k_m + k_m^{ps})}{k_m k_L + k_{eff}^2 k_m^{ps}}, \quad (2.45)$$

where k_m is the section's stiffness from equation (2.25) or (2.26), k_m^{ps} is the prestress mechanism stiffness, k_L is a flux leakage term, and k_{eff}^2 is from (2.23) or (2.24). This coupling is equivalent to that expressed in equation (2.33) and thus is related directly to the variable material properties.

The last values that need to be obtained are the magnetic permeability μ^σ and the electric permittivity ϵ_0 . Each of these is directly related to the effective electrical impedance of their respective elements. While literature values are available for both, in this investigation it is most accurate to determine these values by back solving from the actual inductance and capacitance in the transducer. The determination of the

inductance and capacitance is performed both graphically (from collected electrical impedance data) and physically (with a multimeter). In general a combination of these readings is then used in equations (2.34) and (2.40) to calculate the permeability and permittivity, respectively.

2.2.8 Linear Model Simulations

The last step in the development of the linear model consists of simulating the electromechanical response of the transducer. It is assumed that the input to the system will be an applied voltage, while the output of primary interest is the head mass velocity. In addition, observing the total electrical impedance will reveal and validate several fundamental concepts that have been discussed to this point.

In calculating the velocity, first the current in each section is found from the definition of the total electrical impedance ($Z_{ee} = V/I$) to be,

$$I_E = \frac{V}{Z_{ee,E}}$$

$$I_M = \frac{V}{Z_{ee,M}}$$

with the same voltage applied due to the sections being wired in parallel. Now the velocity contribution from each part is determined by (2.21),

$$v_E = \frac{-T_{me,E} I_E}{Z_{m,E} + Z_L}$$

$$v_M = \frac{-T_{me,M} I_M}{Z_{m,M} + Z_L},$$

where the external load impedance Z_L is assumed zero here, but will be explained further in Chapters 4 and 5. The final step in this simulation is to recognize that the

mechanical series configuration allows for the superposition of the velocities from the two halves, resulting in

$$v = v_E + v_M. \quad (2.46)$$

This procedure also allows for the easy comparison of the individual section responses by graphing just $Z_{ee,E}$ and v_E or $Z_{ee,M}$ and v_M . Each set assumes no electrical input and thus no excitation of the other section but still accounts for the attached mechanical components.

Plots of the electrical impedance magnitude and head mass velocity response are shown in Figure 2.18 for the case of driving just the Terfenol-D section. In part (a), the impedance increases linearly with frequency as expected for an inductive system, and the coupled motional effects are prevalent around the first resonance near 1300 Hz. On the head mass velocity response the resonance peak agrees in terms of frequency with that predicted in the impedance. It is noted that because of the inductive nature of the electrical system and the antisymmetric transduction of Terfenol-D, f_r is at a lower frequency than f_{ar} . Although not exactly equal to the relative maximum and minimum in the impedance, they are in the same progression. The final thing to notice from these figures is that the full model nicely follows the idealized modes around the Terfenol-D section's natural resonance but also depicts how it excites some response of the inactive PMN-PT stack.

In a similar manner, plots of the electrical impedance magnitude and head mass velocity response are plotted with just the PMN-PT section being driven in Figure 2.19. Here the blocked electrical impedance Z_e is purely capacitive and thus is inversely proportional with frequency as shown. Now the coupled motional effects of Z_{mot} dominate near the high frequency mode at 3900 Hz. With this type of electrical

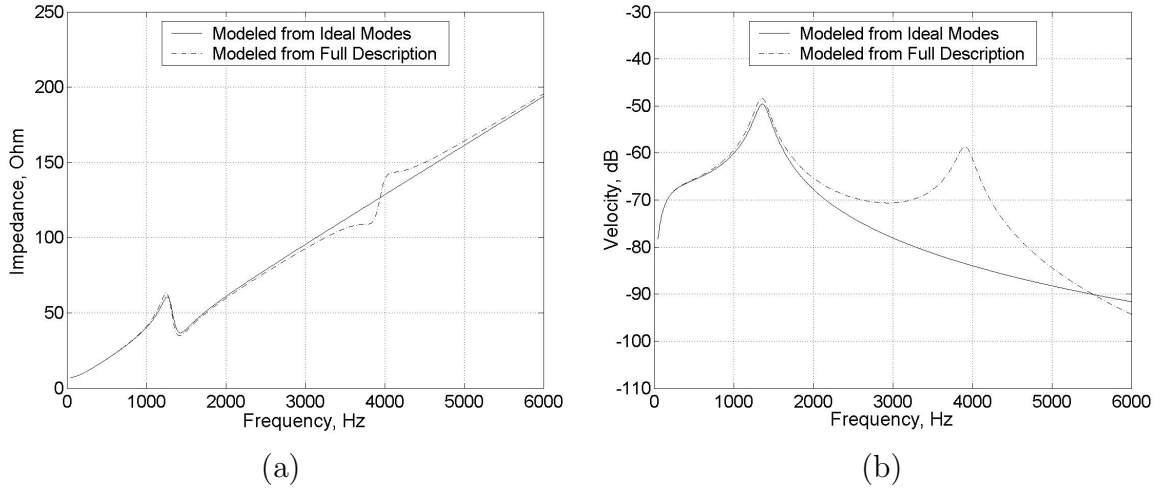


Figure 2.18: Simulated idealized and practical system responses with only Terfenol-D excitation as (a) total electrical impedance magnitudes and (b) head mass velocity responses.

impedance and symmetric transduction, the antiresonance is at a lower frequency than the resonance. From the velocity graph it is again apparent that the full description accounts for the presence of the unexcited Terfenol-D rod, but due to the dynamics of the transducer this off-mode response is not exactly the same as it is with the Terfenol-D section.

The final and most important simulation is to look at the response of the system to complete excitation from both of the smart materials. Once again the graphs of choice are the electrical impedance and the velocity response, plotted in Figure 2.20. Since the two sections are wired together the resulting electrical circuit contains both an inductor and a capacitor, making it a second-order system with its own resonance near 2800 Hz. The familiar trends of the two materials, such as the impedance increasing over the Terfenol-D mode and decreasing through the PMN-PT mode,

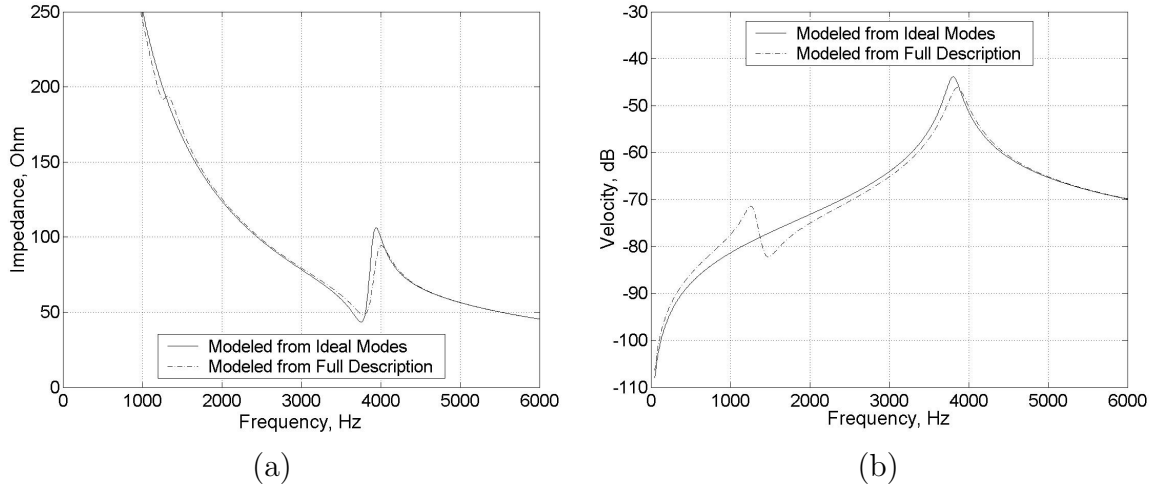


Figure 2.19: Simulated idealized and practical system responses with only PMN-PT excitation as (a) total electrical impedance magnitudes and (b) head mass velocity responses.

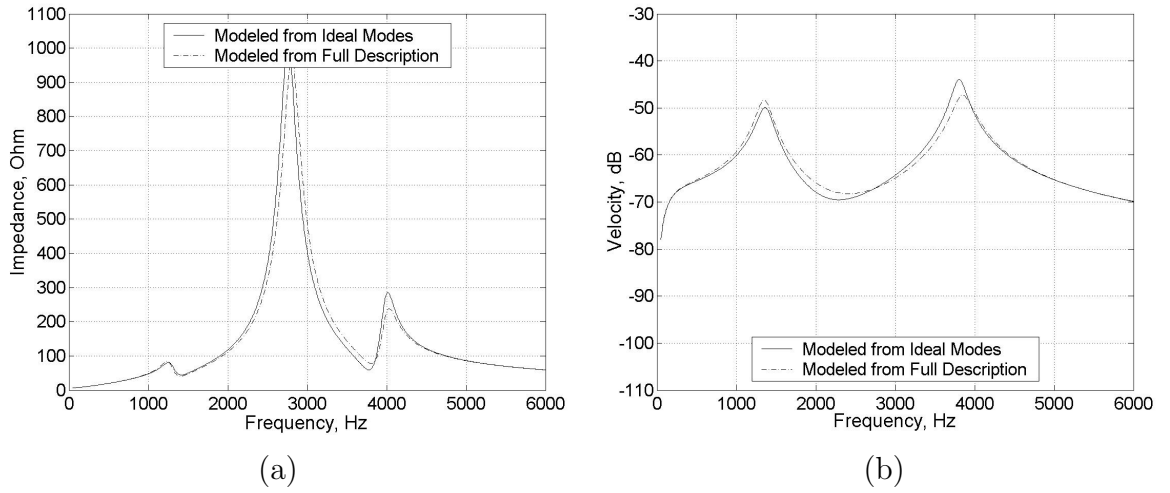


Figure 2.20: Simulated idealized and practical system responses with excitation from both sections as (a) total electrical impedance magnitudes and (b) head mass velocity responses.

are conserved. In Chapter 5 it will be shown how altering the electrical circuit and shifting the resonance can affect this. In the frequency response of the head mass velocity it is obvious that the two resonances overlap with a null in between them, extending the bandwidth to the desired range of 1-6 kHz. It must be noted that in all of these simulations the peaks have been rather sharp due to the relatively low damping in the system, a situation which is addressed in future chapters. These graphs demonstrate only the qualitative features of the various transducer motions; the full results in Chapter 5 will compare these with actual measurements.

CHAPTER 3

NONLINEAR TRANSDUCER MODEL

This chapter presents a complete nonlinear model of the hybrid transducer phenomena. The linear model developed in Chapter 2 is accurate only for low to moderate operating levels and fails to account for the nonlinearities and hysteresis known to be present in the piezoelectric and magnetostrictive processes. Fully utilizing the capabilities of high power actuators requires modeling and control algorithms that accurately incorporate electroelastic and magnetoelastic coupling in a manner consistent with the physical properties of the transducer. A variety of nonlinear modeling techniques currently exist for the two classes of smart material [10, 14, 27, 32], each with its own advantages and implementation issues. This study uses ideas from several of these to formulate its own overall transducer model.

The model is developed in several steps. First the input electrical energy is used to formulate expressions for the internal polarization and magnetization in the two smart materials, taking into account the inherent hysteresis and saturation effects in each. These values are then used to model the active strain component λ in each section. As demonstrated in [6], these strains provide adequate fits to experimental data at lower levels of input but fail at higher values because they do not account for elastic effects in the materials. To address this behavior in the model, an internal force

balance is considered that accounts for the elastic dynamics present in the transducer. The mathematical result of this is a partial differential equation (PDE) that defines the structural coupling of the active elements. The spatial problem is addressed by discretizing the two smart material sections and forming a system of time-continuous ordinary differential equations (ODE), the solutions of which are approximated with standard numerical techniques. A more detailed explanation of these procedures follows.

3.1 Unified Hysteresis Model

Hysteresis and saturation are an inherent property of all ferroic materials over a wide range of operating conditions. The model describing these effects is taken from Smith [31, 32, 33] and represents a unified method of treating both the PMN-PT stack and the Terfenol-D rod. This unified approach starts with Helmholtz and Gibbs energy relations to develop parallel expressions for the polarization and magnetization in the ferroelectric and ferromagnetic materials. The analogous nature of these results is ideal for use in hybrid systems where the duality between regimes is not only conceptually elegant but computationally advantageous as well.

3.1.1 Polarization

Looking first at the PMN-PT element, crystal lattice considerations are used to construct an internal energy balance dependent on electric dipole effects. Incorporating all of the general thermodynamic terms results in a complex expression that is

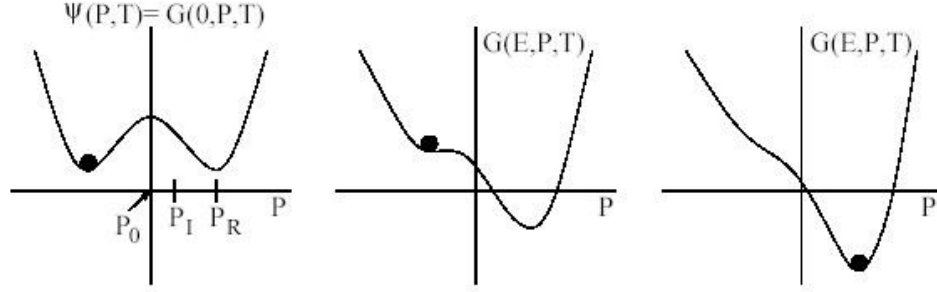


Figure 3.1: Helmholtz energy ψ and Gibbs energy G for increasing field E [32, 33].

difficult to employ or correlate with data. Based on observations, at fixed temperatures the Helmholtz free energy first order approximation can be written as

$$\psi(P) = \begin{cases} \frac{1}{2}\eta(P + P_R)^2 & , P \leq -P_I \\ \frac{1}{2}\eta(P - P_R)^2 & , P \geq P_I \\ \frac{1}{2}\eta(P_I - P_R) \left(\frac{P^2}{P_I} - P_R \right) & , |P| < P_I \end{cases}$$

where ψ is the free energy, P is the polarization, and P_I and P_R respectively denote the positive inflection point and minimum polarization based on free energy graphs like those depicted in Figure 3.1. From this expression the Gibbs free energy can be written as

$$G = \psi - EP,$$

which in the absence of applied stresses describes the energy landscape of homogeneous materials with a uniform crystallographic structure.

The next step in the complete model development [33] utilizes Boltzmann probabilities to determine the local average polarization values throughout the crystal

lattice. The net result of this derivation is the expression

$$[\bar{P}(E, E_c, \xi)](t) = \begin{cases} [\bar{P}(E, E_c, \xi)](0) & , \tau(t) = 0 \\ \frac{E}{\eta} - P_R & , \tau(t) \neq 0 \text{ and } E(\max(\tau(t))) = -E_c \\ \frac{E}{\eta} + P_R & , \tau(t) \neq 0 \text{ and } E(\max(\tau(t))) = E_c \end{cases} \quad (3.1)$$

where

$$[\bar{P}(E, E_c, \xi)](0) = \begin{cases} \frac{E}{\eta} - P_R & , E(0) \leq -E_c \\ \xi & , -E_c < E(0) < E_c \\ \frac{E}{\eta} + P_R & , E(0) \geq E_c \end{cases}$$

denotes the initial orientation. The variable E_c is the coercive field, ξ is an initial distribution of dipoles, and τ are the designated transition times that mark when the value switches sides on the hysteresis kernel. Figure 3.2 shows the implicitly hysteretic shape provided by equation (3.1).

The local polarization expressions hold true only for materials that match the underlying assumptions of homogeneity and uniform fields, and extra considerations

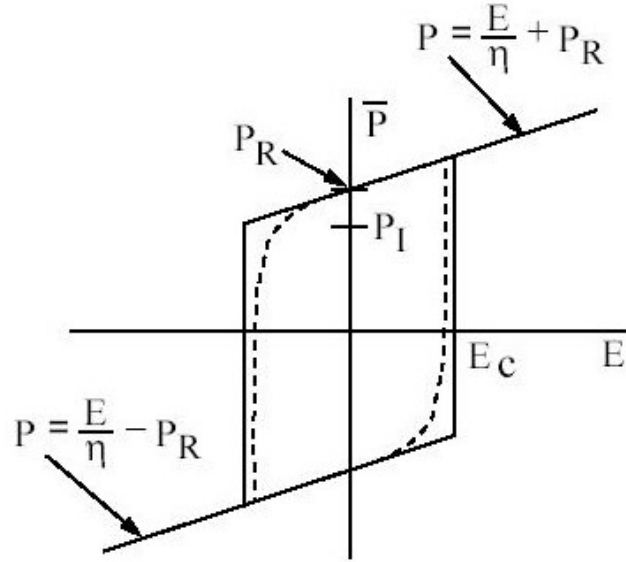


Figure 3.2: Local polarization \bar{P} kernel from Equation (3.1) [33].

are needed to extend these equations to polycrystalline compounds. It is assumed that the effective field E_e is normally distributed about the applied field E , which can be modeled by the statistical density function

$$f(E_e) = c_2 \exp\left(-\frac{(E - E_e)^2}{b}\right). \quad (3.2)$$

Likewise the coercive field values are distributed about the mean \bar{E}_c through a log-normal function

$$f(E_c) = c_1 \exp\left(-\frac{\ln(E_c/\bar{E}_c)^2}{2c}\right). \quad (3.3)$$

The macroscopic polarization model combines (3.2)-(3.3) with the \bar{P} kernel to yield

$$[P(E)](t) = C \int_0^\infty \int_{-\infty}^\infty [\bar{P}(\mathcal{E} + E, E_c, \xi)](t) e^{-\mathcal{E}^2/b} e^{-\ln(E_c/\bar{E}_c)^2/2c} d\mathcal{E} dE_c \quad (3.4)$$

which can be used to model the polarization in a practical material with input electric field $E(t)$.

3.1.2 Magnetization

An identical formulation can be derived for the magnetization M of the Terfenol-D rod incorporating hysteresis and nonuniform fields. Energy diagrams of Terfenol-D show that magnetic moments have two preferred orientations in the crystal, the easy axes group $\langle 111 \rangle$. This creates two potential wells that are defined by the piecewise quadratic Helmholtz energy

$$\psi(M) = \begin{cases} \frac{1}{2}\eta(M + M_R)^2 & , M \leq -M_I \\ \frac{1}{2}\eta(M - M_R)^2 & , M \geq M_I \\ \frac{1}{2}\eta(M_I - M_R) \left(\frac{M^2}{M_I} - M_R\right) & , |M| < M_I \end{cases}$$

which is structurally equivalent to the energy of the PMN-PT section. The corresponding Gibbs free energy is

$$G = \psi - HM.$$

The simplifying assumptions used for the polarization are repeated here, resulting in the hysteretic kernel being defined as

$$[\overline{M}(H, H_c, \xi)](t) = \begin{cases} [\overline{M}(H, H_c, \xi)](0) & , \tau(t) = 0 \\ \frac{H}{\eta} - M_R & , \tau(t) \neq 0 \text{ and } H(\max(\tau(t))) = -H_c \\ \frac{H}{\eta} + M_R & , \tau(t) \neq 0 \text{ and } H(\max(\tau(t))) = H_c \end{cases} \quad (3.5)$$

where

$$[\overline{M}(H, H_c, \xi)](0) = \begin{cases} \frac{H}{\eta} - M_R & , H(0) \leq -H_c \\ \xi & , -H_c < H(0) < H_c \\ \frac{H}{\eta} + M_R & , H(0) \geq H_c. \end{cases}$$

As before, application of stochastic distributions to the homogeneous model gives the bulk magnetization for materials exhibiting polycrystallinity, lattice defects, and internal magnetic interactions. Assuming normally distributed densities the functions can be written as

$$f(H_e) = c_2 \exp\left(-\frac{(H - H_e)^2}{b}\right) \quad (3.6)$$

and

$$f(H_c) = c_1 \exp\left(-\frac{(H_c - \overline{H}_c)^2}{2c}\right). \quad (3.7)$$

Finally, the overall equation that characterizes the magnetization in a material element is then

$$[M(H)](t) = C \int_0^\infty \int_{-\infty}^\infty [\overline{M}(\mathcal{H} + H, H_c, \xi)](t) e^{-\mathcal{H}^2/b} e^{-(H_c - \overline{H}_c)^2/2c} d\mathcal{H} dH_c, \quad (3.8)$$

which is exactly analogous to the polarization expression.

3.2 Active Strain Model

The next step in the model development involves the quantification of the active strain λ generated by each smart material. The strain λ includes components from the

moment rotation in each element but does not include the elastic material response of the type given by Hooke's law $\sigma = \varepsilon E$, which will be incorporated in the next section. At this point the different natures of the piezoelectric and magnetostrictive processes result in a temporary deviation from the parallel model structure developed thus far.

Empirical results show that the strain of the PMN-PT element is more linear and less hysteretic over the same operating range than the magnetostriction of Terfenol-D. This is partially due to the fact that the Terfenol-D element is being driven much nearer to saturation than the PMN-PT stack is for the same applied voltage, and partially due to the intrinsic differences in the materials. The conclusion that is drawn from this is that the linear constitutive relations for piezoelectric materials (2.1)-(2.2) are more valid over this operating range than the equivalent expressions for magnetostrictive materials. Thus it is decided that the linear expressions are acceptable for modeling the strain in the piezoceramic but not the in magnetostrictive element.

The actual value of the active strain for the PMN-PT element can be identified by rewriting the converse piezoelectric effect

$$\varepsilon = \frac{\sigma}{E_y^E} + d_{33}E$$

and separating it into the elastic component to be considered later and the field-induced length change $\lambda = d_{33}E$. To relate this to the polarization, the expression $P = \frac{E}{\eta}$ is employed which gives

$$\lambda_E(t, x) = d'P(t, x), \tag{3.9}$$

where d' is the resultant coefficient of proportionality determined empirically. Note that the hysteretic and saturation effects in the polarization will carry through to the physical strain.

The strain generated by the Terfenol-D rod carries a bit more complexity from the modeling point of view. The material deflection is typically described through an energy formulation with contributions from magnetic, elastic, and anisotropic energies. In the simplified case of an axially applied field and perpendicularly aligned moments due to the compressive prestress, energy minimization [7, 8, 10] yields the relationship

$$\lambda_M(t, x) = \frac{3}{2} \frac{\lambda_s}{M_s^2} M^2(t, x) \quad (3.10)$$

between the magnetization and magnetostriction. It should be noted that this expression is single-valued when experimental evidence suggests that there is some degree of hysteresis in the process. As in [10], it is assumed here that the single-valued function of λ is acceptable and that the hysteretic mechanisms in the process will be accounted for in the M - H interaction.

3.3 Structural Model

The goal in formulating a structural model of the transducer is to develop a PDE system that employs field induced strains λ_E and λ_M as inputs and couples them to the internal elastic dynamics of the materials. The resultant output will consist of the solutions $u(t, x)$ which represent the longitudinal displacements of discrete points along each active section. The following development is general, and is equally applicable to either smart material section.

For modeling purposes, it is easiest to start with a one degree of freedom system and build up towards a full three degree system. The two smart material elements are discretized and modeled with the prestress mechanisms and end masses as boundary conditions. It is assumed that the active material sample has length L , cross-sectional area A , longitudinal coordinate x , density ρ , Young's modulus E , and internal damping c_D . For simplicity all of these material properties are treated as constants along the length. In the most basic one degree of freedom setup, the left end of the rod ($x = 0$) is fixed while the right end ($x = L$) is constrained by the prestress mechanism stiffness and damping k_{ps} and c_{ps} , respectively. The end mass M_L is added as an ideal point mass at $x = L$ as well. The resultant orientation of forces at the free end of the rod are depicted in Figure 3.3.

Under the assumption of linear elasticity the normal stress at a point $0 < x < L$ is given by [10]

$$\sigma(t, x) = E \frac{\partial u}{\partial x}(t, x) + c_D \frac{\partial^2 u}{\partial x \partial t} - E\lambda(t, x) + \sigma_0$$

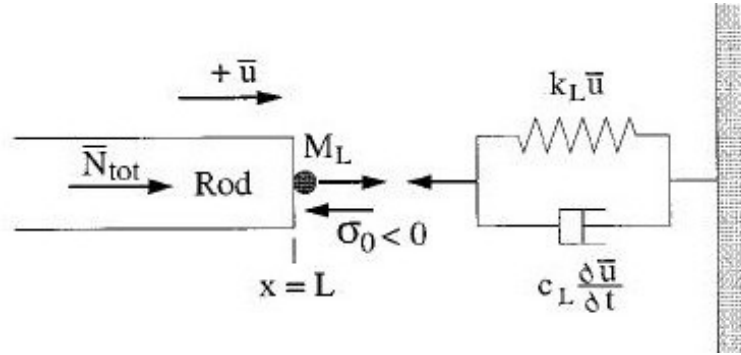


Figure 3.3: Sign convention for the prestress forces, inplane resultant, and rod deflection at boundary condition [10]. The variable \bar{u} represents the total deflection as opposed to the perturbation u employed in the modeling equations.

where λ is given by equation (3.9) or (3.10) and σ_0 denotes the compressive prestress.

Integrating across the face of the material yields the inplane force resultant

$$N_{tot}(t, x) = EA \frac{\partial u}{\partial x}(t, x) + c_D A \frac{\partial^2 u}{\partial x \partial t} - EA \lambda(t, x), \quad (3.11)$$

with u representing the perturbed displacement about the prestress equilibrium position. Force balancing with the distributed mass elements yields the wave equation

$$\rho A \frac{\partial^2 u}{\partial t^2} = \frac{\partial N_{tot}}{\partial x} \quad (3.12)$$

as a model for the internal rod elastic dynamics [10].

Determination of boundary conditions consistent with the physical transducer design is fundamental to the applicability of this approach. In the one degree of freedom configuration this is accomplished in part by imposing $u(t, 0) = 0$. At the other end where $x = L$, the infinitesimal section must satisfy the force balance from the prestress as in Figure 3.3, yielding

$$N_{tot}(t, L) = -k_{ps}u(t, L) - c_{ps} \frac{\partial u}{\partial t}(t, L) - M_L \frac{\partial^2 u}{\partial t^2}(t, L). \quad (3.13)$$

For initial values the entire system is assumed to be in equilibrium prior to excitation such that $u(0, x) = 0$ and $\frac{\partial u}{\partial t}(0, x) = 0$. The wave equation (3.12), boundary conditions (3.13), and initial conditions combine to give the strong form of the model,

$$\begin{aligned} \rho A \frac{\partial^2 u}{\partial t^2} &= \frac{\partial N_{tot}}{\partial x} \\ \begin{cases} u(t, 0) = 0 \\ N_{tot}(t, L) = -k_{ps}u(t, L) - c_{ps} \frac{\partial u}{\partial t}(t, L) - M_L \frac{\partial^2 u}{\partial t^2}(t, L) \end{cases} & \quad (3.14) \\ \begin{cases} u(0, x) = 0 \\ \frac{\partial u}{\partial t}(0, x) = 0. \end{cases} \end{aligned}$$

The more convenient weak form is written by scaling (3.14) by test functions $\phi(x)$ that are used in the numerical approximation. From there integration over the length of the material is performed to get the integral equation containing the boundary conditions implicitly built in. This development is as follows,

$$\begin{aligned}
\int_0^L \rho A \frac{\partial^2 u}{\partial t^2} \phi dx &= \int_0^L \frac{\partial N_{tot}}{\partial x} \phi dx \\
&= N_{tot} \phi \Big|_0^L - \int_0^L N \frac{\partial \phi}{\partial x} \\
&= N_{tot}(t, L) \phi(L) - N_{tot}(t, 0) \phi(0) - \int_0^L N \frac{\partial \phi}{\partial x} \\
&= - \left[k_{ps} u(t, L) + c_{ps} \frac{\partial u}{\partial t}(t, L) + M_L \frac{\partial^2 u}{\partial t^2}(t, L) \right] \phi(L) \\
&\quad - \int_0^L \left[EA \frac{\partial u}{\partial x} + c_D A \frac{\partial^2 u}{\partial x \partial t} - EA \lambda \right] \frac{\partial \phi}{\partial x} dx \tag{3.15}
\end{aligned}$$

with the end result being the weak form of the model. The solution $u(t, x)$ to equation (3.15) provides the axial displacement at every point along the material sample. In the absence of an input λ , the system will have the equilibrium solution $u(t, x) = 0$.

Before discussing the implementation of this model utilizing the $\phi(x)$ test functions, it is helpful to outline the weak form equations for the expanded two and three degree of freedom models. In the two degree case the fixed end at $x = 0$ is replaced with an additional mass and prestress component. The result is that the boundary condition $u(t, 0) = 0$ is replaced with a form similar to that of (3.13),

$$N_{tot}(t, 0) = k_{ps,0} u(t, 0) + c_{ps,0} \frac{\partial u}{\partial t}(t, 0) + M_0 \frac{\partial^2 u}{\partial t^2}(t, 0). \tag{3.16}$$

This implies that in the derivation of the weak form (3.15) the $N_{tot}(t, 0)$ term no longer drops out, yielding the two degree of freedom model

$$\begin{aligned}
\int_0^L \rho A \frac{\partial^2 u}{\partial t^2} \phi dx &= - \left[k_{ps,0} u(t, 0) + c_{ps,0} \frac{\partial u}{\partial t}(t, 0) + M_0 \frac{\partial^2 u}{\partial t^2}(t, 0) \right] \phi(0) \\
&\quad - \left[k_{ps,L} u(t, L) + c_{ps,L} \frac{\partial u}{\partial t}(t, L) + M_L \frac{\partial^2 u}{\partial t^2}(t, L) \right] \phi(L) \\
&\quad - \int_0^L \left[EA \frac{\partial u}{\partial x} + c_D A \frac{\partial^2 u}{\partial x \partial t} - EA \lambda \right] \frac{\partial \phi}{\partial x} dx. \tag{3.17}
\end{aligned}$$

The issue remains to fully expand the model to incorporate both smart materials simultaneously. The best approach is to consider the entire transducer as a two degree of freedom system like that above, but add the center mass to the midpoint of the rod and define different material properties on either side of it. This formulation is fully consistent with the actual design of the transducer, as depicted in Figure 3.4. By defining a different λ on each half of the system, the various drive configurations of the real device can be simulated.

3.4 Implementation

A number of implementation issues arise when trying to simulate the transducer response using the various model components. The mathematical complexity required to accurately describe hysteresis and nonlinearities makes for complicated algorithms

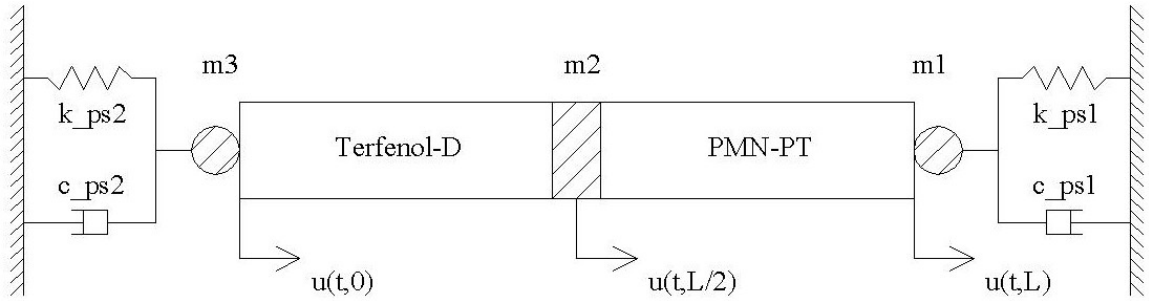


Figure 3.4: Structural model representation of the complete transducer.

and slow computation times. This section outlines the improved techniques that are used to implement the nonlinear system equations.

The expressions for the polarization (3.4) and magnetization (3.8) are initially computed using a Gaussian quadrature approximation of the double integrals. While it is algorithmically straightforward to conditionally determine the values of \bar{P} and \bar{M} using the transition times, the number of comparisons needed is quite large. This significantly diminishes the speed and elegance of the code, and a better approach is typically used.

An alternative is to redefine the local polarization as

$$\bar{P} = \frac{E}{\eta} + P_R \Delta, \quad (3.18)$$

where the matrix Δ contains values of ± 1 to determine the transitions between the upper and lower branches of the kernel. The efficient construction of Δ will accommodate the natural vector forms of the various field values due to the quadrature of the integrals. As a result, the $i \times j$ conditional statements are replaced with a simple matrix multiplication that drastically improves the algorithm. From Smith [33], the formal procedure for this is as follows. First, the initial matrices must be defined as

$$\begin{aligned} \Delta_{init} &= \begin{bmatrix} -1 & \dots & -1 & 1 & \dots & 1 \\ \vdots & & \vdots & \vdots & & \vdots \\ -1 & \dots & -1 & 1 & \dots & 1 \end{bmatrix}_{Ni \times Nj}, \quad \mathcal{E}_c = \begin{bmatrix} E_{c,1} & \dots & E_{c,1} \\ \vdots & & \vdots \\ E_{c,Ni} & \dots & E_{c,Ni} \end{bmatrix}_{Ni \times Nj} \\ \mathcal{E}_k &= \begin{bmatrix} E_k + \mathcal{E}_1 & \dots & E_k + \mathcal{E}_{Nj} \\ \vdots & & \vdots \\ E_k + \mathcal{E}_1 & \dots & E_k + \mathcal{E}_{Nj} \end{bmatrix}_{Ni \times Nj}, \quad \mathcal{O} = \begin{bmatrix} 1 & \dots & 1 \\ \vdots & & \vdots \\ 1 & \dots & 1 \end{bmatrix}_{Ni \times Nj} \end{aligned}$$

and the weight vectors as

$$\begin{aligned} W^T &= [w_1 e^{-\mathcal{E}_1^2/b}, \dots, w_{N_j} e^{-\mathcal{E}_{N_j}^2/b}]_{1 \times N_j} \\ V^T &= [v_1 e^{-(\ln(E_{c1}/\bar{E}_c)/2c)^2}, \dots, v_{N_i} e^{-(\ln(E_{cN_i}/\bar{E}_c)/2c)^2}]_{1 \times N_i} \end{aligned}$$

where E_k is the k th value of the input field. The polarization P_k is then specified by

$$\begin{aligned} \Delta &= \Delta_{init} \\ \hat{P} &= P_R \mathcal{O} + \frac{1}{\eta} \mathcal{E}_c \\ \text{for } k &= 1 : N_k \\ \bar{P} &= \frac{1}{\eta} \mathcal{E}_k + P_R \Delta \\ dE &= E_k - E_{k-1} \\ \Delta &= \text{sgn}((\mathcal{E}_k - \text{sgn}(dE) \mathcal{E}_c) .* (\bar{P} - \text{sgn}(dE) \hat{P}) .* \bar{P}) \\ \bar{P} &= \frac{1}{\eta} \mathcal{E}_k + P_R \Delta \\ P_k &= C W^T \bar{P}^T V \\ \text{end} \end{aligned}$$

where sgn denotes the signum function and $.*$ indicates individual component multiplication. As expected, the above process is directly applicable to the magnetization model as well. This algorithm operates at a level of efficiency significantly higher than the original, allowing it to be potentially employed in real-time control applications. To characterize all of the numerical parameters in both the P and M equations, the simulated curves are optimally fit to experimental data.

With the polarization and magnetization curves the active strain components are calculated from equations (3.9)-(3.10). Determination of the constants in the expressions are based on a combination of values collected from literature and physical data. The time dependence is carried through from the input fields but the spatial considerations, particularly the variations along the Terfenol-D rod, are ignored.

Structurally there are implementation issues as well. In order to approximate the solution to the weak form models, a spatial Galerkin discretization is used followed by a temporal finite difference approximation [10]. On a single smart material the

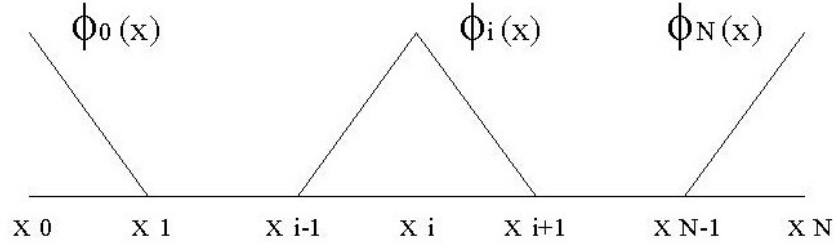


Figure 3.5: Linear test functions $\phi_0(x)$, $\phi(x)$, and $\phi_N(x)$.

interval $[0, L]$ can be divided up into partitions with points x_i and step size $h = L/N$, where N denotes the number of subintervals (implying $N + 1$ points). The spatial basis test functions $\phi_i(x)$ take the form of linear splines,

$$\phi_i(x) = \frac{1}{h} \begin{cases} (x - x_{i-1}) & , x_{i-1} \leq x < x_i \\ (x_{i+1} - x) & , x_i \leq x \leq x_{i+1} \\ 0 & , \text{otherwise} \end{cases} \quad i = 1, \dots, N-1$$

$$\phi_N(x) = \frac{1}{h} \begin{cases} (x - x_{N-1}) & , x_{N-1} \leq x \leq x_N \\ 0 & , \text{otherwise} \end{cases}$$

which are plotted in Figure 3.5. This form of $\phi(x)$ ignores calculation at the one end of the rod because it is designed for the one degree of freedom setup with the fixed end at $x = 0$. To account for the other designs another function must be added,

$$\phi_0(x) = \frac{1}{h} \begin{cases} (x_1 - x) & , 0 \leq x \leq x_1 \\ 0 & , \text{otherwise} \end{cases}$$

which is a mirror of the half hat over the final interval x_N . The solution $u(t, x)$ follows from the above definitions to be an expansion having the form

$$u^N(t, x) = \sum_{j=0}^N u_j(t) \phi_j(x).$$

Noting the separation of variables in the previous equation, if this form for u is substituted into the weak form model of equation (3.15) it yields the discrete second-order time dependent system

$$[Q]\ddot{\vec{u}}(t) + [C]\dot{\vec{u}}(t) + [K]\vec{u}(t) = \vec{f}(t), \quad (3.19)$$

where the matrices and vectors are defined as

$$[Q]_{ij} = \begin{cases} \int_0^L \rho A \phi_i \phi_j dx + M_0 & i = 0 \text{ and } j = 0 \\ \int_0^L \rho A \phi_i \phi_j dx & i \neq (0|N) \text{ and } j \neq (0|N) \\ \int_0^L \rho A \phi_i \phi_j dx + M_L & i = N \text{ and } j = N \end{cases}$$

$$[C]_{ij} = \begin{cases} \int_0^L c_D A \phi'_i \phi'_j dx + c_{ps,0} & i = 0 \text{ and } j = 0 \\ \int_0^L c_D A \phi'_i \phi'_j dx & i \neq (0|N) \text{ and } j \neq (0|N) \\ \int_0^L c_D A \phi'_i \phi'_j dx + c_{ps,L} & i = N \text{ and } j = N \end{cases}$$

$$[K]_{ij} = \begin{cases} \int_0^L E A \phi'_i \phi'_j dx + k_{ps,0} & i = 0 \text{ and } j = 0 \\ \int_0^L E A \phi'_i \phi'_j dx & i \neq (0|N) \text{ and } j \neq (0|N) \\ \int_0^L E A \phi'_i \phi'_j dx + k_{ps,L} & i = N \text{ and } j = N \end{cases}$$

$$\vec{u} = [u_0(t), u_1(t), \dots, u_N(t)]$$

$$[\vec{f}]_i = \int_0^L E A \lambda(t, x) \phi'_i dx$$

for the two degree of freedom system (3.17). The last consideration is the case where the rod is not uniform but rather a combination of two distinct smart materials.

From Figure 3.4, the total transducer can be separated into two smaller intervals each covering one active material. The integrals in the matrix expressions will be uniform along one entire interval until the midpoint of the structure is reached. There the differences in material properties will automatically arise from the integration of

bias functions and result in the proper average of Terfenol-D and PMN-PT effects at the center, essentially coupling the two in mechanical series.

The various integrals in the matrix indices all contain some product of bias functions or bias function derivatives. Computing these with conditional statements can prove inefficient and slow when done over the entire interval. A more robust algorithm can be used by accounting for the fact that the bias function products are nonzero only when within one point of each other on the i and j intervals. This limits computation to just the main diagonal and adjacent diagonals rather than the entire matrix. For the actual numerical integration a Gaussian quadrature routine is used that looks at four points along each half of a hat function. Since the test functions $\phi(x)$ appear identically at each point on the sample the x dependence is eliminated from the integrals, and thus the computed quadrature results at all x_i will be equal (along one distinct material section only). This allows for the value at one point to be calculated and simply propagated to all of the other discrete points in the material.

With the matrix coefficients determined, the system response needs to be numerically approximated at discrete times. To this end the system matrices $[W]$ and $[F]$ are created as

$$W = \begin{bmatrix} 0 & I \\ -Q^{-1}K & -Q^{-1}C \end{bmatrix}, \quad \vec{F}(t) = \begin{bmatrix} 0 \\ -Q^{-1}\vec{f}(t) \end{bmatrix}, \quad (3.20)$$

and the second-order system (3.19) is rewritten as a first order state space system in the form

$$\begin{aligned} \dot{\vec{y}}(t) &= W\vec{y}(t) + \vec{F}(t) \\ \vec{y}(0) &= \vec{y}_0 \end{aligned} \quad (3.21)$$

where $\vec{y}(t)$ is arranged as $[\vec{u}(t), \dot{\vec{u}}(t)]^T$ and \vec{y}_0 denotes the initial positions and velocities. The system allows for temporal solutions to be determined through the iteration

$$\begin{aligned}\vec{y}_{j+1} &= \mathcal{W}\vec{y}_j + \frac{1}{2}\mathcal{F}[\vec{F}(t_j) + \vec{F}(t_{j+1})] \\ \vec{y}_0 &= \vec{y}(0)\end{aligned}\tag{3.22}$$

where t_j is the time value for which the response is \vec{y}_j . The matrices

$$\begin{aligned}\mathcal{W} &= \left[I - \frac{\Delta t}{2}W \right]^{-1} \left[I + \frac{\Delta t}{2}W \right] \\ \mathcal{F} &= \Delta t \left[I - \frac{\Delta t}{2}W \right]^{-1}\end{aligned}$$

contain the differential time step Δt and once computed can be directly implemented above. The \vec{y} output vector contains the time-domain position and velocity at each point along the transducer. In order to generate the desired bandwidth plots, the head mass velocity signal (typically \vec{y}_{2N}) is converted into the frequency domain through a Fourier transform.

CHAPTER 4

TRANSDUCER DESIGN AND TESTING

This chapter presents the design and testing of a hybrid PMN-PT / Terfenol-D transducer constructed in the Smart Materials and Structures Laboratory. The primary issues that need to be considered in this design are the mechanical components, the magnetic circuit, and the electrical drive system. From the testing standpoint, it is emphasized that the various sensors and data acquisition systems must be fully characterized so that the responses of the device are accurately captured. Additionally, the optimum drive conditions for each test must be determined and controlled to ensure correct functionality of the transducer.

4.1 Mechanical Design

The design of the complete mechanical system is centered around the two smart material elements (Figure 4.1). From the transducer modeling it is known that the active materials dominate the stiffness in the system, and the rest of the design can be based around these values. Therefore the starting point of this design is the ETREMA Terfenol-D rod 50.8 mm (2 in) in length and 6.35 mm (0.25 in) in diameter. The piezoceramic material employed is an EDO Ceramic PMN-PT stack 16 mm (0.63 in) in diameter and consisting of 62 individual layers for a total length of 35.2 mm

(1.385 in). Using these values in the linear elastic modeling of material stiffness yields approximately $28\text{e}6$ N/m and $120\text{e}6$ N/m for the Terfenol-D and PMN-PT elements, respectively.

With the smart materials accounting for the compliance elements, the remaining fundamental parts that need to be designed are the three vibratory masses. Benchmarking from previous Tonpilz designs [1, 2, 3, 28, 34] reveals that equal diameter cylindrical masses are the norm, with the head mass occasionally being tapered outward. Using the approximate stiffnesses of the two smart materials, the suggested mass ratio of roughly 1 : 2 : 2.5, and the target resonances of 1300 and 3900 Hz, it is calculated that the head, center, and tail masses should have values of approximately 0.33 kg, 0.67 kg, and 0.83 kg. These numbers represent the overall lumped mass values, which includes not only the masses themselves but also the attached prestress mechanism, a percentage of the compliant material, and the magnetic circuit. Assuming that the center and tail masses are made of non-magnetic steel and the head mass is made of aluminum, the necessary volume of each can be easily calculated. Several considerations lead to a practical diameter of 76.2 mm (3 in) being chosen from which the rest of the dimensions fall into place.

To prepare the masses for machining some further considerations must be incorporated. The compressive prestress that is applied to each material is often implemented by placing a Belleville washer under the head of a bolt running through the center axis of the transducer. Tightening the bolt compresses the washer and loads the entire structure but still allows for the smart material to strain. Considering the lack of a hole in the available samples due to their small size, the center bolt concept is expanded to three bolts located around the exterior of the materials but still running

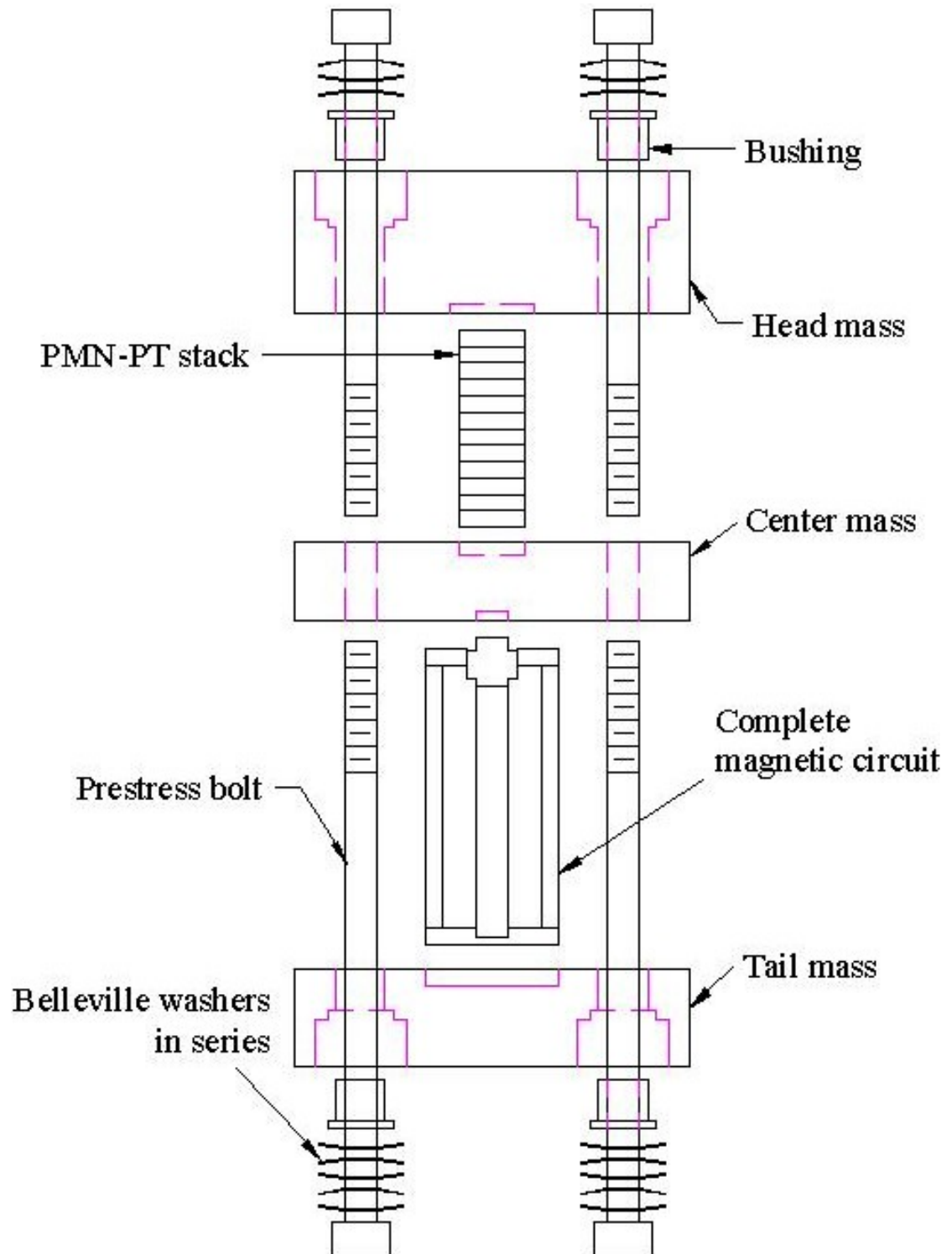


Figure 4.1: Construction diagram of the total hybrid transducer.

through the masses along the primary rod axis. The design consequences of this feature are twofold. First, the center mass must allow for all six bolts to rigidly thread into it, and second, each end mass must contain three bolt holes and corresponding bushings for accurate alignment.

In general, the Belleville washer force-deflection relationship is nonlinear and depends solely on the geometry and material of the washer. The washers employed here have dimensions of $h=.0225$ in, $t=.0135$ in, $D_o=0.50$ in, and $D_i=0.25$ in, which are designed to provide a quasi-linear force output over the range of interest as illustrated in the measured data of Figure 4.2. From this experiment, the linear stiffness value of a single washer is approximated as $k_{ps}=0.684\text{e}6$ N/m. To reduce the effective stiffness of the springs, they are stacked in series combinations of three for the PMN-PT section and five for the Terfenol-D section. A more detailed examination of Belleville washers can be found in [24].

Final geometric modifications to the three masses include countersinking space for the prestress bolt heads to ensure a flat radiating surface. To assist in the structure's alignment shallow depressions are built into each mass to interface with the two active sections. Additionally, notches are cut out where needed to allow for the electrical wires to protrude unimpeded. With these final additions, the mechanical drawings for the transducer components are completed as shown in Appendix B. The construction diagram of the complete transducer is depicted back in Figure 4.1. When all of the components are combined the final values of the masses come out to be 0.308 kg for the head, 0.670 kg for the center, and 0.777 kg for the tail. These slight deviations from the target values are found to cause a negligible change in the system bandwidth.

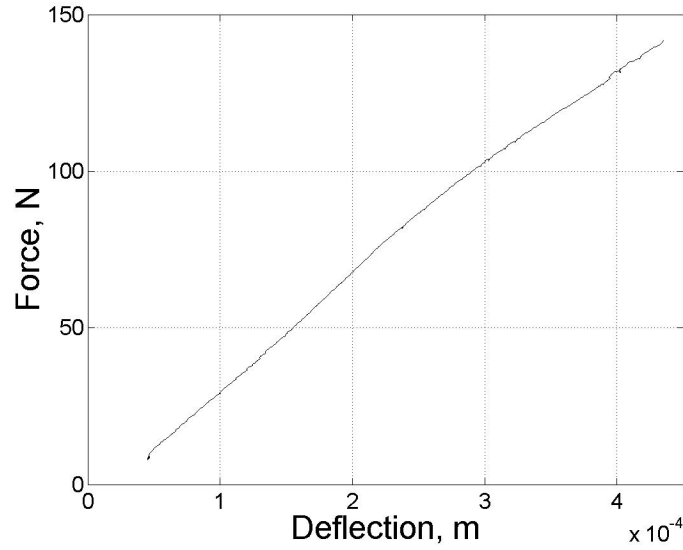


Figure 4.2: Experimental force versus deflection curve for the Belleville washers used in the prestress mechanism.

Once the parts are assembled the transducer is ready for testing. When the two sections are bolted together, the completed transducer measures 152.4 mm (6 in) in length as shown in Figure 4.3(a). For accurate testing, the transducer must be removed from any surface that could influence its dynamics, because for example setting it on a table will restrict the motion of the tail mass. To this end the entire transducer is placed inside of a 76.2 mm (3 in) PVC tube with a neoprene/cork ring around each mass acting as an isolator. A thin slit is cut in the tube to allow the various wires to escape. As shown in Figure 4.3(b) the complete tube assembly is suspended from a Unistrut housing structure to prevent exogenous dynamics from affecting transducer data.

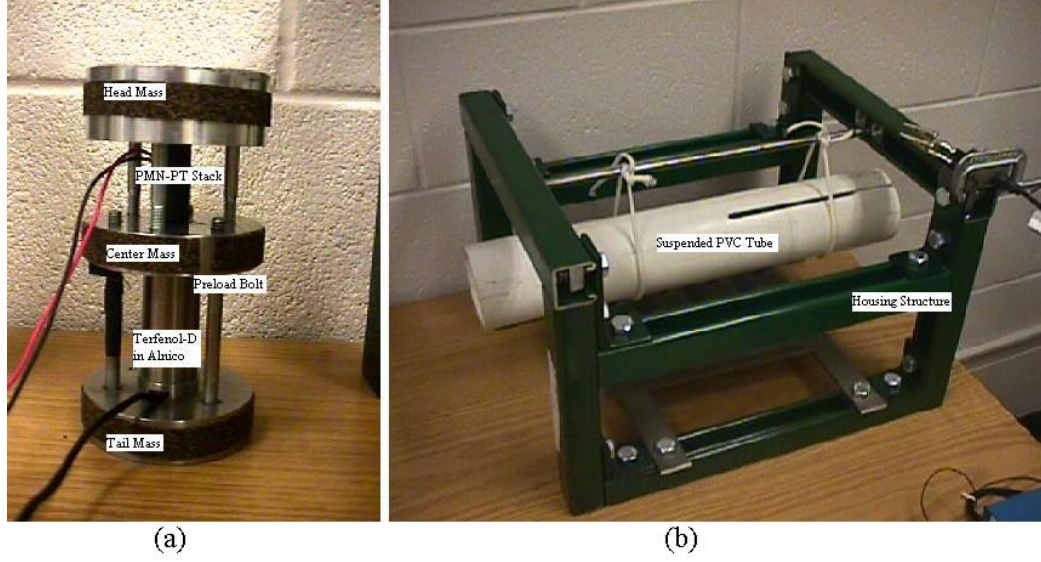


Figure 4.3: Complete (a) PMN-PT / Terfenol-D transducer and (b) external housing structure.

4.2 Magnetic Circuit Design

Ideally, activation of Terfenol-D requires a perfectly uniform magnetic induction throughout the material. To approximately generate this effect in the transducer, an efficient magnetic return path needs to be incorporated. A key concern in magnetizing the sample is that the relative permeability of Terfenol-D under typical conditions is about $\mu_r = 5$ [12, 19]. Compared with values in the thousands for steel, it is apparent that careful design of the magnetic circuit is needed to maximize the potential magnetization of the Terfenol-D element. The key components in this flux path are the sample itself, the cylindrical permanent magnet, and the various steel connecting pieces.

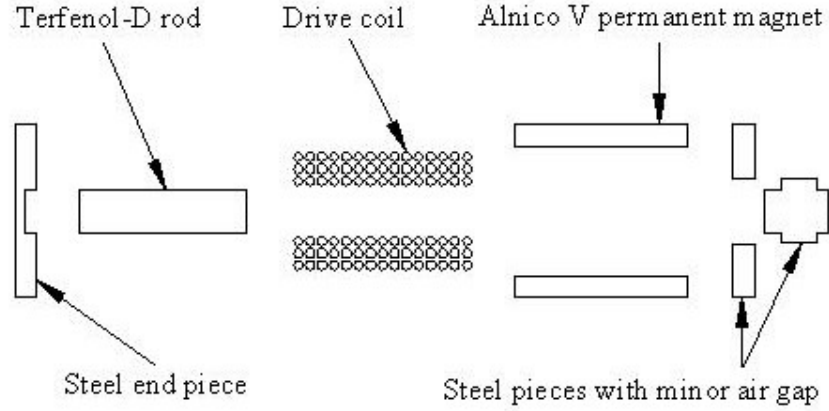


Figure 4.4: Cross-section of the closed magnetic circuit components.

Encasing all of the magnetic components is the Alnico V permanent magnet providing a constant field value of approximately 125 Oe (10 kA/m). The magnet has inner and outer diameters of 19 mm (0.75 in) and 25.4 mm (1 in) and a length of 50.8 mm (2 in). An axial slit helps reduce the negative effects of high frequency eddy currents. Connecting this to the Terfenol-D rod are 1018 steel discs that provide a favorable magnetic flux path into and out of the sample. In this stage a small air gap is required to allow for the Terfenol-D to strain. Often this will significantly hinder the flux, but the gap is kept very thin and filled with a conductive grease to help maintain a strong return path. The final magnetic structure is depicted in Figure 4.4 where all of the components are separated.

The magnetic circuit is driven by a solenoid that consists of 1232 turns of wound 26-AWG magnet wire, has a field rating of 300 Oe/A, has a resistance of 6.73 Ω , and has an inductance of about 6 mH when filled with the Terfenol-D rod. The coil's inner diameter is slightly larger than the sample itself so as to not hinder the strain, and

its length is roughly equal to that of the Terfenol-D rod as well. The innermost layer of the coil is a separately wound pickup coil with 112 turns. This is used primarily for sensing the induction in the smart material. The coils are wound with the help of a variable speed motor and layers of the epoxy EpoTek T1709 spread throughout to hold it together. This epoxy also aids the heat conduction away from the center sample, which is important because the current can cause significant heating and Terfenol-D properties will vary with temperature.

The magnetic finite element package FEMM v3.2 is used to simulate the system to ensure that flux lines converge through the Terfenol-D sample and that leakage is not predominate. The 2-d schematic of the transducer is imported and some current input assumed. The simulation results are shown in Figure 4.5, where the relative darkness is a measure of the flux density. In addition the software computes the variation in induction along the length of the rod due to issues with the practical solenoid. This result is plotted in Figure 4.6 for a relatively low input field.

4.3 Amplifier Configuration

The magnetic drive coil and the PMN-PT stack both require direct voltage application to generate their respective fields. This input voltage is provided by two Techron 7780 amplifiers connected in electrical series, a configuration that is capable of producing up to $240 V_{rms}$ due to its voltage gain of 60. Since the test transducer is not capable of handling such high levels, the amplifiers are used at low signal regimes and thus need to be characterized at those levels. In particular, the high frequency response of the amplifier output needs to be considered because any practical amplifier will at some point show a combination of magnitude roll off and undesirable

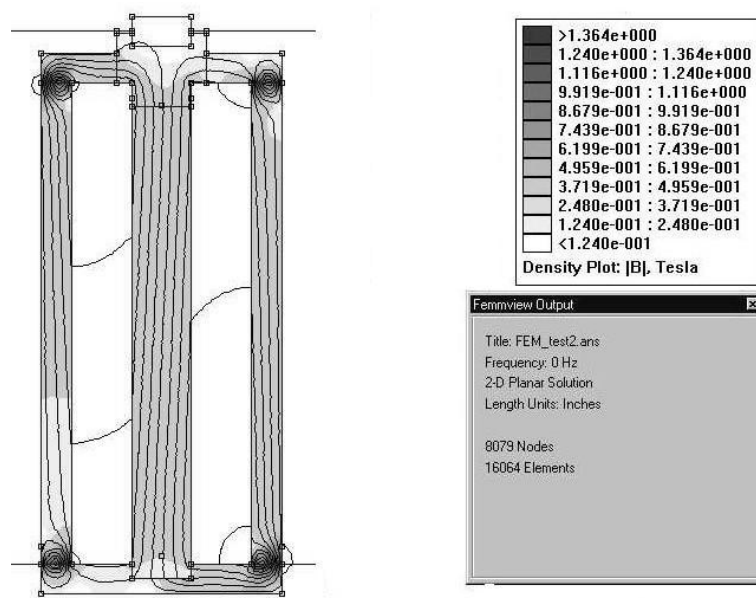


Figure 4.5: Finite element computation of the performance of the magnetic circuit.

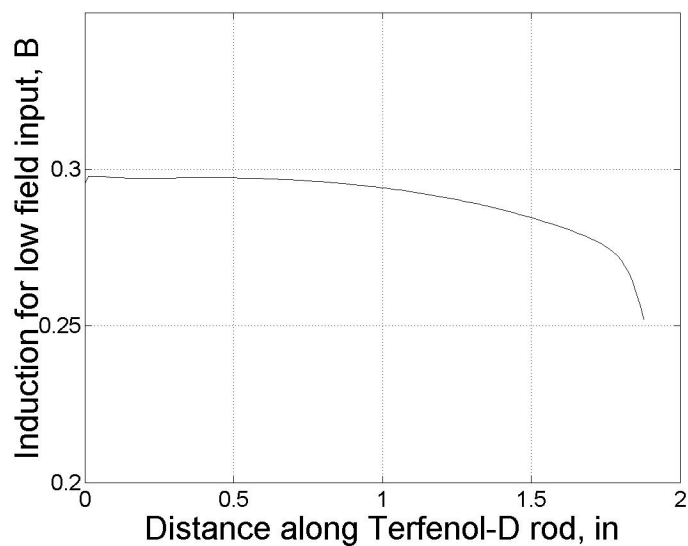


Figure 4.6: Predicted variation of induction along the axis of the Terfenol-D rod calculated with FEMM v3.2.

phase shifts. Considering that this transducer is targeted for use up to 6 kHz and may have potential well past that, it is necessary to know the behavior of the amplifiers at these frequencies.

To test for output degradation such as roll off or phase shifts, all three types of electrical load (resistor, capacitor, and inductor) need to be considered because the amplifier output is partially dependent on impedance. The tests are conducted by connecting each component individually to the amplifiers and measuring the transfer function of voltage across the load to voltage input to the amps. Each test is run with the maximum allowable 20 kHz frequency span and an input of 100 mV of white noise. Any drop off in the transfer function magnitude or sudden shifts in the phase will be evidence that the amplifiers have issues that need to be accounted for. Further tests are run at discrete frequencies and compared with the trends from the random tests. The conclusion from the tests is that the amplifiers have a steady voltage gain of approximately 60 up to at least 20 kHz, with only minor changes resulting from the type of load impedance. A small consistent phase shift is observed at the rate of $-1^\circ/\text{kHz}$. The full results of this procedure are presented in Appendix C.

4.4 Data Collection

Experimental data is collected from a variety of electrical and mechanical sources. An accurate measurement of each transducer variable is necessary to quantify the output response of the system, to address the behavior of the electromechanical coupling, and to provide reasonable values for the material properties. For this purpose a range of sensors are used in this investigation.

On the mechanical side of the transducer, the primary variables of interest are the motion of each mass, both at quasi-static frequencies and over the full bandwidth. For low frequency measurements a Lucas Schaevitz MHR-025 linear variable differential transformer (LVDT) with a sensitivity of 1.25 V/mil is used to capture the small strains produced by both the Terfenol-D and PMN-PT elements. The sensor itself is fixed on a test stand above the mass in question with the core located on a thin rod that is gently fixed to the mass face with wax. The instrument occasionally suffers from noise issues, particularly at 60 Hz, so in most cases the LVDT signal is low-pass filtered to alleviate these errors.

For measurements at higher frequencies PCB U353B16 accelerometers, in conjunction with the PCB 482B05 signal conditioning box, are used to record the actual acceleration of each mass. These sensors thread directly onto the masses to ensure the best possible coupling of the instrument to the real motion. The resulting data signal can be numerically integrated to determine the velocity or position response as desired.

From the electrical side of the transducer it is necessary to know the voltage and current values associated with each smart material section. The applied voltage across the two active elements is measured directly with an appropriate cable. The amplifiers are equipped with a convenient current monitoring system that outputs a small voltage signal proportional to the current flow out of the amplifiers and into the transducer. Knowledge of the gain on this function (18.7 A/V) allows for a direct scaling into true current. The ratio of the measured voltage and current gives the total electrical impedance that is of particular use in analyzing the dynamics of the structure.

In the magnetostrictive section of the device, the pickup coil allows for the voltage induced by flux changes to be read directly across the coil's terminals. Connecting these terminals to a Walker Scientific model MF-5D integrating fluxmeter results in a voltage output directly proportional to the magnetic induction B . This instrument applies equation (1.10) to the voltage signal where the constant NA is the product of the number of turns in the pickup coil and the mean area of one loop.

The hardware employed for data acquisition includes a Data Physics SignalStar Vector dynamic signal analyzer and accompanying Mobilyzer 4.0 software. This system has five input channels that accept voltage readings up to ± 10 V and performs transfer function analysis on all desired combinations. The output channel can be configured for a variety of signals that are used as input to the amplifiers. To create the magnetic and electric offsets often needed in testing, a variable external DC circuit is electrically combined with the AC output from the Data Physics prior to amplification.

4.5 Test Parameters

The first experiments consist of applying quasi-static sinusoidal voltages from the Data Physics system into each smart material and measuring the output displacements with the LVDT. Tests are run initially at low levels (± 5 V input) to ensure that the materials respond properly before they are driven with higher (± 75 V) fields. One end of the transducer is clamped to the work table, limiting the output motion to one degree of freedom, in order to make use of the single LVDT instrument. From the resultant strain versus field “butterfly” curve of the Terfenol-D section a magnetic bias and AC drive level were chosen to limit the motion to the steepest linear region

on the curve. All subsequent broadband testing is done at the operating levels so determined.

The tests of the high frequency bandwidth are conducted with a low drive level and corresponding bias to maximize the linearity in the material responses. To excite the structure, low level (2.1 V) white noise voltage is generated by the Data Physics system and combined with the appropriate DC offset (2.1 V) to ensure that each section sees only zero-to-peak voltage. The upper frequency span on the data collection ranges from 5 to 20 kHz using maximum resolution of the DAQ system. The measured quantities in these tests include the applied voltage and current to the transducer and the output acceleration at each mass. From these the target transfer functions voltage per current (impedance) and velocity per voltage (bandwidth) are calculated.

Experiments are conducted with each individual section driven independently and with the two wired in parallel. In addition, to study the effect of shifting the electrical resonance an external 378 nF capacitor is wired in parallel with the 251 nF PMN-PT stack as well. This alters the effective capacitance in the circuit, and thus the frequency of electrical resonance, to see what changes appear in the bandwidth. Every broadband test is repeated when an external mechanical load impedance is added to the radiating face of the head mass. The PVC tube is packed full of duct seal on the one side of the transducer in an attempt to simulate the loading effects of water that this design would see if actually used in sonar applications [2]. The results and implications of all of these tests are presented in Chapter 5.

CHAPTER 5

RESULTS AND ANALYSIS

Experiments are conducted on the test transducer as a means of determining material properties for and validating the formulation of the various system models. Low frequency tests provide data on the strain-field relationships and quantify the hysteresis in the system. Broadband frequency experiments validate the extension of the velocity response bandwidth to the 1-6 kHz range.

5.1 Low Frequency Model and Test Results

Quasi-static time domain tests are performed for purposes of determining the low field drive regime to be used for broadband driving of the transducer. Figure 5.1 shows strain versus magnetic field curves collected from the transducer when driving solely the Terfenol-D section at 500 mHz. The overall “butterfly” shape is apparent, with the material exhibiting positive strain in response to applied field in either direction. The deviation of the center crossover point from zero field is due to the 125 Oe (10 kA/m) DC bias of the Alnico permanent magnet. The minor loop on the right branch of the curve depicts the low drive level employed in the subsequent broadband tests, chosen for its location on the steep linear region of the total curve. Corresponding

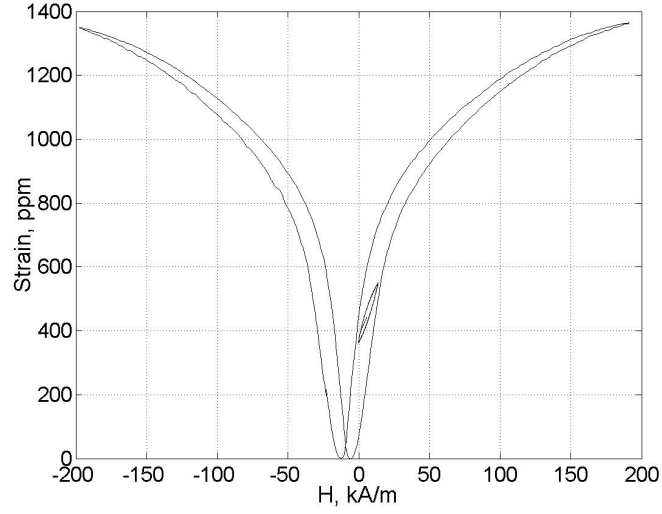


Figure 5.1: Biased strain versus magnetic field data collected from the Terfenol-D section at 500 mHz. The minor loop depicts the drive range for subsequent broadband tests.

to this data is the measured induction versus field graph shown in Figure 5.2, again with minor loop.

In order to generate the low level excitation depicted, the magnetic bias of the Alnico is increased to 220 Oe (17.6 kA/m) by adding 2.1 V DC to the drive coil. The minor loops are then created by applying an additional ± 2.1 V AC to the drive coil, for a total zero to peak field of 190 Oe (15.2 kA/m). The resulting drive signal must also be applied to the PMN-PT stack, where a 0 - 4.2 V input is equivalent to a zero to peak electric field of 7 kV/m. Figure 5.3 shows the results of driving solely the PMN-PT stack at this level. The major loop is a simulated curve exemplifying the general shape, while the minor loop is actual test data. It should be noted that this signal contained some noise at 60 Hz which was removed via a software digital filter.

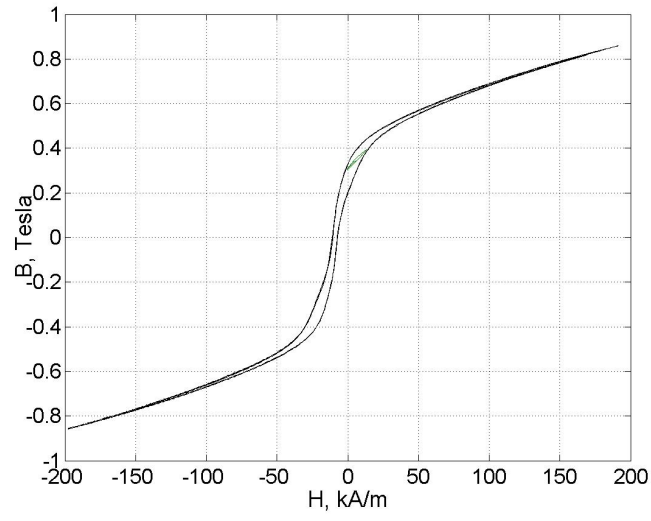


Figure 5.2: Magnetic induction versus magnetic field data collected from the Terfenol-D section at 500 mHz, showing biased major and minor loops.

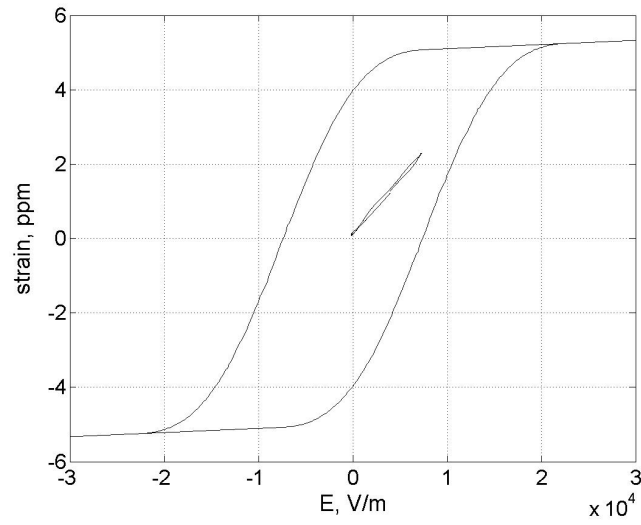


Figure 5.3: Strain versus field data collected from the PMN-PT stack at 500 mHz.

The hysteresis in this strain loop is seen to be small, and the overall slope of the data gives the linear piezoelectric coupling coefficient d_{33} .

The nonlinear model presented in Chapter 3 can be used to produce low frequency graphs to compare with collected data. At this point, however, the model fit to the data is not optimized through the various numerical constants as would be required for truly accurate simulations. Notwithstanding, the general applicability of the nonlinear model can be seen by the qualitative similarities between the data in Figures 5.1 and 5.2 and the model output in Figures 5.4 and 5.5.

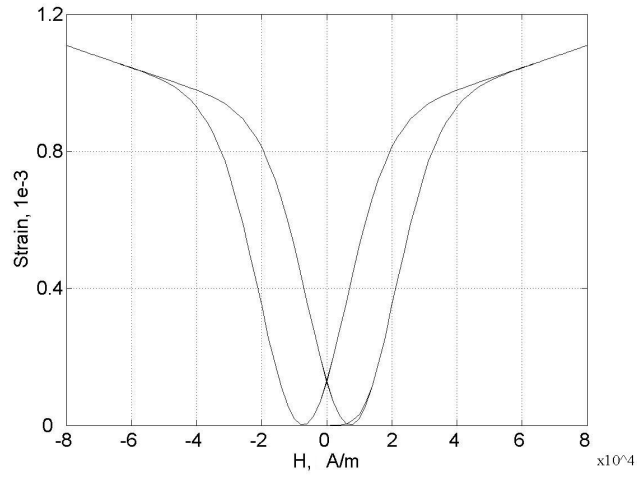


Figure 5.4: Strain versus magnetic field for the Terfenol-D section simulated with the nonlinear model presented in Section 3.2.

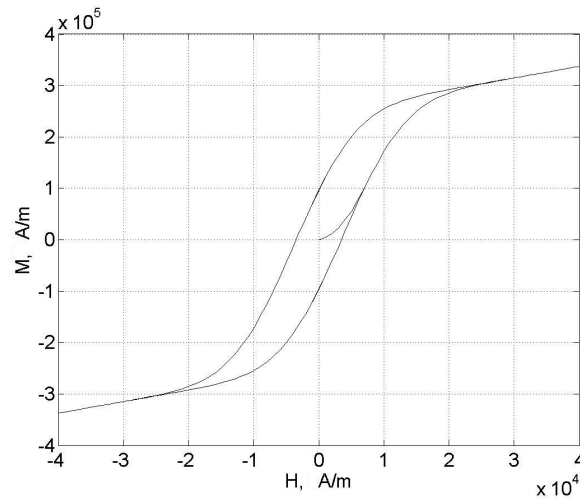


Figure 5.5: Magnetization versus magnetic field for the Terfenol-D section simulated with the nonlinear model presented in Section 3.1.2.

5.2 Broadband Model and Test Results

In all broadband tests, random white noise excitation in the 0 - 4.2 V range is applied to each smart material section. The full complement of electrical impedance and mechanical acceleration frequency response functions are measured from the two transducer sections using the equipment reviewed in Chapter 4. The analysis techniques previously discussed are applied to the impedance and admittance loops to determine the effective material properties for use in the model simulations. The various results and implications of all empirical and calculated data are discussed below.

5.2.1 Terfenol-D Section

In all tests of the Terfenol-D section, the voltage excitation is applied across the terminals of the magnetic drive coil while the PMN-PT section is left as an open circuit. The first tests are run with the transducer operating with no external load. Figure 5.6 shows the head mass velocity response dominated by the Terfenol-D section's resonance peak, which is rather sharp due to the lack of damping. The modeled data in this case is only from the full linear transducer description. The excited motion of the PMN-PT mode is significant, and appears at a slightly higher frequency in the experimental data than in the model simulation. This is due to the open circuit configuration of the piezoceramic stack causing an increase in its stiffness. Because the model uses values obtained from the complete closed circuit transducer, it fails to account for this shift.

The other result of primary interest is the electrical impedance. Figure 5.7 depicts the magnitude of this function, with the linear model result overlaid onto the measured

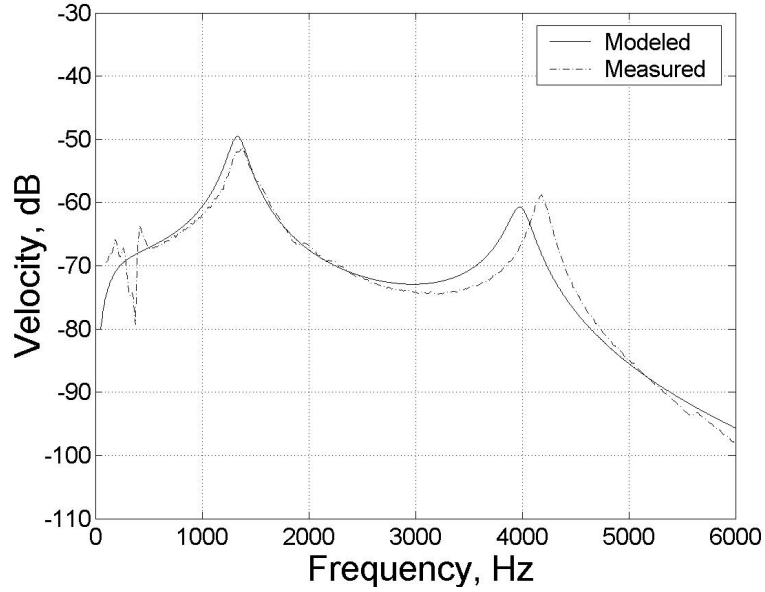


Figure 5.6: Head mass velocity response with only Terfenol-D excitation.

data. Both show the anticipated linear increase of Z with frequency due to the inductive nature of the solenoid. The coupled motional effects near 1300 Hz agree with the section's resonant frequency from the velocity response, while the measured impedance also shows smaller effects from the excited PMN-PT motion at 4100 Hz. The circular mobility loop in Figure 5.8 is the same electrical impedance data plotted in Nyquist format. The loop's location in the first quadrant is indicative of the transducer section's electrical properties ($j\omega L$ places it along the positive imaginary axis) while the diameter and roundness are measures of the transduction.

The above procedure is repeated with the transducer connected to the duct seal loading. With identical drive conditions, the presence of radiation impedance adds a Z_L term to the existing form of the mechanical impedance, the net result of which

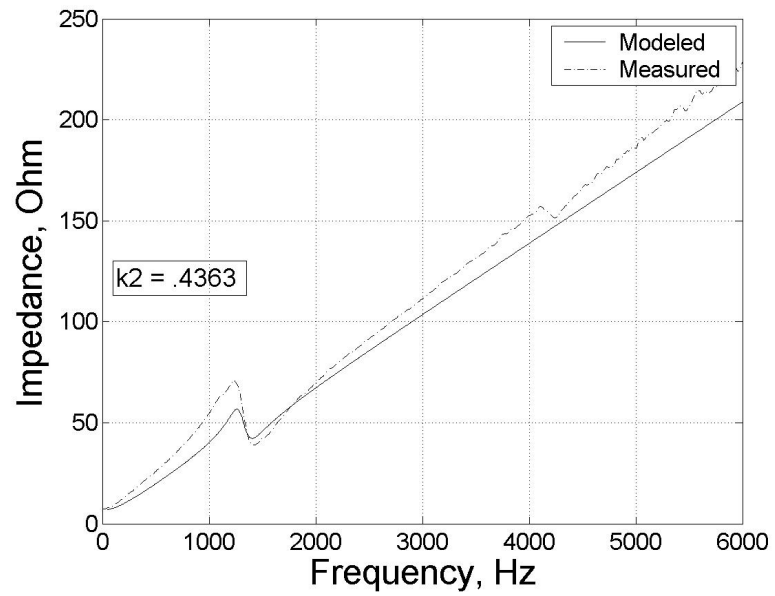


Figure 5.7: Electrical impedance magnitude with only Terfenol-D excitation.

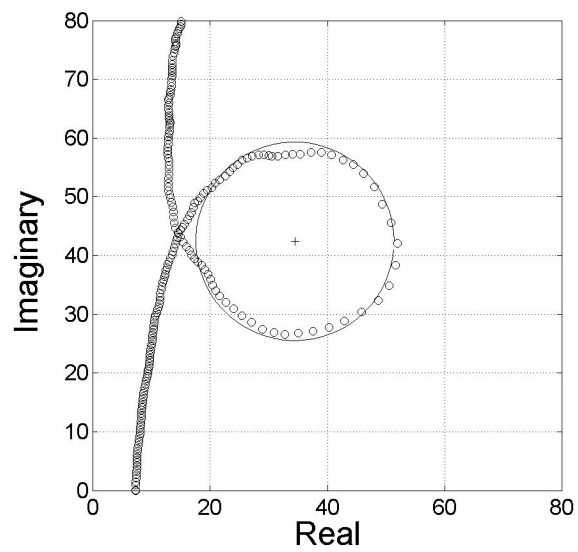


Figure 5.8: Impedance mobility loop with only Terfenol-D excitation.

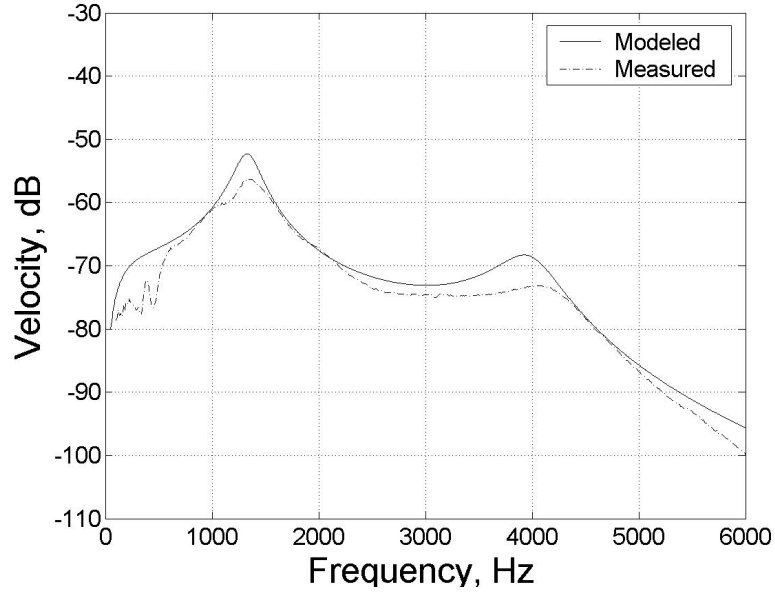


Figure 5.9: Head mass velocity response with only Terfenol-D excitation with external load Z_L .

is the presence of increased damping. This is apparent in the head mass velocity response shown in Figure 5.9, which has the same features as the unloaded result. It is noted that whereas the model accurately predicts the level of damping in the unloaded case, it underestimates the damping in this loaded situation. Figure 5.10 shows how the addition of damping in the amount of 600 Ns/m (about a 100% increase) to the modeled load impedance can compensate for this and bring the modeled Terfenol-D resonance right onto the measured data. The need for this excess damping may be explained by equation (1.30) being an approximation best suited for lightly damped systems [21]. For continuity, all further graphs with the external load include this extra term.

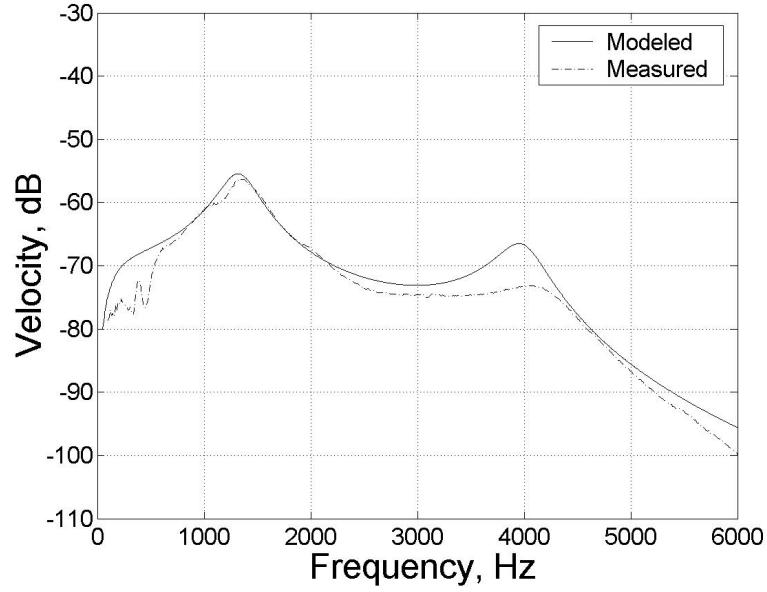


Figure 5.10: Head mass velocity response with only Terfenol-D excitation with external load and increased damping in the modeled load impedance.

The same loaded velocity response is plotted in Figure 5.11, but with the results from the nonlinear model and the simplified modal linear model as well. The linear model assuming ideal modes ignores all off-mode contributions as explained in Chapter 2. The nonlinear model is shown to agree with the data near the Terfenol-D resonance, but predicts more output from the PMN-PT section than what is actually seen, and shows a steeper roll off on the low frequency end. These disparities are best explained by the nonlinear model not being optimized for the transducer. The data analysis that yields the lumped system parameters for use in the linear model does not provide equal insight into the distributed properties of the smart materials, particularly the internal damping. As such the nonlinear model coefficients are simply estimates at this stage. The result of this is that the full linear model is found

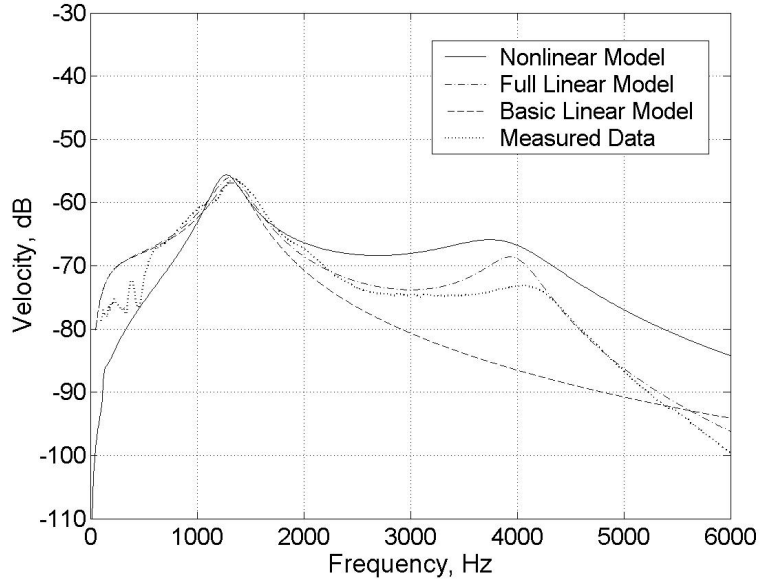


Figure 5.11: Head mass velocity response with only Terfenol-D excitation from all models.

to be sufficiently accurate at low drive levels, and thus will be exclusively used in most of the figures. The nonlinear model has been shown the potential to properly characterize the transducer motions, but will be necessary only at operating regimes beyond the linear model's capabilities.

Returning to the full linear model, the electrical impedance magnitude in Figure 5.12 shows that the coupled motional effects are somewhat diminished due to the damping, but the overall form is the same as before. The coupling value displayed is significantly less than in the unloaded case, but this may simply be a numerical issue since the coupling estimates (2.23)-(2.24) become poor approximations in heavily damped systems [12]. The mobility loop in Figure 5.13 is smaller and more teardrop shaped, a sign of increased losses [5, 15].

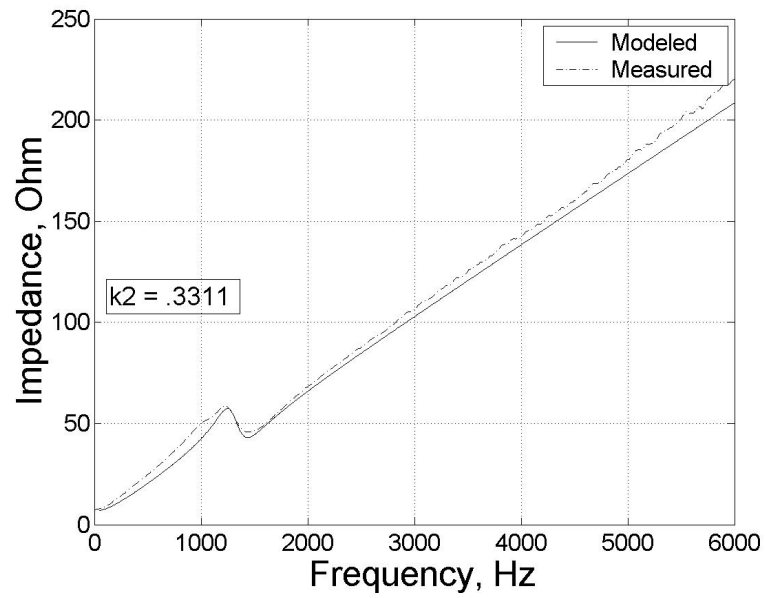


Figure 5.12: Electrical impedance magnitude with only Terfenol-D excitation with external load.

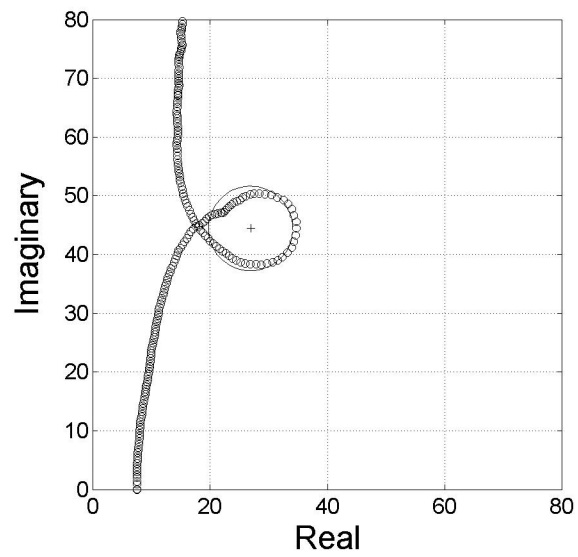


Figure 5.13: Impedance mobility loop with only Terfenol-D excitation with external load.

5.2.2 PMN-PT Section

Identical tests are run on just the PMN-PT section of the transducer, with the magnetic drive coil left as an open circuit. The unloaded velocity response in Figure 5.14 shows the high frequency resonance near 3900 Hz as expected. The off-mode effects of the Terfenol-D section are as before at a higher frequency than anticipated by the model due to the open circuit. Figure 5.15 displays the electrical impedance magnitude, where the inverse relationship to frequency depicts the stack's capacitive properties. The pronounced motional impedance effects are found in Figure 5.16 to result in a nearly perfectly shaped circular loop, which implies that in this particular transducer the piezoelectric transduction process is cleaner and more efficient than the magnetostrictive counterpart. The loop is in the fourth quadrant because the capacitive impedance can be written $1/j\omega C = -j/\omega C$, placing it along the negative imaginary axis.

When the external load impedance is added, the same trends as in the Terfenol-D section are observed. The dampened version of the head mass velocity response is plotted in Figure 5.17, which displays all of the model results. Here, the nonlinear model is practically identical to the full linear model, confirming the nonlinear formulation. Once again, however, the fact that the nonlinear model offers no advantages for this drive configuration implies that it will only be used when high drive levels require it. Figures 5.18 and 5.19 show how the added load causes a drastic reduction on the magnitude of the motional effects, and correspondingly on the size and circular quality of the impedance mobility loop.

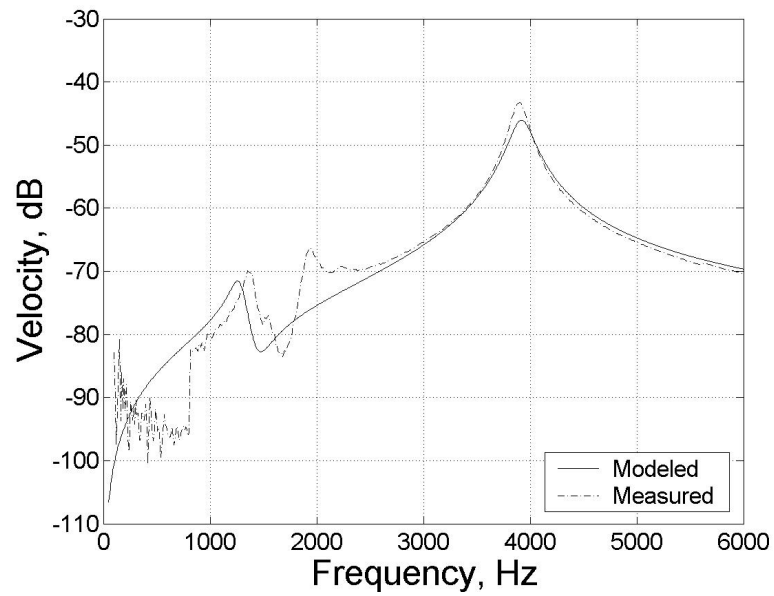


Figure 5.14: Head mass velocity response with only PMN-PT excitation.

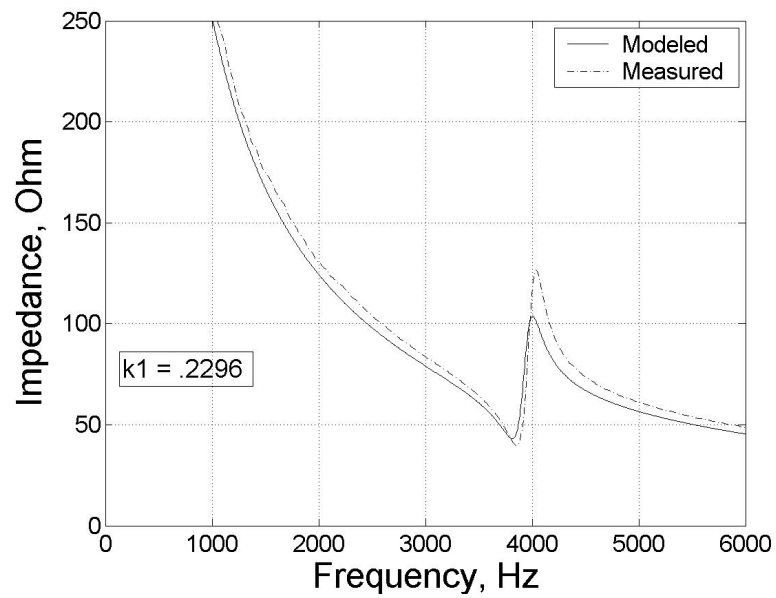


Figure 5.15: Electrical impedance magnitude with only PMN-PT excitation.

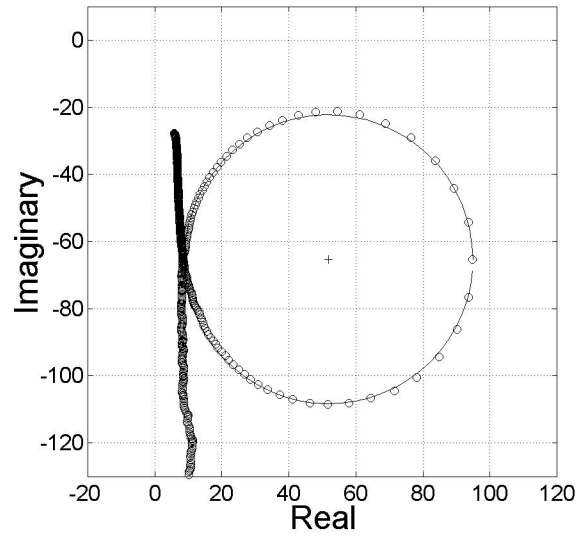


Figure 5.16: Impedance mobility loop with only PMN-PT excitation.

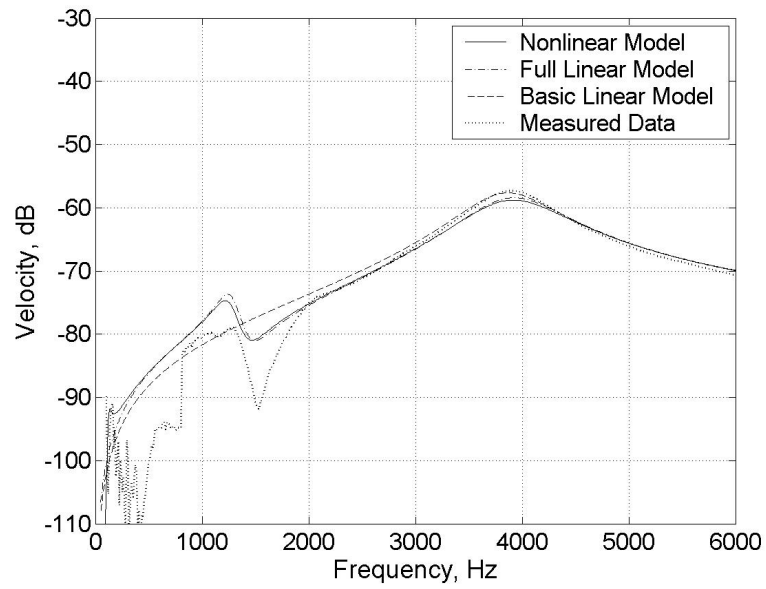


Figure 5.17: Head mass velocity response with only PMN-PT excitation from all models.

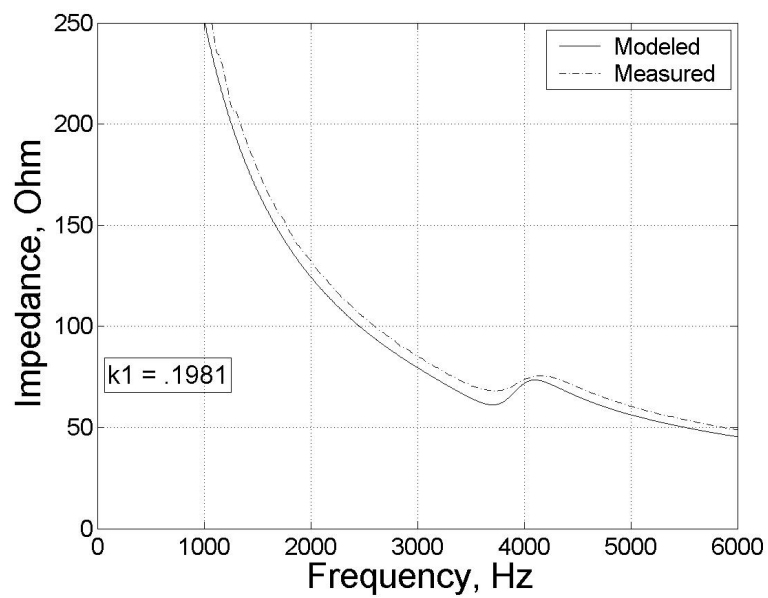


Figure 5.18: Electrical impedance magnitude with only PMN-PT excitation with external load.

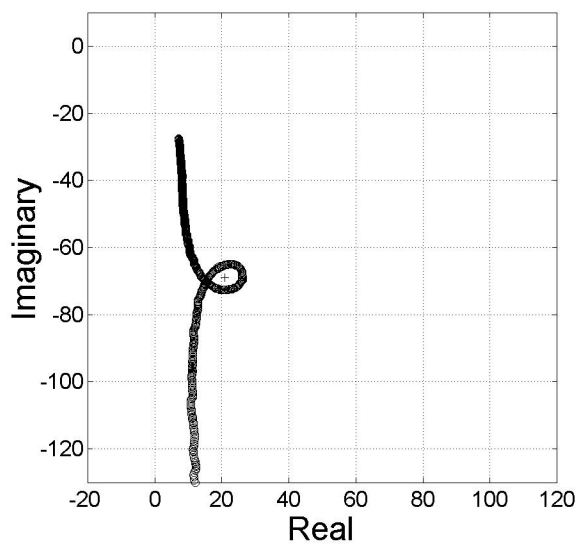


Figure 5.19: Impedance mobility loop with only PMN-PT excitation with external load.

5.2.3 Complete Transducer

When the two sections are wired in parallel and driven with the same 0 - 4.2 V random voltage excitation, the two modes' resonant peaks overlap to successfully extend the transducer bandwidth to below 1 kHz. The results in Figure 5.20 show that although the measured peaks overlap accurately with the modeled responses, the lack of significant damping creates a large magnitude variation over the frequency range of interest that actually constitutes a poor overall bandwidth. Driving the transducer against the duct seal loading adds the needed damping, and the resulting velocity response in Figure 5.21 shows a substantially flatter and more desirable bandwidth.

An important goal of this study is to characterize the effect of the electrical resonance on the transducer bandwidth. To this end, the impedance magnitude in Figure 5.22 shows the results for the case when the drive solenoid and piezoceramic stack are wired together in electrical parallel. The Terfenol-D section is shown to behave normally, that is the impedance increases with frequency, but the PMN-PT section's resonance is now just to the left of the electrical resonance frequency $\omega_{n,e} = 1/\sqrt{LC}$. As a result, the motional effects are quite large, and the coupling k_1 is improved from the PMN-PT only case. However, Figure 5.23 illustrates that the PMN-PT element's mobility loop is actually in the first quadrant, before the electrical resonance frequency at the real axis-intercept. This means that the capacitive stack is behaving inductively in this configuration. Wiring an external 378 nF capacitor in parallel with the circuit changes the effective capacitance and thus shifts the electrical resonant frequency to in between the two mechanical resonances. Figure 5.24 shows that the impedance magnitude is now indicative of the two individual modes,

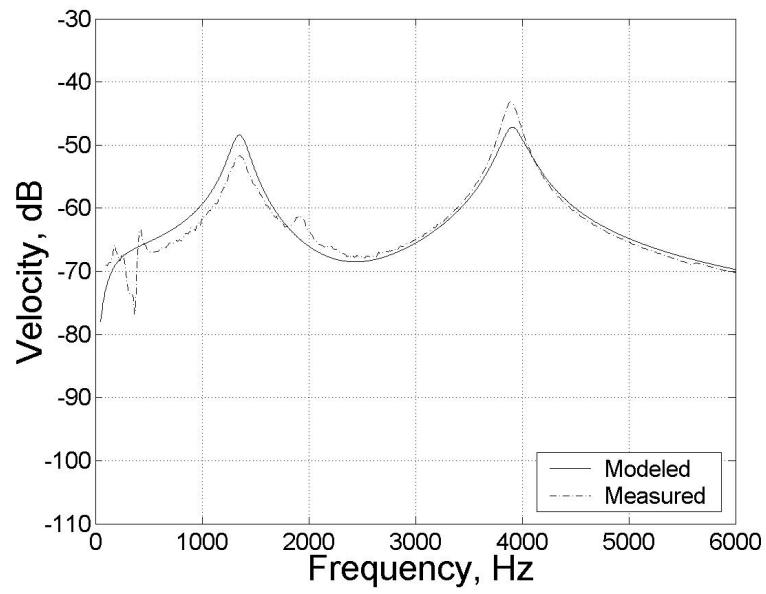


Figure 5.20: Head mass velocity response with both sections driven.

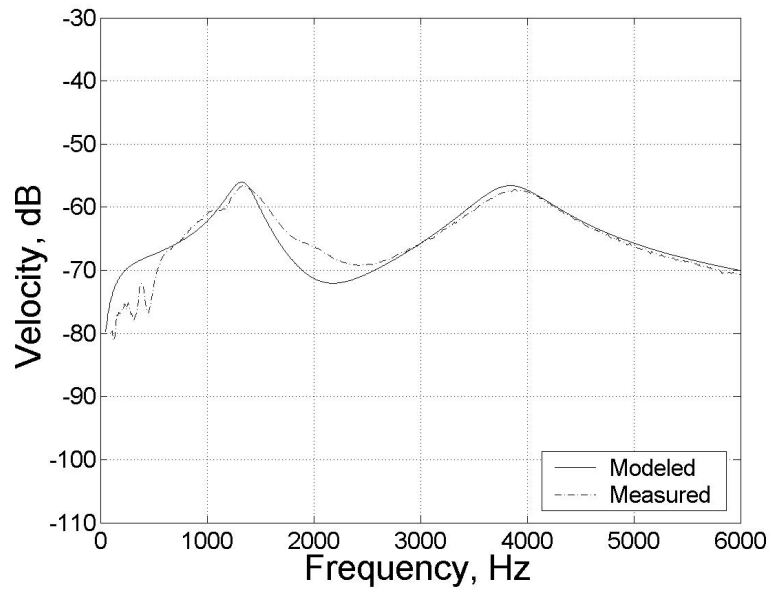


Figure 5.21: Head mass velocity response with both sections driven with external load.

as the Terfenol-D section is inductive and the PMN-PT section is once again capacitive. The Nyquist plot in Figure 5.25 illustrates that the two sections resonate in their original quadrants. The most important result lies in the head mass velocity response, where a comparison of Figures 5.26 and 5.27 reveals that altering the electrical resonance leaves the transducer bandwidth unaffected. This result carries a variety of implications, particularly the design consideration that replacing the piezoceramic or the magnetic solenoid with an alternate component of the same type will not fundamentally alter the transducer performance.

Finally, the resulting bandwidth of Figure 5.27 is found to have a magnitude deviation of about 12 dB over the frequency range of interest. Typically this would be considered too large of a variation for effective use, but it must be considered that these Tonpilz transducers are typically incorporated into an array structure. A U.S. Navy prototype of a similar hybrid architecture has been shown to exhibit a comparable decibel variation over the bandwidth of a single element, but only a 3 dB variation when configured in a 4×4 transducer array [3].

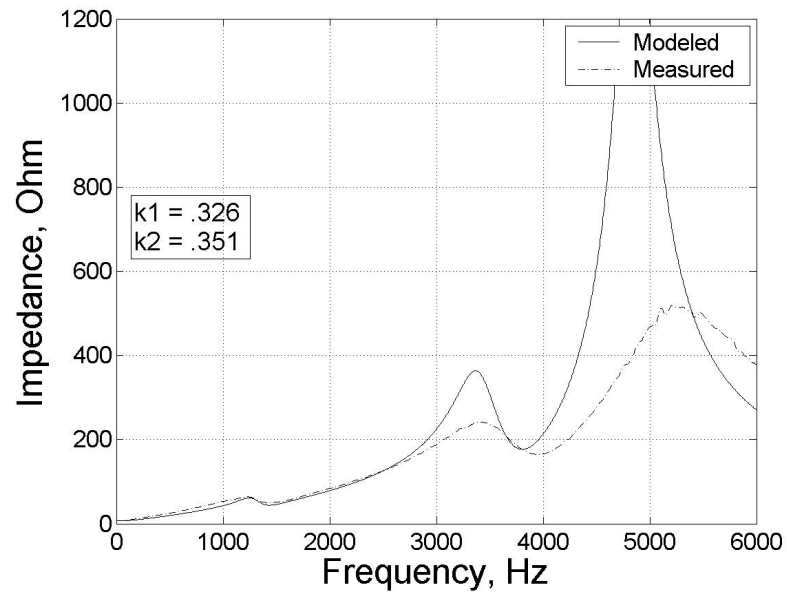


Figure 5.22: Electrical impedance magnitude with both sections driven in parallel with external load.

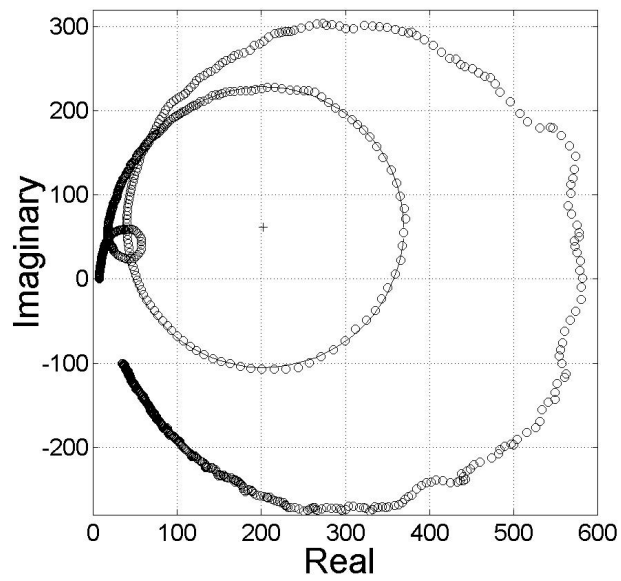


Figure 5.23: Impedance mobility loop with both sections driven in parallel.

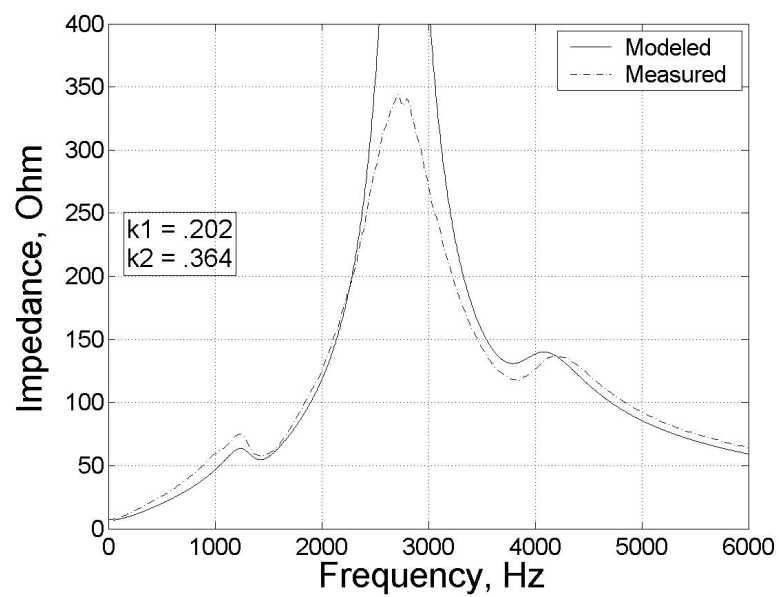


Figure 5.24: Electrical impedance magnitude with both sections driven with external load and added capacitor.

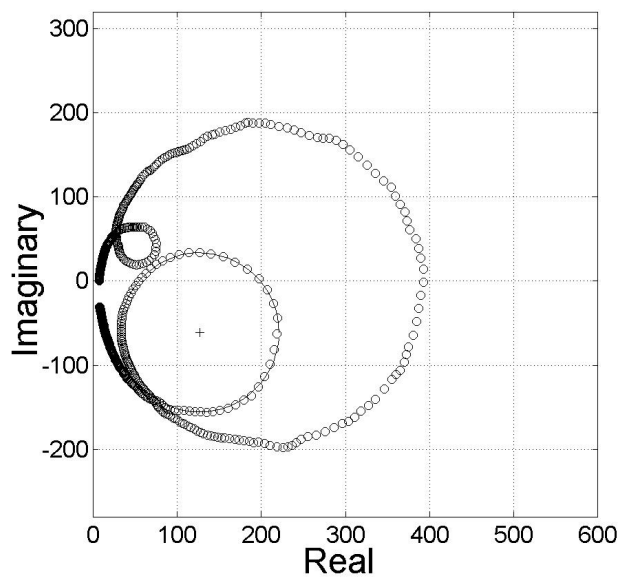


Figure 5.25: Impedance mobility loop with both sections driven and added capacitor.

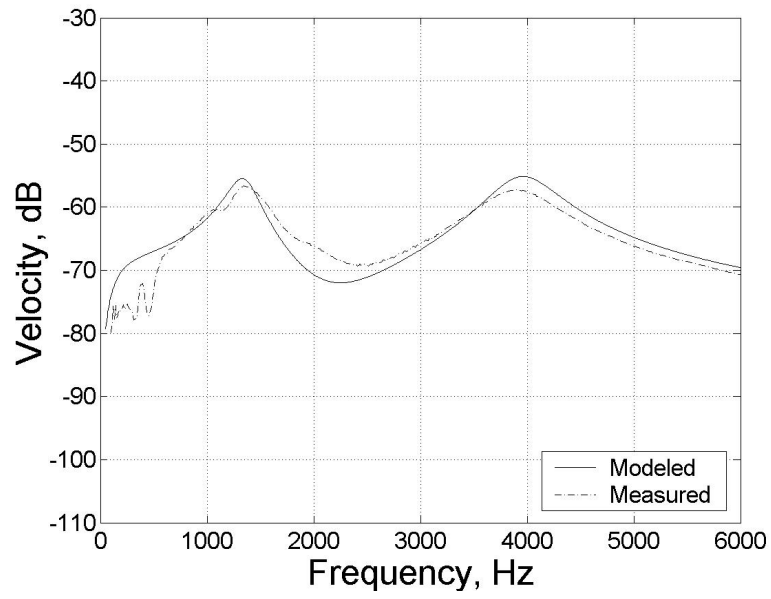


Figure 5.26: Head mass velocity response with both sections driven with external load and added capacitor.

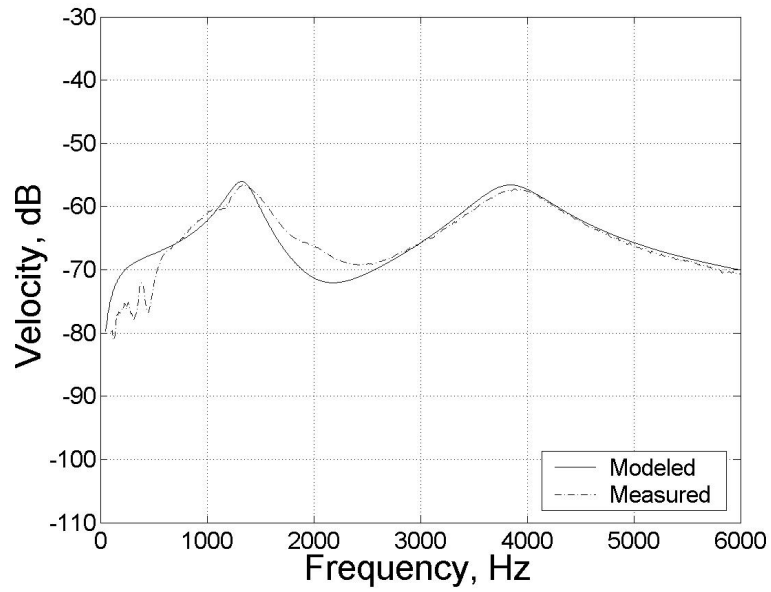


Figure 5.27: Head mass velocity response with both sections driven with external load.

CHAPTER 6

CONCLUDING REMARKS

The goal of this investigation was to develop an accurate modeling framework for application to hybrid smart material structures containing more than one active element. The specific focus involved extending the frequency bandwidth of a Tonpilz sonar transducer to 1-6 kHz, which has been shown to be successfully accomplished.

The overall approach of this investigation was as follows. The first chapter reviewed the fundamental concepts behind electromechanical systems, and how they relate to hybrid smart structures. Chapter 2 worked through the development of the total linear transducer model by combining concepts from mechanical vibrations, electroacoustics, and the constitutive material relations into a unified expression. While the results of this model compared favorably with experimental data, the use of the model is constrained to low input operation. Knowing that a more complete transducer description is needed for arbitrary operation, a detailed nonlinear model was developed in Chapter 3. The design and experimental setup of the physical test transducer were outlined in Chapter 4, with the results presented in Chapter 5.

6.1 Conclusions

The most important results from the model and data analysis are summarized below. In the formulation of the linear model it is learned that the modal analysis, while useful for estimating the resonance frequencies, fails to address all pertinent dynamics in the transducer. From the results in Chapter 5, it is apparent that for the low drive levels employed, the full linear model provides an excellent fit to the measured data. The linear frequency domain nature of the system equations also imply that they are useable in control applications. The linear model's main issue at the low regimes implemented is the need for extra damping, on the order of 600 Ns/m, to be added to the estimated load impedance Z_L to correct for inaccuracies in equation (1.30) for the damping coefficient.

The nonlinear model is based heavily on the prior works of Smith [33] and Dapino [10], but this investigation combines them in a novel manner. Expanding the published one-degree-of-freedom structural model to a two-degree case is straightforward, but a variety of issues arise when developing the three-degree-of-freedom situation. Trying a force balance between two different rods (one for each material) gives results that range from physically inaccurate to completely unstable. The approach of a single transducer with variable properties better incorporates the mechanical series coupling of the two sections and reduces to other simpler modes when certain limits are enforced.

From the measured data, a few important trends are observed. The most fundamental result is that the desired bandwidth has been achieved, and that the transducer bandwidth extends to even below 1 kHz. Although associated with undesirable losses, sufficient damping must be present in the system to flatten out the resonance peaks.

The figures in Chapter 5 show that the external load impedance accomplishes this goal at the cost of diminishing the transduction processes in the two smart materials.

Variation of the system capacitance, and thus electrical resonance, is shown to alter the impedance of each active section but cause a negligible change in the transducer bandwidth. This implies that the specific electrical properties of each smart material can be altered, supporting the idea of retrofitting older transducers (typically employing PZT) with modern materials such as PMN-PT. The case where the electrical resonance frequency overlaps with the PMN-PT section's mechanical peak showed the maximum coupling for that element, meaning potential gains might be achievable. Further investigation into this effect may shed light on the high energy efficiencies thought to be attainable in hybrid structures.

6.2 Future Work

While this research has accomplished several key goals, there is still potential for further study. An original focus of hybrid systems research was the implementation of high energy efficiencies by driving the structure near its electrical resonance. As mentioned, this investigation showed that maximum coupling is attained for an individual section when the electrical and mechanical resonances overlap. Continued research could be done on methods to shift the electrical resonance onto each section's mode for improved transduction. Additionally, experimental energy measurements can be made to determine the driving efficiency of the transducer over the entire bandwidth. This information would prove useful in optimizing the overall transducer performance.

Of primary interest for further development is a more complete implementation of the nonlinear model. The model is composed of several parts, each requiring that

a number of numerical constants be optimized from measured data. This procedure requires a combination of least-square regressions that has not been used to this point. As a result, the nonlinear model is not easily compared with either the linear model or the physical data, particularly in the hysteretic P and M relations. The optimization of the fit between these curves and actual data is imperative to fully reduce the discrepancies that will propagate through the rest of the nonlinear model. Proper correlation of the nonlinear model will be necessary to simulate the potential effects of high drive regimes, as the inherent hysteresis and saturation effects could offer unique enhancements of the transducer bandwidth.

In combination with this, a variety of alternate drive configurations may provide a more optimal transducer response. Specifically, constant current and swept sine inputs would generate slightly different transducer outputs that could lead to new ideas. The inherent delta- E effect in Terfenol-D could be creatively used to shift the lower resonance peak over a range that further extends the system bandwidth.

Another consideration for future research is in expanding the experimental setup to more accurately measure the quantities of interest. The bandwidth in this thesis is considered to be represented by the head mass velocity response, which is only an approximation. A more accurate sonar response can be found by driving the transducer underwater and using microphone pickups, which would present additional implementation difficulties. Tonpilz transducers are typically employed in an array structure to improve the overall performance, and although constructing additional devices may be impractical, analytical techniques exist that could be used to simulate the differences in the array loading.

APPENDIX A

UNITS IN ELECTROMAGNETISM

The following table summarizes the most common electromagnetic quantities in both the CGS or Gaussian system and the SI system with Sommerfeld convention.

Quantity	Symbol	CGS	SI	Conversion/Value
Electric charge	q	-	coulomb (C)	$C = A \cdot s$
Current	I	-	ampere (A)	-
Electric potential	V	-	volt (V)	-
Electric field	\vec{E}	-	V/m	-
Electric induction	\vec{D}	-	C/m ²	-
Electric flux	Φ	-	N·m ² /C	-
Permittivity	ϵ_0	-	C ² /N·m ²	8.85×10^{-12}
Electric moment	\vec{p}	-	C·m	-
Polarization	\vec{P}	-	V/m	-
Magnetic field	\vec{H}	oersted (Oe)	A/m	$Oe = 79.58 \text{ A/m}$
Magnetic induction	\vec{B}	gauss	tesla (T)	$gauss = 10^{-4} \text{ T}$
Magnetic flux	ϕ	maxwell	weber (Wb)	$maxwell = 10^{-8} \text{ Wb}$
Permeability	μ_0	-	H/m	$4 \pi \times 10^{-7}$
Magnetic moment	\vec{m}	emu	A·m ²	-
Magnetization	\vec{M}	emu/cc	A/m	$emu/cc = 1000 \text{ A/m}$
Resistance	R	-	ohm (Ω)	$\Omega = V/A$
Capacitance	C	-	farad (F)	$F = A \cdot s/V$
Inductance	L	-	henry (H)	$H = V \cdot s/A$

Table A.1: Principal variables and units in electricity and magnetism.

APPENDIX B

MECHANICAL PART DRAWINGS

This appendix contains the individual mass and magnetic circuit drawings of the key components in Figure 4.1. The head, center, and tail masses are represented in Figures B.1, B.2, and B.3, respectively. The steel pieces required to complete the magnetic circuit path are depicted in Figures B.4, B.5, and B.6.

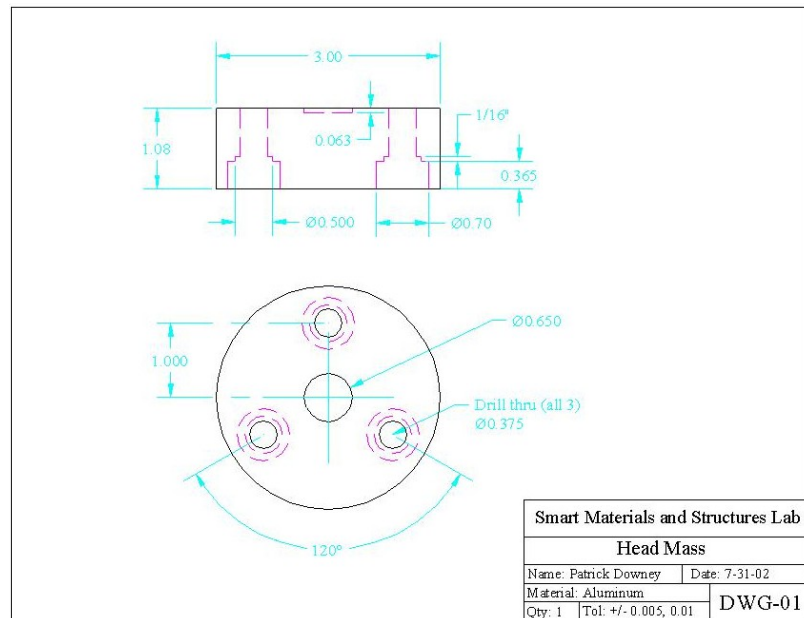


Figure B.1: Mechanical drawing of head mass.

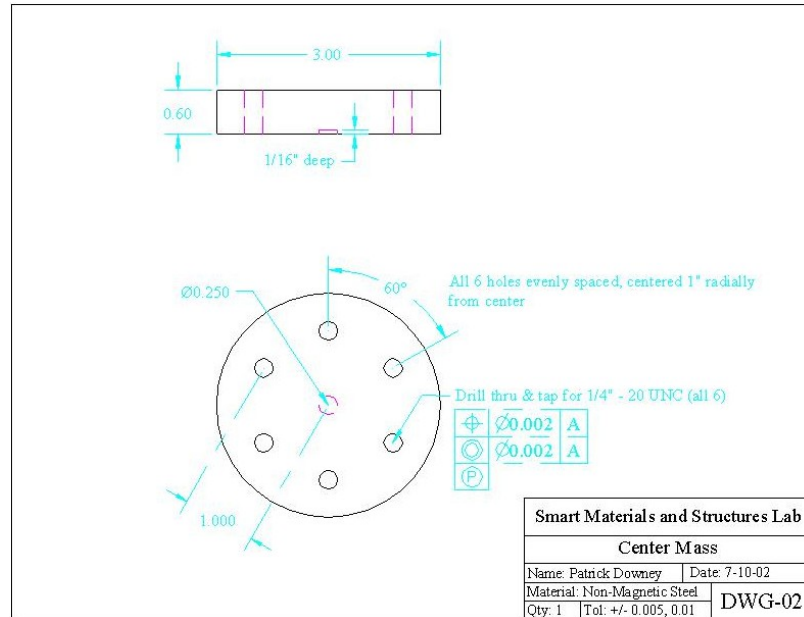


Figure B.2: Mechanical drawing of center mass.

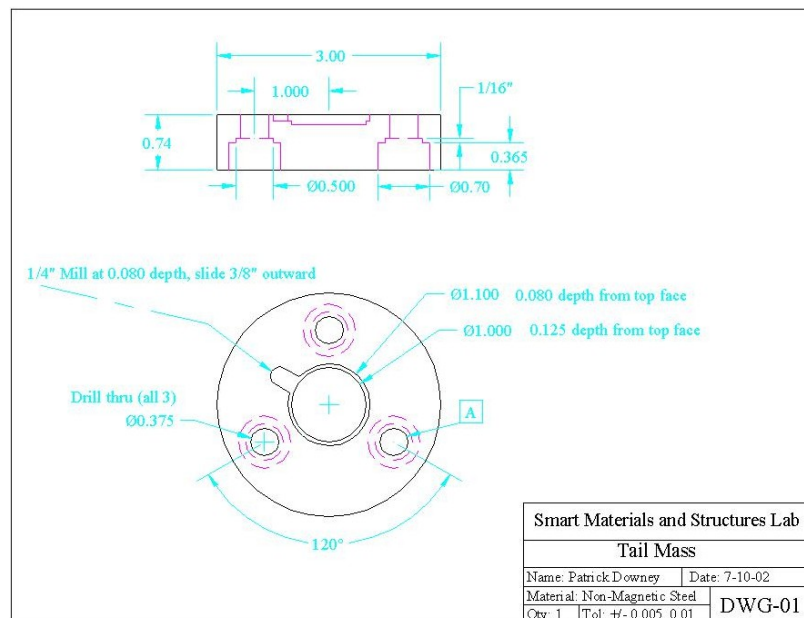


Figure B.3: Mechanical drawing of tail mass.

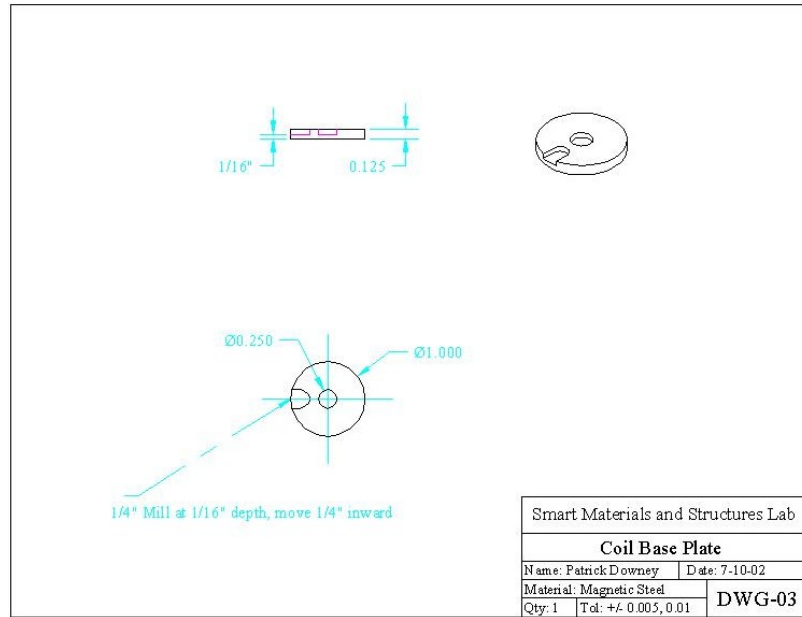


Figure B.4: Mechanical drawing of a magnetic circuit steel piece.

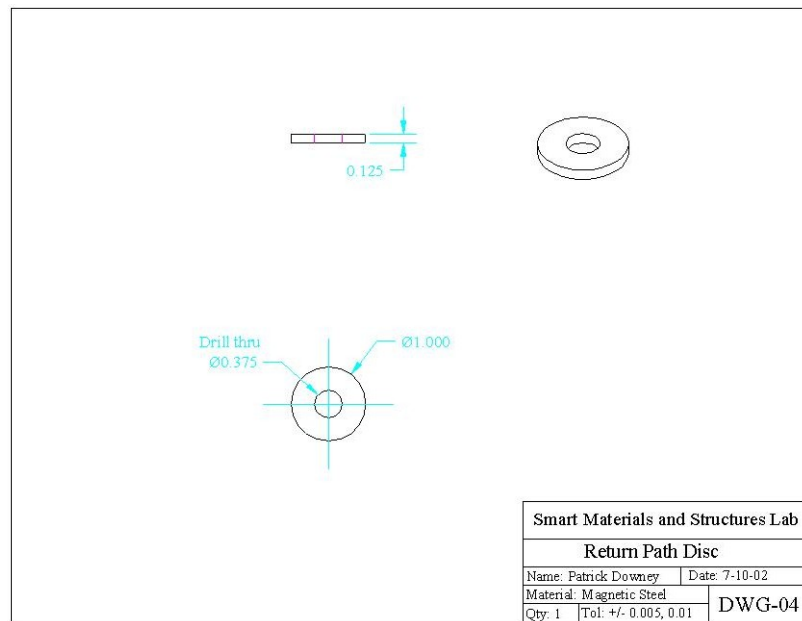


Figure B.5: Mechanical drawing of a magnetic circuit steel piece.

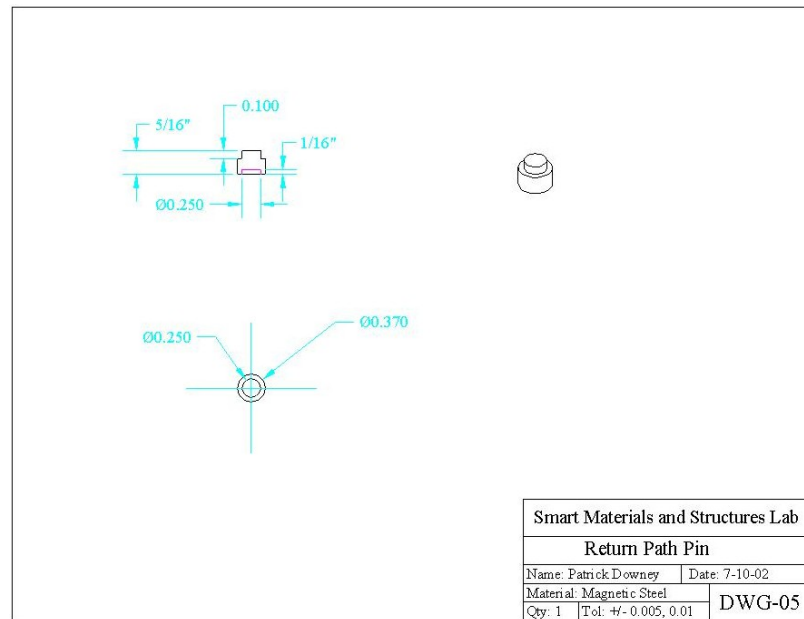


Figure B.6: Mechanical drawing of a magnetic circuit steel piece.

APPENDIX C

AMPLIFIER CHARACTERIZATION

The high frequency response of the two Techron 7780 amplifiers is measured for resistive, inductive, and capacitive loading. The amplifiers are tested in series with 100 mV random noise input and a DAQ frequency span from DC to 20 kHz. The measured quantities are the magnitude and phase of the output voltage to input voltage transfer function.

Figures C.1 and C.2 show the full frequency response of the amplifiers when driving a purely resistive load. Both graphs show only minor deviations over the range of interest. The results for the inductor and capacitor are plotted in Figures C.3-C.4 and C.5-C.6, respectively, with each showing nice behavior as well. Overall the expected roll off is not found and the amplifiers behave better than anticipated.

To confirm the broadband tests, individual frequencies are tested as well via a 100 mV sine wave, the results of which are in Table C.1. An example of the 5 kHz test is shown in Figure C.7, where the gain value is read from the flat region at that specific frequency. Finally, these value were compared with the original tests in Figures C.8 and C.9. The conclusion is that the amplifiers are extremely reliable up to at least 20 kHz, with a constant gain of 60 V/V and a phase shift of only $-1^\circ/\text{kHz}$.

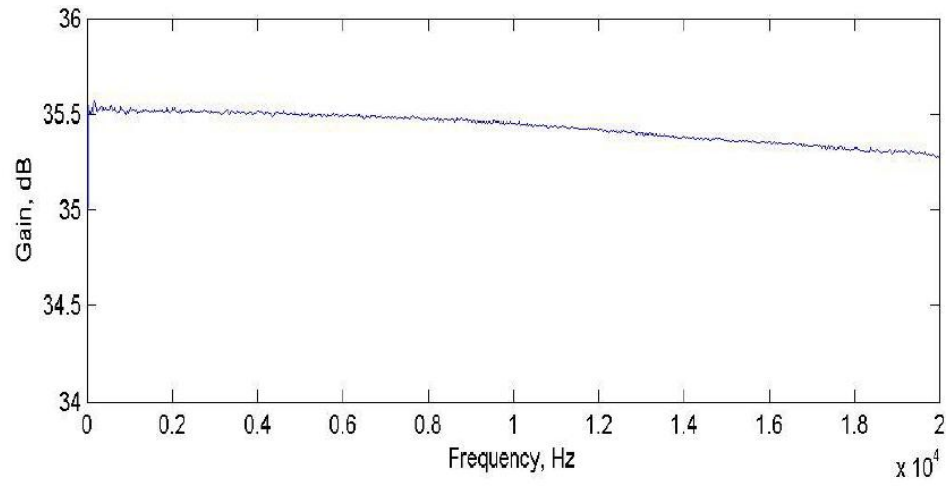


Figure C.1: Magnitude of amplifier frequency response with $R=10\Omega$ load.

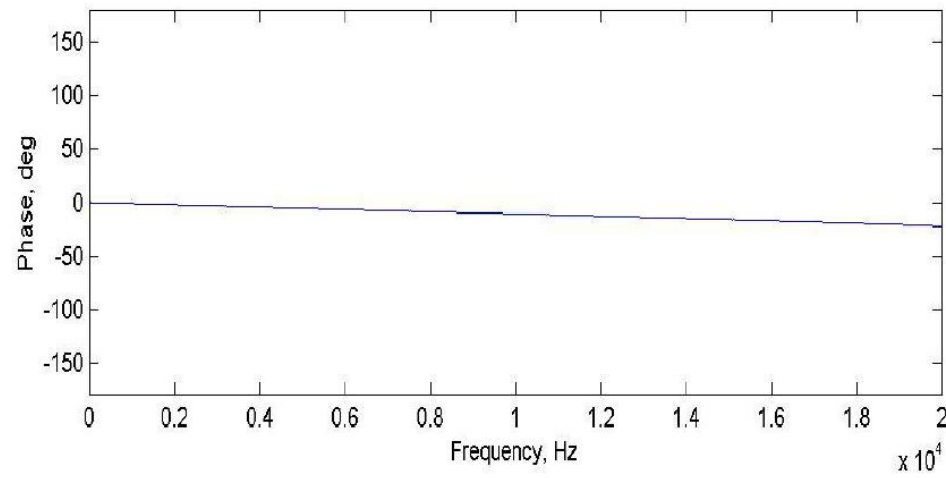


Figure C.2: Phase of amplifier frequency response with $R=10\Omega$ load.

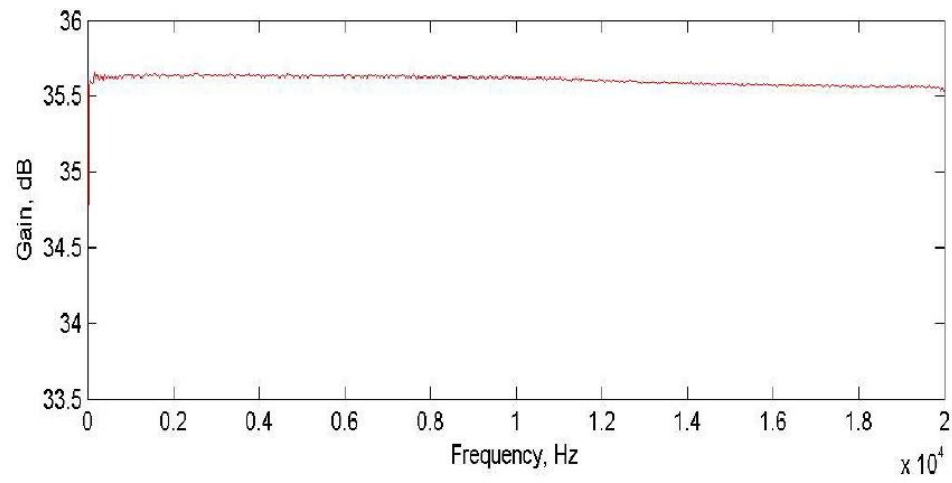


Figure C.3: Magnitude of amplifier frequency response with L=225 mH load.

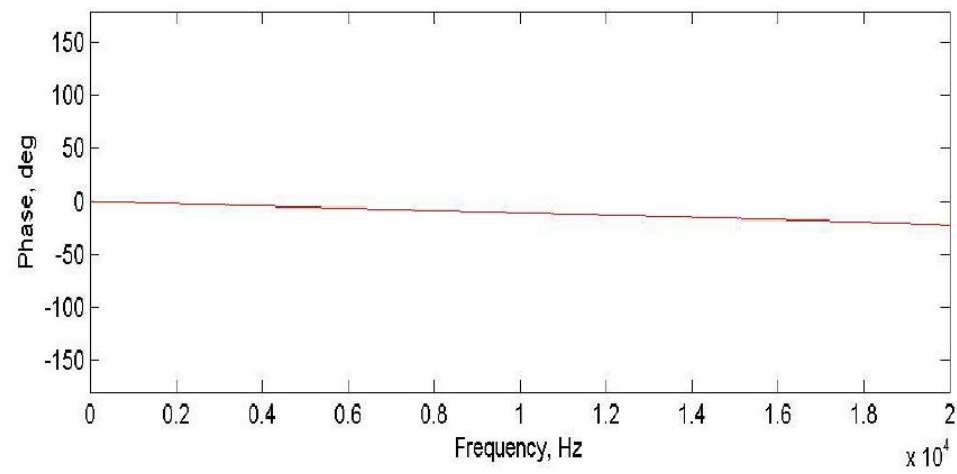


Figure C.4: Phase of amplifier frequency response with L=225 mH load.

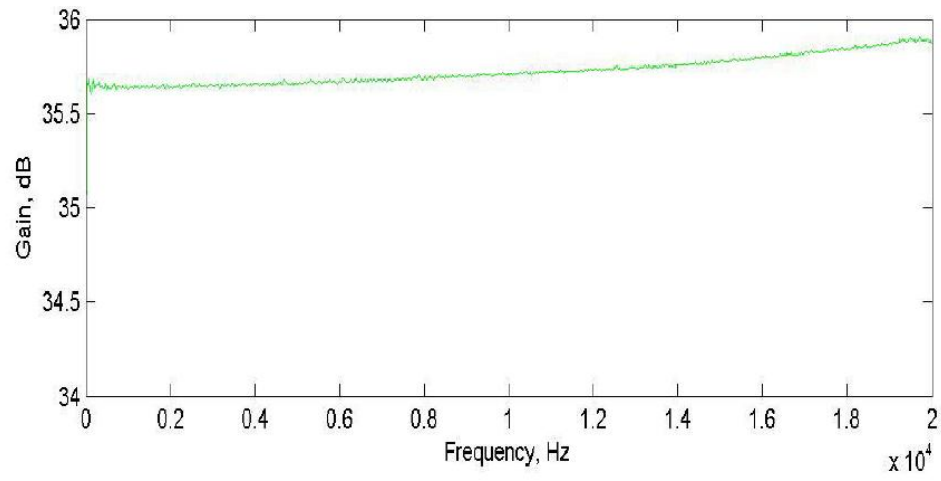


Figure C.5: Magnitude of amplifier frequency response with $C=390$ nF load.

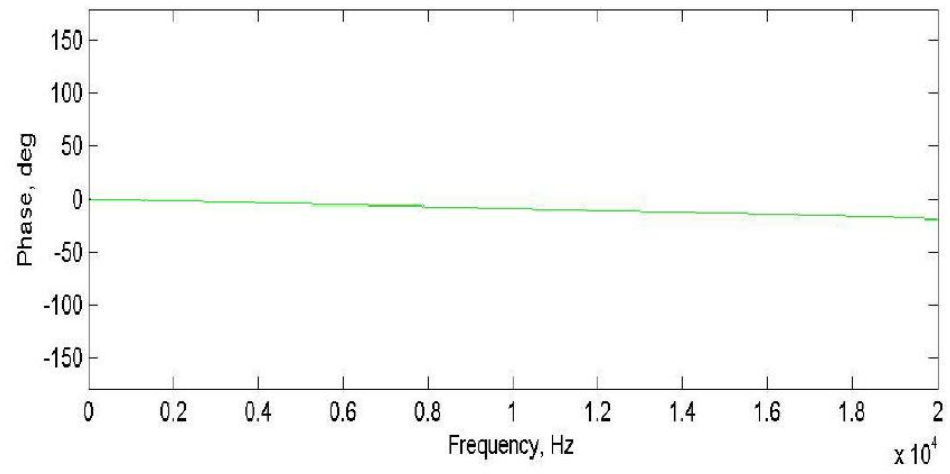


Figure C.6: Phase of amplifier frequency response with $C=390$ nF load.

Frequency (Hz)	Gain (V/V)		
	R	L	C
100	59.74	60.30	60.54
500	59.74	60.45	60.55
1000	59.73	60.48	60.55
2000	59.70	60.49	60.56
5000	59.55	60.46	60.65
10000	59.18	60.36	60.98
15000	58.68	60.22	61.55
19000	58.10	59.97	62.09

Table C.1: Amplifier voltage gains at discrete frequencies for each electrical load.

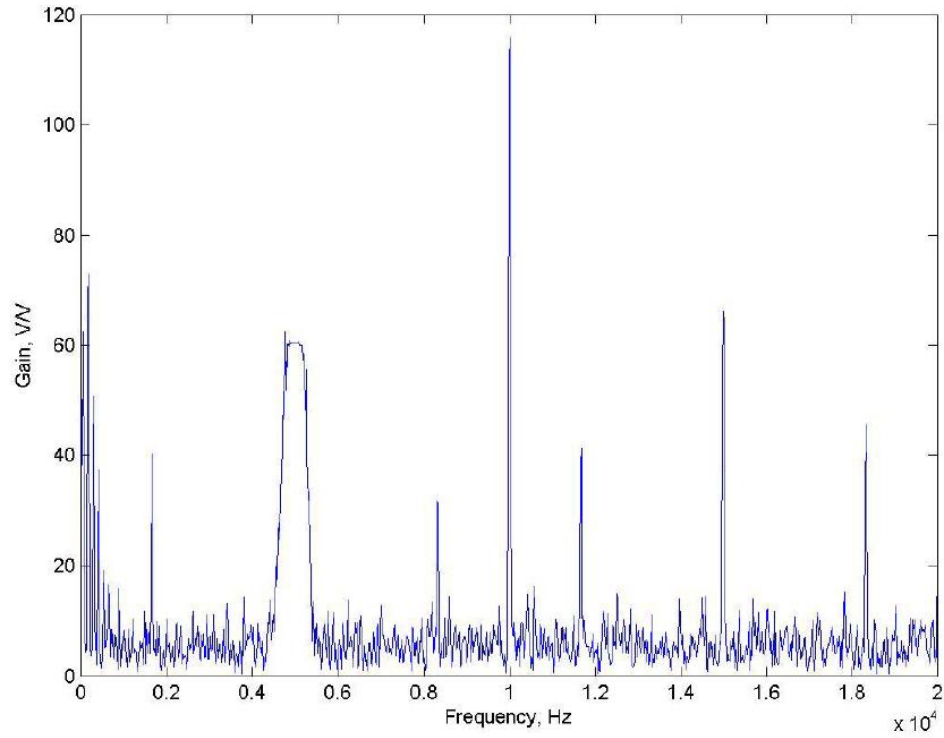


Figure C.7: Magnitude of amplifier frequency response to 5 kHz sine wave.

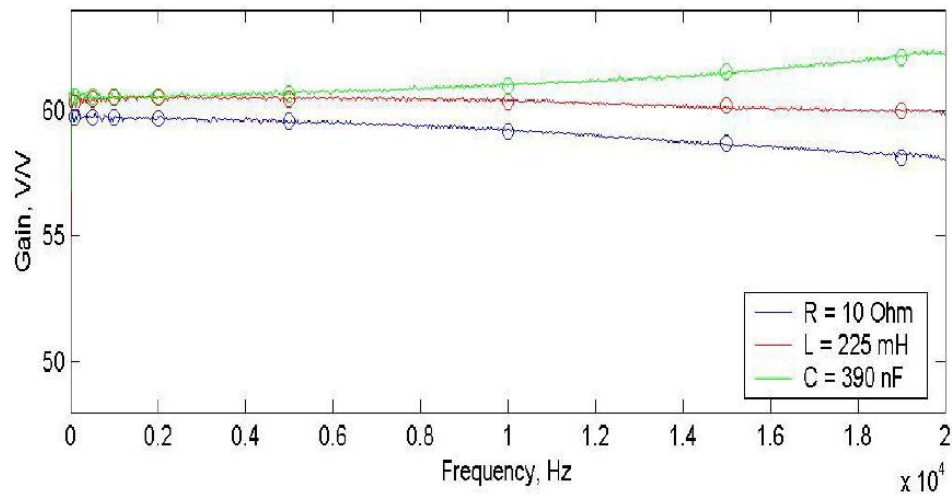


Figure C.8: Magnitude of amplifier frequency response to all loads, showing agreement between random and sinusoidal inputs.

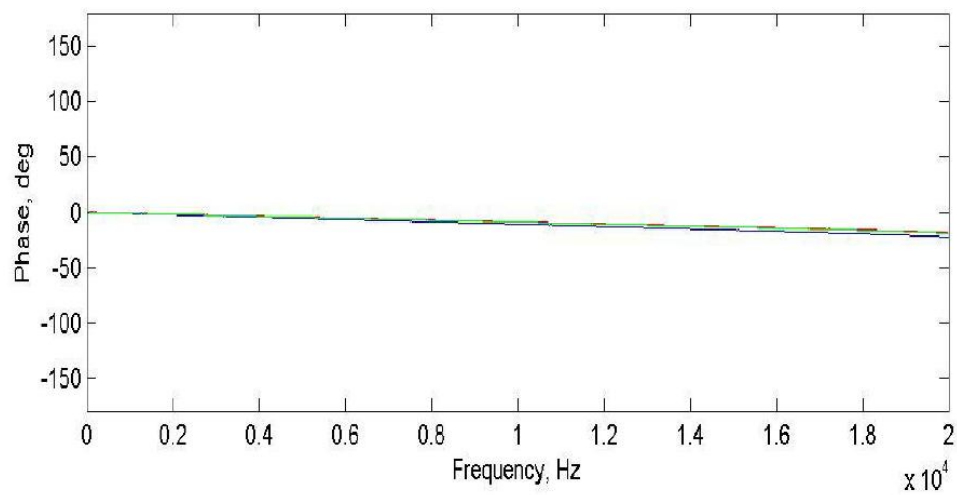


Figure C.9: Phase of amplifier frequency response to all loads.

BIBLIOGRAPHY

- [1] John L. Butler, Alexander L. Butler, and Stephen C. Butler. “Hybrid magnetostrictive / piezoelectric Tonpilz transducer”. *Journal of the Acoustical Society of America*, 94(2):636–641, August 1993.
- [2] John L. Butler, Stephen C. Butler, and Arthur E. Clark. “Unidirectional magnetostrictive / piezoelectric hybrid transducer”. *Journal of the Acoustical Society of America*, 88(1):7–11, July 1990.
- [3] Stephen C. Butler and Frank A. Tito. “A Broadband Hybrid Magnetostrictive / Piezoelectric Transducer Array”. *OCEANS 2000 MTS/IEEE*, 3:1469–1475, 2000.
- [4] Walter G. Cady. *Piezoelectricity*. McGraw-Hill, 1946.
- [5] Frederick T. Calkins and Alison B. Flatau. “Transducer based measurements of Terfenol-D material properties”. In *Proceedings SPIE*, number 2717-67, 1996.
- [6] Frederick T. Calkins, Ralph C. Smith, and Alison B. Flatau. “An Energy-based Hysteresis Model for Magnetostrictive Transducers”. *IEEE Transactions on Magnetics*, 36(2):429–439, 2000.
- [7] B.D. Cullity. *Introduction to Magnetic Materials*. Addison-Wesley, 1972.
- [8] Marcelo J. Dapino. “*Nonlinear and hysteretic magnetomechanical model for magnetostrictive transducers*”. PhD thesis, Iowa State University, 1999.
- [9] Marcelo J. Dapino, Frederick T. Calkins, and Alison B. Flatau. “On identification and analysis of fundamental issues in Terfenol-D transducer modeling”. In *Proceedings SPIE*, volume 3329, 1998.
- [10] Marcelo J. Dapino, Ralph C. Smith, and Alison B. Flatau. “Structural Magnetic Strain Model for Magnetostrictive Transducers”. *IEEE Transactions on Magnetics*, 36(3):545–556, May 2000.

- [11] Alison B. Flatau, Marcelo J. Dapino, and Frederick T. Calkins. “High Bandwidth Tunability in a Smart Vibration Absorber”. *Journal of Intelligent Material Systems and Structures*, 11(12):923–929, December 2000.
- [12] David Hall. “*Dynamics and vibrations of magnetostrictive transducers*”. PhD thesis, Iowa State University, 1994.
- [13] David Halliday, Robert Resnick, and Jearl Walker. *Fundamentals of Physics Extended*. John Wiley & Sons, Fifth edition, 1997.
- [14] Craig L. Hom and Natarajan Shankar. “A Fully Coupled Constitutive Model for Electrostrictive Ceramic Materials”. *Journal of Intelligent Material Systems and Structures*, 5:795–801, November 1994.
- [15] Frederick V. Hunt. *Electroacoustics: The Analysis of Transduction, and Its Historical Background*. American Institute of Physics for the Acoustical Society of America, 1982.
- [16] B. Jaffe, W.R. Cook, and H. Jaffe. *Piezoelectric Ceramics*. Academic Press, 1971.
- [17] H. Janocha and B. Clephas. “Hybrid Actuator With Piezoelectric and Magnetostrictive Material”. *ACTUATOR 96, Proc. 5th International Conference on New Actuators*, pages 304–307, 1996.
- [18] David Jiles. *Introduction to Magnetism and Magnetic Materials*. Chapman & Hall, 1991.
- [19] Rick A. Kellogg. “The Delta-E effect in Terfenol-D and its application in a tunable mechanical resonator”. Master’s thesis, Iowa State University, 2000.
- [20] Warren P. Mason. *Piezoelectric Crystals and Their Application to Ultrasonics*. D. Van Nostrand, 1950.
- [21] Leonard Meirovitch. *Fundamentals of Vibrations*. McGraw-Hill, 2001.
- [22] M.B. Moffett, A.E. Clark, M. Wun-Fogle, J. Lindberg, J.P. Teter, and E.A. McLaughlin. “Characterization of Terfenol-D for magnetostrictive transducers”. *Journal of the Acoustical Society of America*, 89(3), March 1991.
- [23] Francis C. Moon. *Magneto-Solid Mechanics*. John Wiley & Sons, 1984.
- [24] Robert L. Norton. *Machine Design: An Integrated Approach*. Prentice Hall, 1998.
- [25] Katsuhiko Ogata. *System Dynamics*. Prentice Hall, Second edition, 1992.

- [26] Seung-Eek Park and Thomas R. Shrout. “Characteristics of Relaxor-Based Piezoelectric Single Crystals for Ultrasonic Transducers”. *IEEE Ultrasonics Symposium*, 2:935–942, November 1996.
- [27] J.C. Piquette and S.E. Forsythe. “Generalized material model for lead magnesium niobate (PMN) and an associated electromechanical equivalent circuit”. *Journal of the Acoustical Society of America*, 104:2763–2772, 1998.
- [28] Dhilsha Rajapan. “Performance of a low-frequency, multi-resonant broadband Tonpilz transducer”. *Journal of the Acoustical Society of America*, 111(4):1692–1694, April 2002.
- [29] Giorgio Rizzoni. *Principles and Applications of Electrical Engineering*. McGraw-Hill, Third edition, 2000.
- [30] Thomas R. Shrout and Joseph Fielding. “Relaxor Ferroelectric Materials”. *IEEE Ultrasonics Symposium*, 2:711–720, 1990.
- [31] Ralph C. Smith, Marcelo J. Dapino, and Stefan Seelecke. “A Free Energy Model for Hysteresis in Magnetostrictive Materials”. Technical report, North Carolina State University, 2002.
- [32] Ralph C. Smith, Stefan Seelecke, Marcelo J. Dapino, and Zoubeida Ounaies. “A Unified Model for Hysteresis in Ferroic Materials”. Technical report, North Carolina State University, 2003.
- [33] Ralph C. Smith, Stefan Seelecke, Zoubeida Ounaies, and Joshua Smith. “A Free Energy Model for Hysteresis in Ferroelectric Materials”. Technical report, North Carolina State University, 2003.
- [34] Qingshan Yao and Leif Bjorno. “Broadband Tonpilz Underwater Acoustic Transducers Based on Multimode Optimization”. *IEEE Transactions on Ultrasonics, Ferroelectrics, and Frequency Control*, 44(5):1060–1066, 1997.